Stony Brook University

Probing DNA Dynamics with Fluorescence Cross-Correlation Spectroscopy

A Dissertation Presented

by

Tomasz Bakowski

to

The Graduate School

in Partial Fulfillment of the

Requirements

for the Degree of

Doctor of Philosophy

in

Biomedical Engineering

Stony Brook University

August 2015

Stony Brook University

The Graduate School

Tomasz Bakowski

We, the dissertation committee for the above candidate for the

Doctor of Philosophy degree, hereby recommend

acceptance of this dissertation.

Helmut Strey – Dissertation Advisor
Associate Professor of Biomedical Engineering

Emilia Entcheva - Chairperson of Defense
Professor of Biomedical Engineering

Jonathan Liu – Committee Member
Assistant Professor, Mechanical Engineering, University of Washington
Former Assistant Professor, Biomedical Engineering, Stony Brook University

Mircea Cotlet – Committee Member, External
Materials Scientist, Soft Biological Nanomaterials Team
Center for Functional Nanomaterials, Brookhaven National Labs

This dissertation is accepted by the Graduate School

Charles Taber
Dean of the Graduate School

ii

Abstract of the Dissertation

Probing DNA Dynamics with Fluorescence Cross-Correlation Spectroscopy

by

Tomasz Bakowski

Doctor of Philosophy

in

Biomedical Engineering

Stony Brook University

2015

DNA Polymer dynamics are fundamental to the function of biological systems. Examples include gene regulation, cell division, threading and transport through pores. We address the limitations of previous experimental studies of polymer dynamics by designing, building, and characterizing a novel, custom Fluorescence Cross-Correlation Spectroscopy (FCCS) system. We detail the optical considerations for quantitatively describing and shaping the confocal volume. The hardware is supplemented by a robust theoretical foundation of correlation analysis and how it applies to polymer dynamics. We carry this theory through in the design of novel fitting methods and software. We utilize our FCCS setup to quantitatively measure important polymer dynamics of DNA in solution, such as diffusion coefficients and relaxation time, both more carefully and at lower molecular weights than typically accessible by single color FCS or standard fluorescence microscopy. By establishing a well-characterized FCCS measurement platform and detailing its functionality and applicability to polymer dynamics, we lay the foundation to applying our system to further measurements within nano-confinement. A detailed nanofabrication approach is provided. Better understanding internal polymer dynamics under nano-confinement has significant potential applications in designing more robust molecular separations technologies as well as the ability to address fundamental research questions in biophysics and molecular biology.

Dedication Page

My sincerest thanks go to the following people:

For my adviser, for never losing faith in me and displaying the utmost levels of patience, understanding, and intellect while guiding me through the process.

For my family, for showing me what unconditional love is and doing so even at the most difficult moments.

For all of my friends, who, despite my decidedly curmudgeonly attitude, remain steadfastly loyal while providing warmth, understanding, and humoring my endless philosophical debates.

Table of Contents

List of Figures

normalized curves are graphed as a function of mean squared displacement in the right column

List of Tables

List of Abbreviations

CEF – Collection Efficiency Function

EBL / E-beam – Electron Beam Lithography

FCS – Fluorescence Correlation Spectroscopy

FCCS – Fluorescence Cross-Correlation Spectroscopy

FJC – Freely Jointed Chain

FRET – Fluorescence Resonance Energy Transfer

MSD – Mean Squared Displacement

NA – Numerical Aperture

MDF – Molecule Detection Function

PSQ – Polysilsesquioxane

I.   Introduction

DNA is a natural choice for studying polymer dynamics. It is a model polymer. DNA is easy to modify, capable of assuming different topologies (e.g. linear, circular), and well characterized, allowing for studies that would otherwise be limited with synthetic polymers. DNA also is at the heart of many biological questions and, therefore, technologically important for a wide-range of medical applications.

Previous research studying DNA dynamics has been extensive, however, far from complete. Most studies of DNA under nano-confinement focused on fluorescence microscopy coupled with intercalating dye labeled DNA. The choice of microscopy limited study to DNA larger than lambda-DNA (48kbp with slowest internal relaxation time of approximately 0.2 sec) and basic nano-channel geometries.

Other research has focused on anchoring and stretching DNA molecules out linearly to study protein search. This limits the ability to replicate biological conditions where DNA oftentimes is not linearized but confined in someway. Further still, FRET techniques for studying DNA dynamics are limited in the information they are capable of revealing due to the limited interaction distance on the order of angstroms.

Fluorescence Correlation Spectroscopy (FCS) presents itself as an experimental alternative addressing the limitations of the above-mentioned techniques due to the ability to focus on: 1) a wide-range of timescales (nanoseconds to seconds) 2) distances on the order of microns 3) single molecules in solution. Despite these advantages, previous incarnations of FCS were limited in their application to studying DNA dynamics because of the use of only one color, poor characterization of the optics, and oversimplification of the nature of the confocal volume and resultant fitting procedure. All of these factors limit one's ability to discern subtle yet important features of DNA dynamics and effectively identify and quantify fit parameters.

Our goal has been to address all of the above-mentioned limitations of previous work by establishing the building blocks of a homebuilt two-color Fluorescence Correlation Spectroscopy device for expanding upon the understanding of DNA dynamics both in solution and under nano-confinement. Such a platform would have applications towards the design of better separations technologies for DNA and polymers with different molecular weights, among others.

In order to achieve our goal, the work was divided into three main parts as defined briefly below and in greater detail in the following chapters.

The first section focuses on the importance of quality of single molecule techniques and the development of a custom designed fluorescence cross correlation spectroscopy platform to address outstanding deficiencies in commercial setups. The parameters and optical properties of homebuilt Fluorescence Cross Correlation Spectroscopy (FCCS) device were determined. The modified FCCS is characterized utilizing free dye solutions and fixed length double labeled oligonucleotides. Fitting parameters were informed by the optical design. Traditional Gaussian model fitting is compared to modified numerical fitting methods, improving on the determination of realistic and quantifiable parameters.

The platform is then used to expand upon the current knowledge of polymer dynamics. DNA samples ranging from 500 to 6000bp were created using PCR and end labeled with two fluorophores using custom designed PCR primers. Expanded two color FCCS measurements were performed in solution. Diffusion, mean square displacement (MSD), radius of gyration and other polymer dynamics were determined utilizing defined calibration parameters. Numerical fitting methods were expanded upon to incorporate theories of polymer dynamics. Fitting methods were compared to traditional Gaussian fitting models. Novel approach for extracting the MSD from the auto- and cross-correlation functions is developed. Polymer scaling exponents were compared to traditional theories of polymer dynamics.

Finally, the ultimate goal of this work was to extend the characterization of double-labeled DNA samples into nano-fabricated channels. Nano-slit (shallow, wide channels) chips were designed and fabricated in borosilicate glass utilizing standard nanofabrication techniques. Multiple strategies for bonding/sealing nanostructures were tested, with a clear nanofabrication protocol developed, albeit with limited consistency. Both freely diffusing fluorophore and double-labeled DNA oligonucleotides were preliminarily tested within nano-slits utilizing the FCCS previously designed and characterized. Theoretical and fitting models were adjusted to account for the two-dimensional dynamics and laterally confined measurement volume. Establishing the nanofabrication protocol and the proof of principle for the FCCS platform opens the door for future work addressing the internal polymer dynamics of DNA under confinement.

II.   Background and Significance

A. Motivation

The motions of polymers play an important role in the development of separations technologies. One cannot separate DNA within solutions. The gold standard of separations in molecular biology is gel electrophoresis, where driving the molecules through porous gels using electric fields can separate DNA molecules ranging from 10bp to over 1 Mbp.[1, 2] Despite the success of this technique, a complete understanding of the mechanisms of separations is lacking. Additionally, although some basic studies fluorescence microscopy studies of lambda DNA have been performed in nanoslits, separations technology based on topology remains limited. [3-9]

Gel electrophoresis, a standard scientific technique, employs highly cross-linked polymer gels to separate DNA based on size; however, it is limited in its size resolution (several hundred base pairs) and ability to separate based on topology (e.g. circular, linear). This poses significant problems for being able to perform high-throughput DNA analysis or genetic sequencing, as these applications require very tight size distributions and topological constraints.

Addressing these limitations requires being able to improve our understanding of loop (hernia) formations. It has been shown that, under some conditions, The formation of these loops governs the diffusion and reptation of linear DNA through electrophoretic gels.[10, 11] Additionally, although basic isolation of linear and circular DNA mixtures is relatively straightforward, separating mixtures of circular DNA remains difficult or their behavior in dense environments. Some theoretical studies have addressed the effects of loop formation on reptation.[12] The formation of loops also plays a role in a wide range of prokaryotic and eukaryotic organisms, with the dynamics of threading and looping occurring during DNA compaction and DNA interaction with enzymes.[13-18]

The development of our single molecule platform experimentally studying DNA dynamics both in solution and under nano-confinement would support efforts to improve the speed and dynamic range of DNA separation. Improvements in separation would in turn make medical diagnostics and genetic sequencing cheaper, faster, and more reliable.

Because of the aforementioned dynamic limitations of previous studies, we chose to apply Fluorescence Correlation Spectroscopy (FCS) to improving our understanding of polymer dynamics under nano-confinement. In order to study polymer dynamics on a single molecule level utilizing FCS, it is critical to be able to reliably quantitatively determine and carefully characterize the confocal volume. Previous research by other groups looked at DNA dynamics utilizing single color FCS setups.[19-21] Keeping these limitations in mind, we developed our single molecule Fluorescence Cross Correlation Spectroscopy platform with specific design parameters to help address the questions in polymer dynamics with the ultimate goal of developing more robust separations technologies.

The following sections will provide an introduction and explanation of DNA, the basic theory of polymer dynamics, both in solution and under confinement, current imaging methods, basic theory behind FCS, and future perspective applications of the platform developed herein.

B. Perspectives - Applications to Biological and Biomedical Problems

Developing a reliable, well-characterized single molecule platform for measuring the dynamics of DNA would help experimentally verify and elucidate the theories of polymer physics and their applicability to questions of biological and biomedical importance. Therefore, there are many areas of research where the results of this work and its future further development would impact. Below is a sampling of some additional areas of interest that are beyond the scope of the current thesis work.

One area of interest relates to the importance of topological constraints in DNA condensation and packaging in viruses. The DNA molecules of bacteriophages are typically larger than 10kbp with radii of gyration greater than 300nm in free solution; however, the size of the viral capsid is smaller than 50nm. As a result the DNA form highly supercoiled and complicated knots.[22, 23] Such strong confinement severely restricts DNA conformation and dynamics. Many recent studies have begun to elucidate the effects of confinement on DNA structure and dynamics; however, more work remains.[4, 8, 24, 25]

Another area of research that would benefit from advanced single molecule techniques such as those proposed would be protein search. Many cellular processes rely heavily on the interaction of proteins with specific sequences on the DNA molecules [26]. The remarkable aspect of these DNA-protein interactions is the fact that, despite the large amount of non-specific and compacted DNA within a cell ($> 10^6$ bp), proteins are able to quickly locate and bind to their specific targets, typically 10-20bp in size. The binding of transcription factors occurs much more rapidly than can be accounted for by simple diffusional collisions between protein and DNA [27, 28]. In response to these findings, Berg and von Hippel developed an analytical model of target search known as facilitated diffusion.[29, 30] The model presumes that the search involves a mix of 3D diffusion and 1D sliding along the DNA backbone through a series of non-specific interactions. Significant theoretical and computational effort has been spent addressing different aspects of the protein search problem.[31-35]

The quantitative aspects of these search functions are of considerable biological interest since they underpin key steps in all types of cellular functions important for normal function and the development of disease states such as cancer. Characterizing the different phenomena involved with biomolecular interactions and correlating them with information relating to structure will increase our ability to associate molecular activity with function. Some experimental work has been done on the single-molecule level in vitro and in vivo. [36-40] Despite this, significant questions remain regarding the quantitative kinetics and dynamics of specific DNA-protein interactions, such as, can one accurately determine the location and movement of a protein along a DNA backbone.

C. DNA and Polymer Dynamics

DNA serves as the molecular backbone of life with all of the instructions necessary to assemble every protein needed by the cell carried in its code.[41] The molecule is structured in a double helix with two deoxyribose backbones joined by nitrogenous bases.[42] The four bases are

adenine, cytosine, guanine, and thymine. The bases have complementary pairs and join through hydrogen bonding: adenine to thymine and guanine to cytosine.

In its normal helical structure, the diameter of the strand is about 2nm and one helical turn is comprised of about 10 base pairs over a length of 3.4nm. Although the DNA molecule can be considered rod-like, over longer base-pair lengths, the chain begins to curve randomly. The bending and curving of DNA results in the formation of a random coil as the molecule resists elongation. It does so because the random-coiled conformation maximizes the entropy of the polymer [43].

Within the cell, proteins fold DNA into chromosomes, with the total set forming the genome. The length of the human genome is on the order of three billion base pairs, with single genes comprising several kilobase pairs.

Studying the polymer dynamics of DNA is critical to furthering our understanding of how fundamental biological processes operate and what role topological constraints have. Examples include, but are not limited to, gene regulation, cell division, threading and transport through pores, and DNA condensation.

DNA is a natural choice for studying polymer dynamics not only because of its critical biological role, but also because it is a model polymer, capable of assuming different topologies (e.g. linear, circular) and is well characterized. The availability of experimental techniques, such as PCR, allows for the mono-disperse production of DNA of a fixed length simplifying it's scientific application. This is critically important in polymer dynamics as the length of the molecule strongly affects the dynamics at play.[44] The process of attaching fluorophores to DNA can be approached through multiple means and is well understood, simplifying fluorescent imaging of small molecules.[45]

There are many questions that remain regarding the polymer dynamics of DNA that can now be experimentally tested thanks to the development and availability of new single molecule detection and nanofabrication techniques. In order to expand upon the polymer dynamics of DNA, it is important to review some of the basics regarding the currently understood theories.

D. Polymer Physics Basics

A polymer is defined as a chain of many discrete segments, or repeating monomers. The total number of segments is defined as the total length of the polymer and known as the contour length L. The length of each segment is defined as the Kuhn length or twice the persistence length, $l_k = 2l_p$, with the persistence length as length over which the polymer can be considered "stiff" or inflexible.[46, 47] The persistence length can vary greatly from polymer to polymer, ranging from $3\,nm$ for some synthetic polymers to over $25\,\mu m$ for other biopolymers with double stranded DNA being about 150bp or $50\,nm$.[48, 49]

There are several models for describing the motion of a polymer. The simplest model is that of a freely jointed chain (FJC). A FJC is composed of a series of N connected links of equal length each with their own independent orientations, as shown in Figure 1. Each link of the chain

undergoes a "random walk" through space. The two most common ways by which the size of a polymer is described are the end-to-end length, R, and the radius of gyration, R_g. The mean square end-to-end length is defined as:[46] $\langle R^2 \rangle = Nb^2$ The entropy of the polymer increases with decreasing end-to-end distance with a stretched polymer behaving like a spring displaced about its equilibrium position, as demonstrated by Bustamante et al.[50] The radius of gyration represents the geometric average of the length and stiffness of the polymer. For a random walk, $R_g = \frac{1}{6} b N^{\frac{1}{2}}$
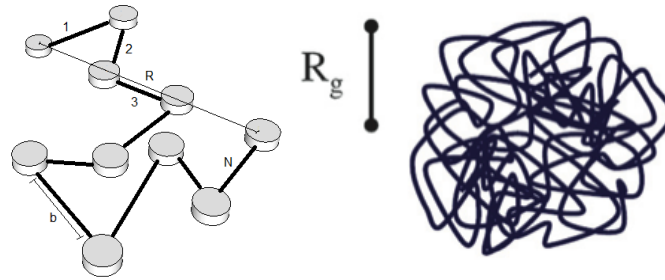
Figure 1 – Polymer of N segments of length b with end-to-end length R (left)[1] and radius of gyration (right)[51]

In reality, the polymer chain link orientation is not entirely random, as it cannot bend back on itself, resulting in a self-avoiding random walk. This results from excluded volume and electrostatic effects. A polymer whose links cannot bend randomly is defined as swollen and takes up more space in a solution than if it were a truly random walk. The correlation of the angles between links is related to the center of mass of the polymer. One can use Flory's mean field approach to determine the Flory exponent, ν, or excluded volume parameter, which relates the mean radius of the polymer to the number of chains and their length.[52] This approach minimizes the Flory free energy with respect to R. According to this approach, the Radius of gyration scales as $R_g \sim N^\nu$. In the FJC model, $\nu = \frac{1}{2}$, which is also known as a theta solvent.[46] For a bad solvent, $\nu = \frac{1}{3}$. Including excluded volume effects (good solvent case), $\nu = \frac{3}{5}$, while a more rigorous analysis reaches a value of $\nu = 0.588$. Radius of gyration scales as $R_g \sim N^\nu$ is typically defined as $R_g \approx b N^\nu$.[46]

The longer the DNA chain, the more important the excluded volume interactions become as extra repulsions are introduced, which swell the chain. Therefore, the type of solvent a polymer is in heavily affects the radius of gyration and persistence length.[53] In a bad solvent, polymer behaves like a solid sphere, while in a good solvent it is larger and swells. When immersed in a typical buffer such as 1x Tris Borate Sodium EDTA (TBE), DNA will form a 3D blob in free solution (figure 1). For longer polymers in good solvent, the theory estimates that $R_g \sim L^{\frac{3}{5}} = \frac{5}{\sqrt{176}} b N^{\frac{3}{5}}$.[46] A good experimental approximation was shown by Smith et. al, as $80nm * (n \ in \ kbp)^{\frac{3}{5}}$.[47, 54] While for a shorter, stiffer polymer $R_g = \frac{Nb}{\sqrt{12}}$, with the Flory parameter, $\nu = 1$.

While the models discussed above describe the static behavior of polymers, in the context of

dynamics, there are two primary theories, Rouse and Zimm.[46, 55] These both predict a distribution of relaxation times or breathing modes that polymers undergo within a solvent. The Rouse model essentially treats the polymer as a series of beads and springs, while the Zimm model introduces the additional complexity of hydrodynamic interactions between the beads. As a result, the effect of polymer size on diffusivity is weakened. For a single polymer, the diffusivity is shown to scale with a negative power law with respect to molecular mass with a (approximately) -1 and $-\frac{3}{5}$ exponent for the Rouse and Zimm regimes, respectively. The relaxation time scales with the exponents $1 + 2v$ and $3v$ for the Rouse and Zimm regimes, respectively. Typically, the Zimm model has been shown to be more accurate, given it's additional assumptions and experimental results with larger polymers (e.g. DNA > 20kbp) has largely followed these power laws, although their still exists controversy regarding the exact power laws and when the transition between different regimes occurs.

E. DNA under confinement

When constraining a polymer to a slit whose smallest dimension is smaller than twice the radius of gyration of the polymer, the polymer has to deform in order to entire the nanostructure.[2, 56] A nanostructure can be either a capillary, channel, slit or pore matrix. A nano-slit is defined as a structure where there is strong confinement in one dimension, effectively limiting the polymer to a 2D system. A nano-channel has strong confinement in two dimensions. Following the same approach to minimizing the Flory free energy, one obtains a scaling behavior in a 2D system, such as a nano-slit, of $R \approx N^{\frac{3}{4}}$.[56] Recent experiments directly measuring radius of gyration of DNA adsorbed to a surface were in agreement with the theoretical 2D scaling exponent for a self-avoiding walk.[57]

To describe the subsequent deformation, two theories are employed [44, 58]. The choice of model is based on the relation of persistence length to the diameter of the nanostructure, as shown in fig. 2 [2, 8, 59].

In the Odijk regime, known also as the deflection model, defines the DNA molecule as having a persistence length longer than the diameter of the channel. As a result, the DNA molecule is forced to elongate more as it deflects off of the wall and changes its direction. One can define a deflection length over which the polymer can be assumed to be a rigid rod or segment. When the structure has differing diameters of height and width, one uses a geometrically averaged diameter for determining the deflection length.
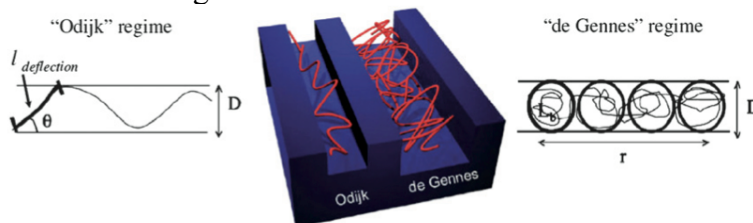
Figure 2[8, 59] - Schematic of the two regimes for DNA confinement in nano-channels: a) de Gennes D >> A b) Odijk D << A, where A is persistence length, D diameter of the nano-channel

With the de Gennes regime, the diameter is sufficiently large in the two directions of height and width that the confined DNA is viewed a chain of blobs.[60, 61] In contrast to the deflection length, a polymer in this regime has a characteristic contour length, defined as the average length of each blob on the chain. The molecule is extended over a length r (as seen in fig 2) as a result of the repulsion between blobs.

Additionally, when DNA is forced to enter a nano-channel under the influence of an electric field, it has a certain probability of entering the channel by a hairpin rather than by an end, resulting in the confinement of an unfavorably high energy state of the molecule; however, additional study is needed to understand the exact mechanics and probabilities for the entrance of DNA into nanochannels.[62] It remains unknown exactly how a polymer like DNA would thread through a nano-channel or nano-pore, whether by ends or mid-segments.

One of the dominant mechanisms of polymer diffusion in nanostructures is known as entropic trapping. Entropic trapping occurs when a polymer encounters a channel with a diameter less than twice the radius of gyration.[63] Typically, a polymer tends to move towards regions of higher entropy to minimize its free energy. This has been observed experimentally by Nykypanchuk et. al, with DNA recoloring after being forced into a low-entropy region.[64]

F. Single DNA Imaging Methods

Despite the contour length of DNA typically being on the order of microns, the molecule's axial diameter is on the order of a couple nanometers. Therefore, one is unable to resolve single DNA molecules utilizing brightfield microscopy. In order to study, verify, and improve the theories of polymer dynamics as presented by Doi and Edwards, fluorescence techniques have been employed.

The most common method for labeling DNA for use with standard fluorescence microscopy involves staining of the entire molecule with YOYO (oxazole yellow dimer), which has a 100 to 1000 fold fluorescent enhancement on binding to DNA.[65] When staining DNA with a dye such as YOYO, the length of the molecule extends significantly – up to 50% of the original, linear chain length.[54] The setup of a basic epifluorescence microscope is shown in figure 3.[66] A light source passes through an objective and illuminates the sample with the excitation light (fluorescence) traveling in the opposite direction through a dichroic mirror to a detector. This type of setup minimizes backscattered excitation light with the general success of a fluorescence setup being dependent on the ability to discriminate effectively between excitation and emission light.

A major consideration when trying to image single DNA molecules is the limitations of the optical resolution of the experimental setup, which is determined primarily by the numerical aperture (NA) of the objective lens. Typical objectives range between 1.4 (oil immersion) and 1.2 (water immersion). The theoretical limit of the spatial resolution is found by $R = \frac{0.61\lambda}{NA}$. Therefore, with an NA of 1.2 and a $\lambda = 488nm$, one obtains a $R \approx 250nm$, meaning that two objects or points separated by a distance smaller than R cannot be resolved. Given that DNA typically bends on a length scale approximately five times less than the calculated limit, DNA appears in successful fluorescence images as a bright blob. Single molecule diffusion and

transport can still be tracked by determining precisely the location of the centroid of an isolated molecule and proper image processing.[67]
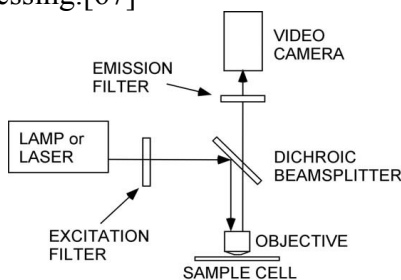
Figure 3[66] – Schematic of basic Fluorescence microscopy setup

A challenge inherent with any fluorescence techniques is the tendency of many dyes to photobleach, a result of photo-induced chemical damage. This damage can also damage the DNA molecule itself, breaking it up. The use of additives such as β- mercaptoethanol in buffers or newer dyes such as the atto series helps to minimize these effects.

G. Fluorescence Correlation Spectroscopy – A Primer

The previously described single molecule fluorescence techniques have allowed for the direct visualization and measurement of individual polymer; however the imaging approach is still limited to molecules larger in size than the diffraction limit of the optics in use.[68-70] Fluorescence correlation spectroscopy has been proposed as a technique that could resolve dynamics below the diffraction limit, where many FCS based studies of polymer dynamics have been undertaken to measure the conformational dynamics of single and double stranded DNA molecules.[20, 21, 71-74] Typically, for fluorescence correlation spectroscopy measurements, a DNA molecule is single end labeled with a single fluorophore such as Rhodamine 6G or Alexa Fluor 488 using custom oligonucleotides and polymerase chain reaction.[19] There has been some debate as to whether FCS can truly resolve below conformational dynamics of single molecules below the diffraction limit; however, this discussion and the application of a two color FCCS system to address this issue is followed up in **Chapter V.**[75]

Fluorescence correlation spectroscopy (FCS) was developed more than 40 years ago.[76, 77] It saw a resurgence in use and utility following application of a confocal illumination setup in 1993 by Rigler et al.[78] Since then, FCS has become an invaluable tool for measuring the diffusion of molecules, binding and reaction kinetics, single molecule photo physics, and conformational dynamics of proteins.[79-83]

The basic principle behind FCS relies on the fluctuation of the fluorescence signal intensity about the mean. What distinguishes FCS from most other fluorescence related techniques is that the primary interest lies not in the amplitude of the fluorescence intensity, but rather the random intensity fluctuations around the mean that result from thermal noise. FCS does not perturb the system being studied. It utilizes the fact that, on a molecular level, the equilibrium states are highly dynamic and that the smaller the observed volume is, the larger the fluctuations that are observable.

A basic setup is illustrated in figure 4.[84]A collimated laser beam, focused by an objective lens into a diffraction limited confocal volume, excites a sample. The confocal optics are crucial for creating a small observation volume that, knowing the optical parameters of the system, should be able to be well-characterized. This is crucial in the development of the theory elaborated on in the following chapter.
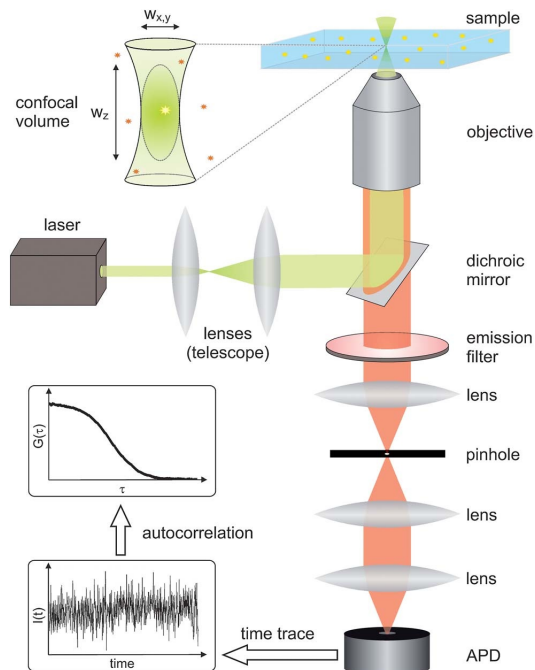
Figure 4[84] – Typical FCS Setup and resultant time trace and auto-correlation curve (insets, left)

Part of the light emitted from the confocal volume is collected by the same objective and separated from the excitation light with a dichroic mirror and emission filter. Detection is performed by an avalanche photo diode (APD). Through the use of a pinhole, most of the light not originating from the confocal volume is blocked (figure 5). A typical confocal volume is on the order of 1 femtoliter.
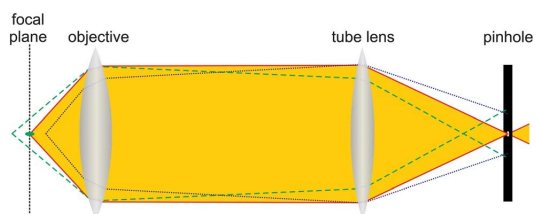
Figure 5[84] – Effect of pinhole on axial resolution of FCS setup

The confocal observation volume, or the actual measurement volume that is seen by the detectors, is approximated by the product of the molecular detection function (MDF) and the optical collection efficiency function (CEF). More detail about these two functions and their forms will be provided in the next chapter.

Molecules diffuse in and out of the volume, which result in fluorescence fluctuations. The timescale of these fluctuations provides information on the kinetics that underlie processes at

play. In a standard FCS measurement one uses fluorescently tagged molecules in order to glean information as to what the concentration within a particular volume is. Knowing both of these pieces of information, one can use correlation analysis to determine various dynamic properties of the molecules in question, namely diffusion. Depending on the molecular system being studied and the method of fluorescent tagging, other fluctuations can also be detected. These include, but are not limited to, directed flow, chemical equilibrium, intersystem crossing between singlet and triplet states, and non-radiative fluorescence resonance energy transfer (FRET).

As fluorescent particles diffuse in and out of the confocal detection volume, as illustrated in figure 4, an intensity time trace is generated. The autocorrelation function (ACF) is a measure of whether the intensity at a particular time point, t, is correlated with any later time point, $t + \tau$, and can be expressed as follows:

$$G(t) = \frac{\langle \delta I(t) * \delta I(t+\tau) \rangle}{\langle I(t) \rangle^2} = \frac{\langle I(t) * I(t+\tau) \rangle}{\langle I(t) \rangle^2} - 1 \qquad \text{(II-1)}$$

where $\delta I(t) = I(t) - \langle I(t) \rangle$, is the deviation from the mean intensity.

Any further discussion requires a careful understanding of correlation analysis. It is instructive to begin the discussion on what is a correlation? A correlation itself results when the relationship between two sets of measurements is not random. An example of a correlation among three intensities I_1, I_2, I_3 is shown below. From a cursory overview, it becomes apparent that there is a direct, linear relationship between I_1 and I_2, but no relationship between I_1 and I_3.
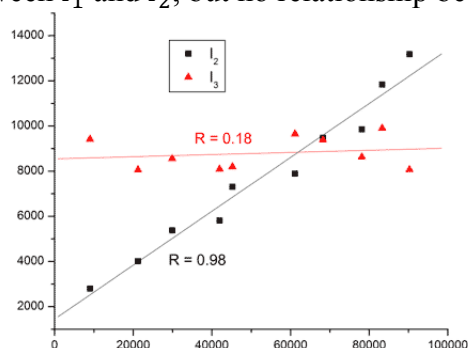
Figure 6[85] – Example of Correlation. I_1 plotted along x axis, I_2, I_3 along y-axis

An autocorrelation analysis performs the same correlation test with the key difference being that in the previous example I_1 would be plotted against itself. Doing so, one would obtain the following perfect correlation and wonder what the point was:
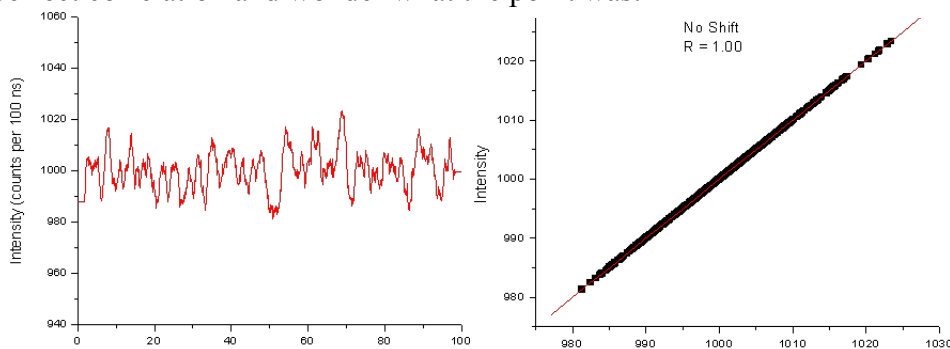
Figure 7[85] – Example Intensity fluctuation and resulting correlation

However, the intensity fluctuation example in Figure 7 does not seem to be perfectly random. The amplitude is randomly distributed, but the distribution of the amplitudes is not, indicating a possible relationship between the characteristic length scale between the peaks and the valleys. Taking the same data in figure 7, one can re-plot the correlation of the intensity with itself, shifted by set counting intervals. As the shift in time increases, the correlation decreases. One can plot the correlation coefficient explicitly as a function of the time shift to obtain figure 9, which results in a rudimentary autocorrelation function that represents the probability that a signal at an initial time t is correlated with a signal measured at some later time, $t + \tau$.
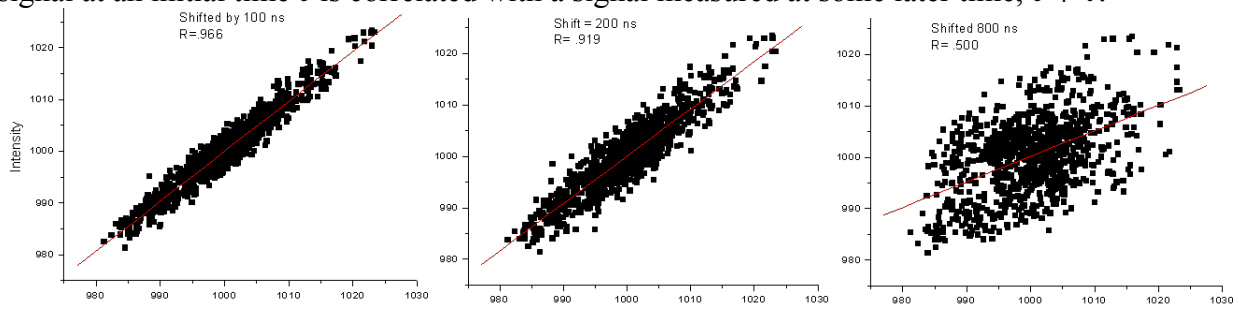
Figure 8[85] – Correlation of intensity fluctuation with itself, shifted in time
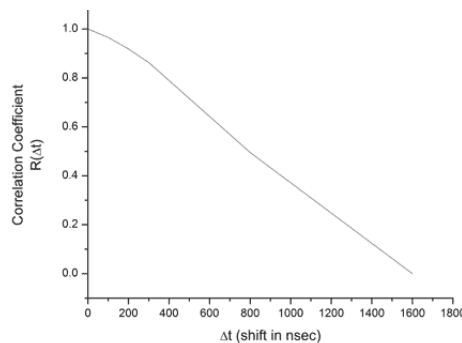
Figure 9[85] – Correlation versus shift in time for an example correlation curve (Figure 7) plotted against itself

To summarize, the autocorrelation function (ACF) is a measure of the probability that a fluctuation from the mean intensity caused by a photon detected at a time t is correlated with a photo detected at a later time $t + \tau$. An example of a normalized ACF is shown in figure 10.

12
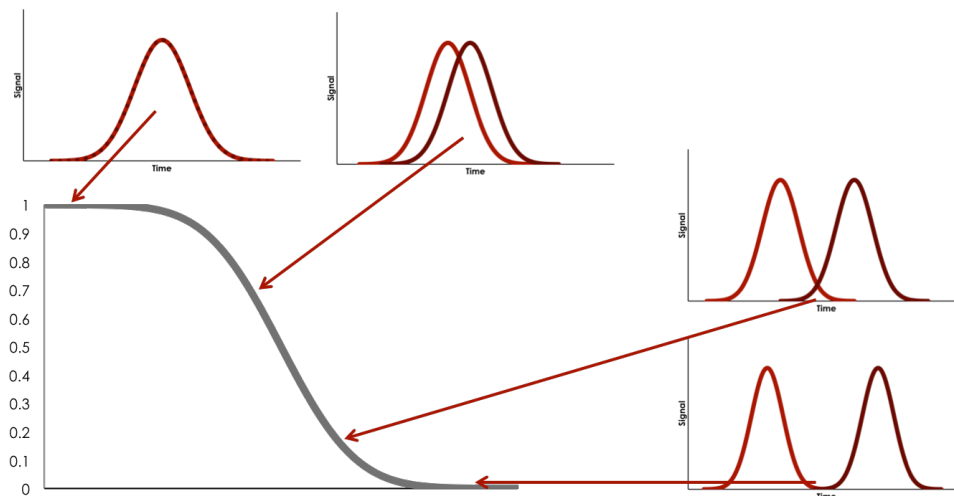
Figure 10 – Example normalized Autocorrelation curve and it's corresponding time shifted self-correlated observation volumes

If the two photos detected originated from the same molecule, they are correlated, resulting in a time-dependent component of the ACF. If the photons originated from background signal or from different non-interacting molecules, the photos are statistically uncorrelated and won't contribute to the shape of the ACF. Because the temporal behavior of the ACF is entirely determined by the correlated contributions of photons from individual molecules, FCS is a true singe molecule technique.

FCS functions on the principle that the number of molecules within the volume must be reduced so that each contributes significantly to the measured signal. Typically this means that experimentally concentrations on the order of nano-molar are most appropriate. As can be seen in figure 10, over shorter time scales, there are larger fluctuations. Conversely, over longer time scales there is zero fluctuation and an averaging of the intensity (figure 10).

The autocorrelation function contains information on all of the processes that cause intensity fluctuations. The inverse of the amplitude of the curve provides the concentration of molecules in solution (as related to the observable volume). The time at which the amplitude of the curve is half of the maximum provides the characteristic diffusion time of a molecule, which relate entirely to the underlying physics, chemistry, biology, etc.

Other dynamics can also be extracted depending on the complexity of the system under study. These include, but are not limited to, translational diffusion, rotational diffusion, and photo-physical effects (e.g. triplet state).[86, 87] All of these processes occur over many orders of magnitude of time (picosecond to seconds); therefore, it is convenient to plot the ACF logarithmically along the x-axis. The fitting of the experimentally derived autocorrelation function depends on defining an appropriate model for the sample system being measured. The simplest model assumes a 3D Gaussian confocal volume and focuses on calculating the translational diffusion of a molecule, which is typically observed as a drop in the autocorrelation function in the millisecond to second range[84, 88] :

$$G(t) = \frac{1}{N}\left(1 + \frac{t}{\tau_D}\right)^{-1}\left(1 + k^{-2}\frac{t}{\tau_D}\right)^{-\frac{1}{2}} \tag{II-2}$$

where N is the number of independently diffusing molecules in the confocal volume, τ_D the average diffusion time of the molecule through the volume, and k the structure parameter, which is defined as $k = \frac{\omega_z}{\omega_{xy}}$, where ω_z and ω_{xy} are the axial and radial diameters of the confocal volume. Typical values for the axial and radial diameters are approximately $1.5\mu m$ and 300nm, respectively. The amplitude of the ACF is determined by the concentration of molecules. The horizontal shift of the slope of the ACF is determined by the diffusion time of the molecule in question. This is further illustrated in figure 11. Best results are obtained when there is approximately on average one fluorescent molecule diffusing in the confocal volume at any one time, which translates to a solution concentration of about 1nM or less.
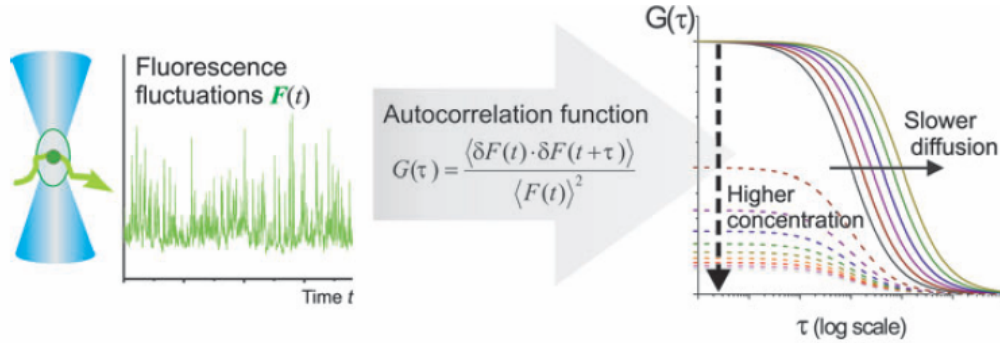
Figure 11 – Summary of ACF. Adapted from Bacia et. al.[89]

Current FCS experimental designs suffer from one or more the following limitations, including, but not limited to, one color detection, the presence photo-physical artifacts related to detector after-pulsing within the ACF, improperly characterized optics, and inconsistent and improper fitting parameters due to incorrect assumption of Gaussian focal volume.[87] Our aim throughout this research project was to address as many of these issues as possible through deliberate design and fitting methods and adapt them towards elucidating DNA dynamics.

III. Theory

Previous work regarding the fitting of ACFs has focused on Gaussian fitting models.[78, 81, 90, 91] Following from the molecule detection function (MDF), which accounts for both the excitation light intensity distribution and the collection efficiency, most earlier groups utilizing FCS began the derivation of the complicated integrals, but made the assumption of a 3D Gaussian approximation in order to simply the calculation, with the original assumption arising from a 1976 paper by Koppel et. al.[78, 92] This grossly oversimplifies and imprecisely represents the actual experimental situation. The first comprehensive studies pointing out the misconception regarding the 3D Gaussian approximation were presented by Hess and Webb and Enderlein et. al.[93, 94]

Many subsequent papers published utilizing FCS have relied on specific cases to force the fit, rather than taking into account the optical parameters of the system and the complete MDF, failing to include a collection efficiency function to take into account the detection optics. The use of a 3D Gaussian MDF assumption introduces arbitrary parameters, w_{xy} and w_z, the radial and axial extents of the confocal volume, respectively (figure 12). The related structure parameter, $k = \frac{w_z}{w_{xy}}$, which is frequently fit by those utilizing a 3D Gaussian model, often arbitrary in size and only ambiguously defined as recommended to be within a certain range (3-9).[89]
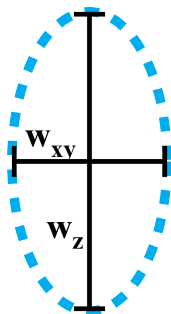
Figure 12 – Confocal volume illustrating w_{xy} and w_z

There is no straightforward way to relate to experimental parameters such as the numerical aperture of the objective or the characteristics of the laser-beam excitation and the confocal detection to these aforementioned fitting parameters. Therefore, misalignment of the optics or deviations of any other sources of optical aberration, which include cover slide thickness variation, optical saturation, or aperture position, are not taken into account. The importance of these parameters was illustrated by Enderlein et. al. where even slight changes in the aperture position resulted in significant changes in the shape of the confocal volume (figure 13).[87, 95]

Without being repeatable or relatable to experimental optical parameters, there is no way to quantitatively determine the confocal volume, which is critical for any two-color setup that requires clear information about volume for each color and their respective overlap. Thus, there exists an immense need for a fitting procedure that takes into account the optics of the experimental system in question.
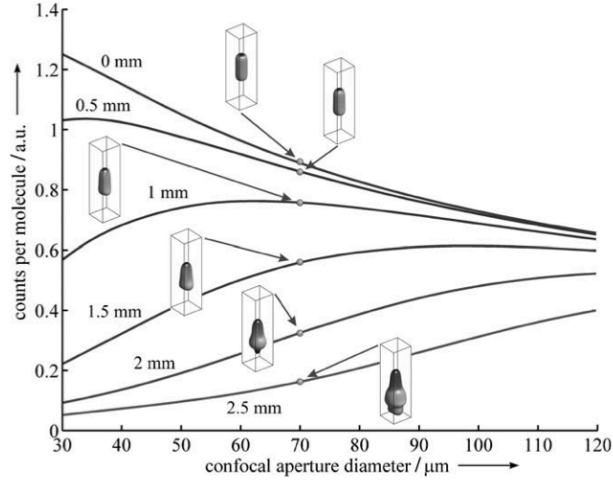
Figure 13 – Dependence of counts per molecule and MDF on the confocal aperture diameter for different aperture positions along axial axis (z). Adapted from Enderlein et. al. 2005.[87]

3D Gaussian Fitting

As illustrated in the background, the traditional 3D Gaussian fitting model takes the form[78],

$$G(t) = G_0 * \frac{1}{\left(1+\left(\frac{t}{\tau_D}\right)\right)\left(1+k^{-2}\left(\frac{t}{\tau_D}\right)\right)^{\frac{1}{2}}} + 1 \tag{III-1}$$

where G_0 is the inverse of the number of molecules within the confocal volume, $k = \frac{w_z}{w_{xy}}$ is the structure parameter, and τ_D the characteristic diffusion time of the molecule in question. As a result, a proper fit relies on the determination of a structure parameter, k, of which the many fitting situations are insensitive too. This prevents one from obtaining a proper determination of the confocal volume given the relation of the three parameters. τ_D is also related to the diffusion coefficient through the following relation, $D = \frac{w_{xy}^2}{4\tau_D}$. G_0 is also related to the confocal volume through the following relation,

$$G_0 = \frac{1}{N} = \frac{1}{V_{eff}CN_A} \tag{III-2}$$

where N_A is Avogadro's number and the effective volume is expressed as,

$$V_{eff} = \frac{1}{G_0*N_A*C} = \pi^{\frac{3}{2}}w_{xy}^2 w_z \tag{III-3}$$

The time correlation function (cross or auto) measured by FCS is:

$$G(\tau) = p_1 p_2 \iint d\vec{x}_1 \, d\vec{x}_2 P_\tau(\vec{x}_2 | \vec{x}_1) P_0(\vec{x}_1) \Phi_1(\vec{x}_1) \Phi_2(\vec{x}_2) \tag{III-4}$$

where x_1, x_2 are the positions of the fluorescent tag 1 and 2; P_0 is the probability distribution of a tag being at position x_1; $P_\tau(x_2|x_1)$ is the conditional probability to find tag 1 at x_1 at time 0 and tag 1 at x_2 at time τ. $\Phi_{1,2}$ is the profile of the laser focus intensity exciting tag 1 and 2. $p_{1,2}$ are the quantum efficiencies for fluorescence. For a freely diffusing particle $P_0=1$.

For a diffusive process, such as the thermal equilibrium being measured by the autocorrelation function in FCS, the conditional probability in equation (4) can be written in the form of a Gaussian:

$$P_\tau(\vec{x}_1|\vec{x}_2) = P_\tau(x_1|x_2)P_\tau(y_1|y_2)P_\tau(z_1|z_2) \tag{III-5}$$

$$P_\tau(x_{1i}|x_{2i}) = \frac{1}{\sqrt{2\pi\left\langle(x_{2i}(t+\tau)-x_{1i}(t))^2\right\rangle}}\exp\left(-\frac{(x_{2i}(\tau)-x_{1i}(0))^2}{2\left\langle(x_{2i}(t+\tau)-x_{1i}(t))^2\right\rangle}\right) \; ; \; i=x,y,z \tag{III-6}$$

Taking into account that for pure diffusion,

$$\left\langle\left(x_2(t+\tau)-x_1(t)\right)^2\right\rangle_t = 2D\tau \tag{III-7}$$

and that diffusion is equal in all three spatial directions, equation (III-7) results in a normalized conditional probability distribution of,

$$P_\tau(\vec{x}_2|\vec{x}_1) = \frac{1}{\sqrt{4\pi Dt}}e^{-\frac{(\vec{x}_2-\vec{x}_1)^2}{4Dt}} \tag{III-8}$$

$$P_\tau(\vec{x}_2|\vec{x}_1) = P(x_1|x_2)P(y_1|y_2)P(z_1|z_2) \tag{III-9}$$

$$P(x_1|x_2) = \frac{1}{\sqrt{2\pi\left\langle\left(x_2(t)-x_1(0)\right)^2\right\rangle}}e^{-\frac{(x_2-x_1)^2}{2\left\langle\left(x_2(t)-x_1(0)\right)^2\right\rangle}} \tag{III-10}$$

Given that probability for diffusion is equal for all three directions, one can integrate over each direction, x,y,z independently. For the 3D Gaussian model we assume that the laser foci are Gaussian with widths ω_{xy} and ω_z in the x-y plane and in z, respectively. Integrating over one of the dimensions gives:

$$\int\frac{1}{\sqrt{4\pi Dt}}e^{-\frac{(x_2-x_1)^2}{4Dt}}e^{-\frac{2(x_1^2+x_2^2)}{w_0^2}}dx_1dx_2 = \frac{\sqrt{\pi}}{2}\frac{w_0}{\sqrt{1+\frac{4Dt}{w_0^2}}} \tag{III-11}$$

which results in the classical analytical FCS correlation function for a 3D Gaussian beam,

$$\int\frac{1}{\sqrt{4\pi Dt}}e^{-\frac{(\vec{x}_2-\vec{x}_1)^2}{4Dt}}e^{-\frac{2(x_1^2+x_2^2+y_1^2+y_2^2)}{w_0^2}-2\frac{2(z_1^2+z_2^2)}{w_z^2}}d\vec{x}_1d\vec{x}_2 = \frac{\pi^{3/2}}{8}\frac{w_0^2}{\left(1+\frac{4Dt}{w_0^2}\right)}\frac{w_z}{\sqrt{1+\frac{4Dt}{w_z^2}}} \tag{III-12}$$

For cross-correlation with two different colors (focus sizes) this becomes,

$$\iint\frac{1}{\sqrt{4\pi Dt}}\exp\left(-\frac{(x_2-x_1)^2}{4Dt}\right)\exp\left(-\frac{2x_1}{w_1}\right)\exp\left(-\frac{2x_2}{w_2}\right)dx_1dx_2 = \frac{\sqrt{\pi}}{2}\frac{\sqrt{w_1w_2}}{\sqrt{\frac{w_1^2+w_2^2}{2w_1w_2}+\frac{4Dt}{w_1w_2}}} \tag{III-13}$$

17

however, the real intensity is defined as,

$$I(\vec{x}) = I_0 \frac{1}{1+\left(\dfrac{z}{z_R}\right)^2} e^{-\frac{2(x^2+y^2)}{w_0^2\left(1+\left(\frac{z}{z_R}\right)^2\right)}}$$

(III-14)

therefore the integral (III-11) turns into the following integral,

$$\int \frac{1}{(4\pi Dt)^{3/2}} \frac{1}{1+\left(\dfrac{z_1}{z_R}\right)^2} \frac{1}{1+\left(\dfrac{z_2}{z_R}\right)^2} e^{-\frac{(\vec{x}_2-\vec{x}_1)^2}{4Dt}} e^{-\frac{2(x^2+y^2)}{w_0^2\left(1+\left(\frac{z_1}{z_R}\right)^2\right)}} e^{-\frac{2(x^2+y^2)}{w_0^2\left(1+\left(\frac{z_2}{z_R}\right)^2\right)}} d^3x$$

(III-15)

we can perform this integral in x and y analytically,

$$\int \frac{1}{1+\left(\dfrac{z_1}{z_R}\right)^2} \frac{1}{1+\left(\dfrac{z_2}{z_R}\right)^2} e^{-\frac{(z_2-z_1)^2}{4Dt}} \frac{\pi}{4} w_0^2 \frac{1}{\left(\dfrac{4Dt(z_1^2+z_R^2)(z_2^2+z_R^2)}{w_0^2 z_R^4} + \dfrac{z_1^2+z_2^2+2z_R^2}{2z_R^2}\right)} dz_1 dz_2$$

(III-16)

The effective volume takes the form,

$$V_{eff}(\Delta z) = \pi^{3/2} \frac{w_{1xy}^2 + w_{2xy}^2}{2} \sqrt{\frac{w_{1z}^2 + w_{2z}^2}{2}} \exp\left[-\frac{2\Delta z^2}{w_{1z}^2 + w_{2z}^2}\right]$$

(III-17)

Numerical Methods for Fitting

Although the Gaussian fitting model provides some information regarding simpler systems in FCS, it's utility falls apart when measuring more complex systems such as a two color double-labeled oligo. The assumption of a 3D Gaussian confocal volume, originally made by Koppel et. al. in 1976, fails to appropriately account for the separation of the in the axial direction of the two color confocal volumes and the resultant overlap (cross correlation volume).[92]

Enderlein et. al. developed a numerical fitting model that calculates a more realistic confocal volume based on the proper molecular detection function (MDF), which takes into account both the excitation optics and the detection optics. Here, we adapt Enderlein's method for application towards FCCS.[87]

In fluorescence correlation spectroscopy we measure the cross-correlation function of the detected light intensities. For single color FCS $I_1=I_2$ and g(t) becomes the intensity autocorrelation function.

$$g(t) = \left\langle I_1(\tau) I_2(\tau+t) \right\rangle_\tau$$

(III-18)

Specifically for diffusing molecules with a diffusion coefficient D we can write

$$g(t) = g_\infty + \varepsilon_1\varepsilon_2 c \frac{1}{(4\pi Dt)^{3/2}} \int_{-\infty}^{\infty} d\vec{r}_1 \int_{-\infty}^{\infty} d\vec{r}_2 U_1(\vec{r}_1) \exp\left[-\frac{(\vec{r}_2 - \vec{r}_1)^2}{4Dt}\right] U_2(\vec{r}_2)$$

(III-19)

where $c = \frac{n}{V}$ is the number concentration of molecules, U_1 and U_2 are the molecule detection functions (MDF) for each detection volume (probability of detecting a photon from a molecule at position r), ε_1 and ε_2 are factors to describe overall excitation power and detection efficiency, and

$$g_\infty = \varepsilon_1\varepsilon_2 c^2 \int dr U_1(r) \int dr U_2(r)$$

(III-20)

The MDF itself is a product of the Intensity distribution of the focus and the optical Collection Efficiency function (CEF) that describes the effect of the confocal pinhole in the detection pathway.

$$U(\vec{r}) = I(\vec{x},z)CEF(\vec{x},z)$$

(III-21)

The laser focus normalized intensity distribution is best described by a Gaussian beam profile:

$$I(\vec{\rho},z) = \frac{1}{w^2(z)} \exp\left(-\frac{2\rho^2}{w^2(z)}\right)$$

(III-22)

where P is the laser power and w(z) is given by

$$w(z) = w_0 \left[1 + \left(\frac{\lambda_{ex} z}{\pi w_0^2 n}\right)^2\right]^{1/2}$$

(III-23)

where w_0 is the minimum beam waist of the Gaussian beam which is determined by the numerical aperture of the objective, n is the index of refraction of the immersion liquid and λ_{ex} is the wavelength of the laser.

The optical Collection Efficiency function (CEF) is the convolution of the Point Spread Function (PSF) with the transmission function of the pinhole in the semi-geometric approximation,

$$CEF(\vec{\rho},z) = \int_A \frac{disc\left(\left\|\vec{\xi} - \vec{\rho}\right\| / R(z)\right)}{\pi R^2(z)} d\vec{\xi}$$

(III-24)

integrated over the area A of the pinhole aperture's image in object space. where the integration

is carried out over the area A of the pinhole of radius a, which is defined as the real radius of the pinhole divided by the magnification. Essentially, it is the radius of the confocal aperture as seen from above the objective.[87, 96] Here, disc denotes a step function (1 for arguments smaller than 1 and 0 otherwise).

R(z) has a similar form to (III-23)

$$R(z) = R_0 \left[1 + \left(\frac{\lambda_{em} z}{\pi R_0^2 n} \right)^2 \right]^{1/2}$$

(III-25)

where R_0 represents the resolution limit of the objective and λ_{em} is the wavelength of the fluorescence emission.

In fluorescence correlation spectroscopy equation III-24 can be further simplified considering that the detection pinhole image in object space (with radius a) that are typically used is larger than R_0. This means that the laser intensity distribution falls off quicker than the CEF in ρ and therefore we can remove the ρ dependence in the CEF by setting ρ=0, resulting in the exact semi-geometric form

$$CEF(\vec{\rho} = 0, z) = \begin{cases} 1 & a > R(z) \\ \dfrac{a^2}{R^2(z)} & a \le R(z) \end{cases}$$

(III-26)

As an alternative and to simplify numerical integration of eq.2, Dertinger et al. approximate the CEF by[96]

$$CEF(\vec{\rho} = 0, z) = 1 - \exp\left(-\frac{2a^2}{R^2(z)} \right)$$

(III-27)

which we will call $\kappa(z)$. A comparison of the differences between III-26 and 27 is illustrated in Figure 14.
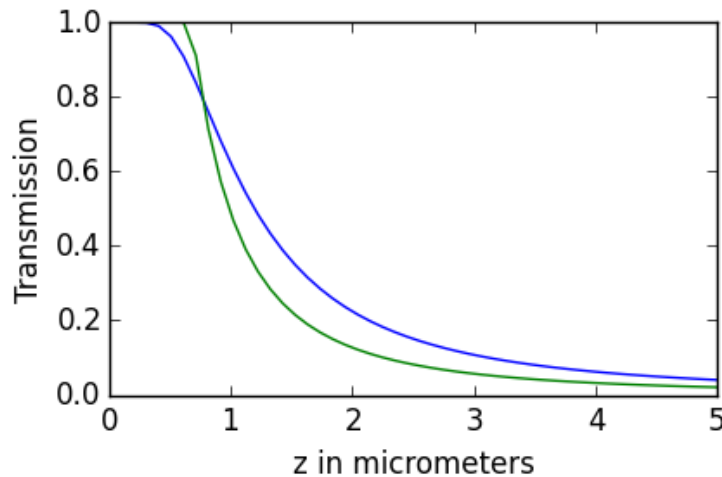
Figure 14 – Comparison of the Optical Collection efficiency function calculated in the semi-geometrical approximation (III-26 / green) and its analytical approximation (III-27 / blue) for a pinhole radius of a=0.522μm, R_0=170nm, n=1.33, and λ_{em}=519nm.

Using either form (III-26 or III-27), the MDF becomes simply:

$$U(\vec{\rho},z) = \frac{\kappa(z)}{w^2(z)} \exp\left(-\frac{2\rho^2}{w^2(z)}\right)$$
(III-28)

Following Dertinger et al., the integral in (III-19) can be expressed as[96]

$$g(t) = g_\infty + \frac{\varepsilon_1 \varepsilon_2}{4} c \sqrt{\frac{\pi}{Dt}} \int_{-\infty}^{\infty} dz_1 \int_{-\infty}^{\infty} dz_2 \frac{\kappa_1(z_1)\kappa_2(z_2)}{8Dt + w_1^2(z_1) + w_2^2(z_2)} \exp\left[-\frac{(z_2 - z_1)^2}{4Dt}\right]$$
(III-29)

This expression can only be evaluated numerically and it is convenient to make a change of variables as follows,

$$\xi = \frac{z_2 - z_1}{2\sqrt{Dt}}, \eta = \frac{z_2 + z_1}{2}$$
(III-30)

which turns (III-29) into

$$g(t) = g_\infty + 2\varepsilon_1 \varepsilon_2 c \sqrt{\pi} \int_0^{\infty} d\xi \int_0^{\infty} d\eta \frac{\kappa_1(\eta - \sqrt{Dt}\xi)\kappa_2(\eta + \sqrt{Dt}\xi)}{8Dt + w_1^2(\eta - \sqrt{Dt}\xi) + w_2^2(\eta + \sqrt{Dt}\xi)} \exp\left[-\xi^2\right]$$
(III-31)

the integral over ξ can be evaluated by using Gauss-Hermite quadrature whereas the second integral over η is evaluated by Romberg integration using a finite upper limit for integration that is determined by that the integral does not change when increasing the upper limit further. This can be done because both κ and w are rapidly decaying functions.

It is important to note that while the function in III-31 seems to have more variables than a typical Gaussian model, most of them are fixed during fitting as they relate to specific optical characteristics of the system in question. Therefore, if a design within another custom FCCS system utilizes different focusing lenses for the emission optics, that can be accounted for appropriately.

In a typical experimental setup, because of chromatic aberration, the foci of the two colors will appear at different positions in z. To account for this, we have to include a parameter that reflects this difference. The importance of this becomes crucial when attempting to fit the cross correlation curves in FCCS. The following integral can be evaluated in a similar fashion as the previous in (III-31); however, the integrals must be calculated from minus infinity to plus infinity since the integrant is no longer symmetric in ξ or η when taking into account Δz,

$$g(t,\Delta z) = g_\infty + \frac{\varepsilon_1 \varepsilon_2}{2} c \sqrt{\pi} \int_{-\infty}^{\infty} d\xi \int_{-\infty}^{\infty} d\eta \frac{\kappa_1(\eta - \sqrt{Dt}\xi + \Delta z)\kappa_2(\eta + \sqrt{Dt}\xi)}{8Dt + w_1^2(\eta - \sqrt{Dt}\xi + \Delta z) + w_2^2(\eta + \sqrt{Dt}\xi)} \exp\left[-\xi^2\right]$$
(III-32)

From fitting (III-31) to experimental FCS curves, we can determine the concentration of the fluorescence molecules in solution and its diffusion coefficient. This is typically accomplished by determining the normalized autocorrelation function:

$$G(t) = \frac{\left\langle I_1(\tau) I_2(\tau + t) \right\rangle_\tau}{\left\langle I_1 \right\rangle \left\langle I_2 \right\rangle}$$ (III-33)

where the denominator is equal to g_∞ (III-20) with the consequence that $G(\infty)=1$ and that the second term in eq. 14 and 15 is proportional to $\frac{1}{c}$. This second term is commonly written such as that for $t = 0$ the amplitude is equal to $\frac{1}{N}$ or $\frac{1}{V_{eff}C}$ where N is the number of molecules in the effective focal volume V_{eff}. In our case, the focal volumes can be determined by integrating III-31 and III-32 at $t = 0$ and dividing by g_∞ which cancels ε_1 and ε_2 and makes the result independent of illumination intensity and quantum efficiencies. For the autocorrelation V_{eff} calculates as:

$$V_{eff} = \frac{\pi \left(\int\limits_0^\infty dz \kappa(z) \right)^2}{2 \int\limits_0^\infty \frac{\kappa^2(\eta)}{w^2(\eta)} d\eta}$$ (III-34)

whereas for the cross-correlation with Δz

$$V_{eff}(\Delta z) = \frac{\pi \left(\int\limits_0^\infty dz \kappa_1(z) \right)\left(\int\limits_0^\infty dz \kappa_2(z) \right)}{2 \int\limits_{-\infty}^\infty \frac{\kappa_1(\eta + \Delta z)\kappa_2(\eta)}{w_1^2(\eta + \Delta z) + w_2^2(\eta)} d\eta}$$ (III-35)

An important aspect that differentiates this form from the traditional 3D Gaussian approach to fitting correlation functions in FCS is that the intensity profile is Gaussian in x and y but Lorentzian in z. This also is not an entirely accurate picture. Because of the complicated shape, that is why a numerical fitting model is most appropriate for obtaining a realistic volume and radial waist, which are informed by the optical characteristics of the system.

In contrast to the Gaussian fitting model, with a fixed diffusion coefficient and concentration, one is able to fit for w_{xy} and an optically based parameter R_0. These fits are consistent and relatable to the alignment of the various optical properties of the aforementioned FCCS system, with the model incorporating parameters such as wavelength, confocal aperture, and the index of refraction.

Using equations III-17 and III-35, one can compare the effect of the axial separation (Δz) versus the expected effective volume of cross-correlation. As shown in figures 15, using a 2D Gaussian-Lorentzian model results in a much larger and quicker increase of the relative cross correlation volume to the axial separation, meaning that the effective cross-correlation should fall off steeply with worse axial alignment. A separation of the two foci by 1μm results in a doubling of the

effective volume. This is explained by the significant intensity within the tails of the Lorentzian volume.
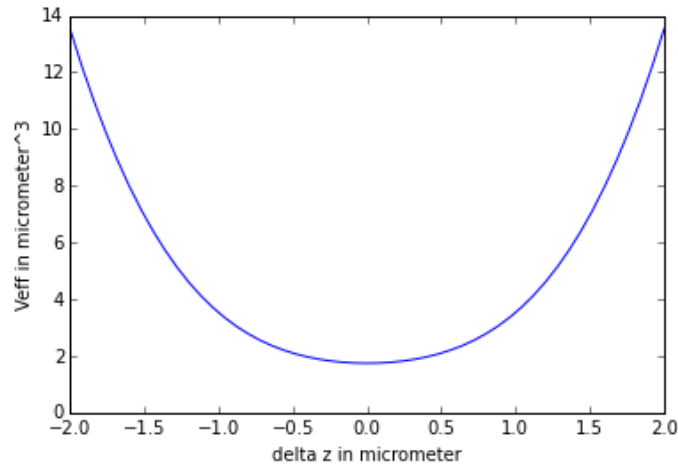
Figure 15 – Effective Volume (III-35) as a function of separation of the two focal volumes Δz using the 2D Gaussian-Lorentzian MDF model. We used the following parameters (experimental results Table 6):: $w_{0b} = 0.193\mu m$; $w_{0r} = 0.326\mu m$ $R_{0b} = 0.123\mu m$; $R_{0r} = 0.148\mu m$, $a_b = 0.522\mu m$ $a_r = 0.652\mu m$ Volume Blue $= 1.09\mu m^3$ Volume red $= 2.61\mu m^3$.

These results are in contrast to the typical FCS analysis method using a 3D Gaussian MDF (III-13), which result in a significantly flatter and less sensitive to axial separation (figure 16). In contrast to figure 15, a Δz of 4μm results in a doubling of the effective volume.
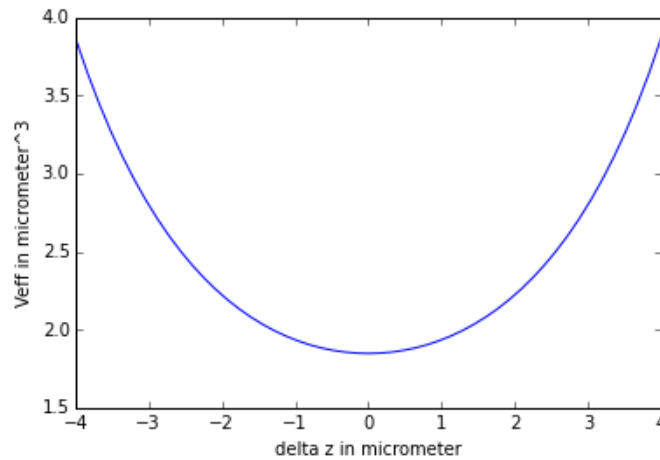
Figure 16 - Effective Volume (III-17) as a function of separation of the two focal volumes Δz using a 3D Gaussian model. We used the following parameters (experimental results Table 6): $w_{xyb} = 0.255\mu m$; $w_{xyr} = 0.370\mu m$ $w_{zb} = 3.15\mu m$; $w_{zr} = 3.43\mu m$, Volume Blue $= 1.14\mu m^3$ Volume red $= 2.61\mu m^3$.

IV. Fluorescence Cross-Correlation Spectroscopy design, construction, and characterization for single molecule detection

A. Motivation for Building a Custom FCCS

Fluorescence correlation spectrometry (FCS) is a powerful tool to measure the concentration and diffusion coefficient of fluorescent species. Originally developed in the 1970s, it saw renewed use in the past two decades following the integration of confocal optics.[76, 77] The technique has been utilized to measure not only molecular diffusion, but also binding and reaction kinetics, single molecule photo-physics, and conformational dynamics of proteins.[79, 81-83, 92, 97-100]

Fluorescence correlation spectroscopy has also been proposed as a technique to study the conformational dynamics of polymers, most notably DNA.[20, 21, 71-74] Typically, for fluorescence correlation spectroscopy measurements, a DNA molecule is single end labeled with a single fluorophore such as Rhodamine 6G or Alexa Fluor 488 using custom oligonucleotides and polymerase chain reaction.[19]

Despite it's utility, FCS in its most commonly utilized form suffers from several limitations. One of the most important is that due to physics and correlation analysis, single color FCS cannot distinguish between multiple reaction species if their diffusion coefficients' are not sufficiently separated, limiting systems of study to those with a molecular weight difference of $MW^{\frac{1}{3}}$ (e.g. a small fluorescent ligand binding to an enzyme). The second arises from the utilization of the assumption of a 3D Gaussian for the confocal volume, originally introduced in 1976 and carried on ever since.[86, 92] This model, while analytically simpler, fails to appropriately account of the optics of the system and therefore calculate an accurate confocal volume. Without an accurate representation of the confocal volume, one is not able to appropriately calibrate the system and measure objectively comparable molecules with unknown diffusion coefficients. The prevalence of this "black-box" approach translates to the use of unphysical and insensitive fitting parameters such as the structure parameter.

Two-color FCS was developed for situations where the diffusion coefficients cannot be separated in a single color approach. By introducing two channels, one measures not only the autocorrelation of the two independent colors, but also their relation between each other in the cross-correlation function. As a result, the concentration of all species can be determined independent of their diffusion coefficients, given the additional data streams. Unfortunately, two-color FCS (or FCCS) setups are technically challenging and usually expensive (e.g. Zeiss Confocor 2 or 3) on the order of $500,000.

The primary difficulty lies in the optical alignment of the two confocal volumes, their characterization, and the determination of the extent of their overlap. Typically, FCCS systems utilize two separate beam paths for excitation and emission to independently control the position of the confocal volumes.

These problems are exacerbated by the use of the 3D Gaussian fitting model. The model fails to appropriately account for the optical characteristics of the system and, as a result, a reasonable determination of the separation of the two independent confocal volumes. The axial separation of

the two volumes is crucial for accurately determining the cross-correlation volume. Without this information, one can only extract relative information between the two color channels and the cross, rather than objective, quantitative information.

In order to study polymer dynamics on a single molecule level utilizing FCS, it is critical to be able to reliably quantitatively determine and carefully characterize the confocal volume. Without proper characterization of the optics, it is impossible to effectively compare the results among multiple groups. With the previously applied 3D Gaussian analytically model, that is not possible. Additionally, the use of only a single color limits one's ability to clearly distinguish conformational dynamics given the diffraction limit.[75] A single color FCS setup also has difficulty measuring differences amongst samples of similar molecular weights.

We aim to address these issues by designing, building, and characterizing a custom two-color FCS system for the goal of establishing a reliable, quantifiable, and repeatable FCCS platform for the study of polymer dynamics.

Here we describe a simple optical design that allows us to construct a two-color FCS without the need to independently adjust both colors. We are doing this by first combining both colors into a single-mode fiber to define a fixed common origin for both colors. The point source is then expanded and focused through a color corrected objective. In order to ensure confocal volume overlap along the optical axis we underfill the objective. This also allows us to more accurately describe the intensity distribution of each confocal volume. We carefully select the optics to provide for the adjustability of the dual confocal alignment while reducing optical aberrations and maximizing alignment in the radial (x,y) directions. The confocal pinhole is defined by the optical fiber diameter. The use of multiple detectors for each single color channel serves to eliminate unwanted photo-physical and detector effects, such as after-pulsing.

The specific optical parameters of our system were integrated with a revised numerical fitting model first introduced by Dertinger et. al that can accurately determine the confocal volumes and physically account for the axial separation.[96] This concurrently eliminates some non-physical and insensitive parameters such as the structure parameter (k) from fitting as well as allows one to consistently determine the effect of a change in the optical characteristics on the fitting.

By having all of this information, one can quantitatively and consistently determine the confocal volume for both colors and the amount of overlap between the two and as a result, the concentrations and diffusion coefficients, among other parameters. This would serve as a significant improvement over commercial FCCS setups such as the Zeiss Confocor 2 and 3 that lack the ability to quantify the confocal volume without fudge parameters and therefore, effectively apply the technique to teasing out polymer dynamics.

The proposed setup also allows for the measurement of DNA under conditions more closely resembling biological conditions where DNA is in solution rather than stretched out.[45, 66] In addition, it overcomes the limitation of limited interaction distance associated with FRET. While the aforementioned technique offers information of dynamics on the order of angstroms, implementation of FCCS allows one to acquire dynamics information on the order of microns.

B. Experimental Setup – How to Build a 2 Color FCCS

We built a two color FCCS system (488nm / blue and 633nm / red) with 4 Avalanche photo diodes to perform cross-correlations on a 50:50 split for each color, as well as a cross-color correlation function. The APDs are (SPCM-AQRH-14) that have an FC fiber coupler. The correlator (Flex03lq_quad) is from correlator.com. A full schematic is illustrated below, while a comprehensive part listing is offered in **Appendix I**.
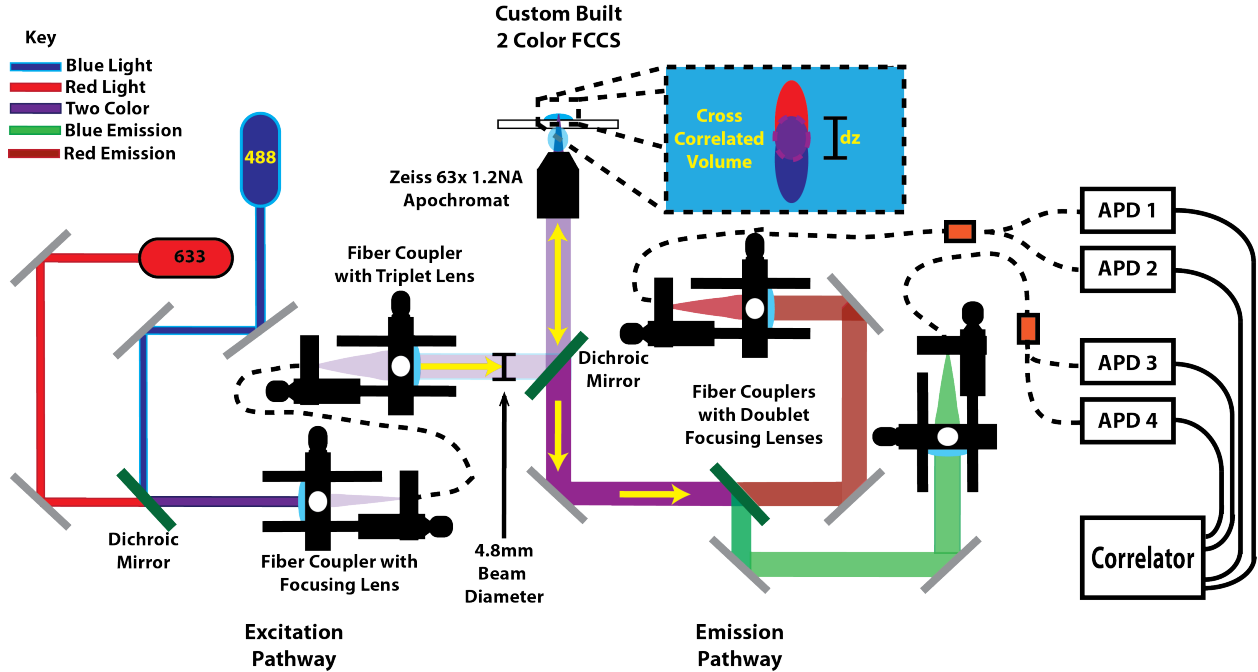
Figure 17 – Instrument Layout – Overall Schematic of Custom FCCS

The following sections will detail each section of the setup and the motivations behind the design choices.

i. Excitation Pathway

To simplify the alignment of the two colors we chose to supply both colors through one single-mode fiber (Thorlabs S405-XP 3.6+-0.5µm @ 405nm and 5.0+-0.5µm @ 630nm mode field diameter, NA = 0.12). Because the excitation light from both lasers is coupled into a single fiber, both colors of laser light come out as a point source and are aligned in the X and Y directions. Therefore, misalignment in the radial directions further upstream is eliminated.

For the blue color, we are use a Sapphire Solid State Laser from Coherent (488nm, 20mW). For the red, we use a Thorlabs HeNE laser (633nm, 5mW). It is important to choose an appropriate lens for coupling both laser beams into the S405 XP fiber. The C230 TME-A lens is coated to transmit wavelengths between $400 - 700nm$ and has a focal length of $f = 4.51mm$, the closest available to the below calculated values for both lasers.

$$f = focal\ length\ for\ fiber\ coupling = \frac{\pi D w}{4\lambda}$$

with D the $\frac{1}{e^2}$ beam diameter, w mode field diameter of fiber, λ wavelength

$$f_b = \frac{\pi(0.7mm)(4.07um \pm 0.5um)}{4 * 488nm} = 4.59mm \pm 0.56mm$$

$$f_r = \frac{\pi(0.81mm)(5.0um \pm 0.5um)}{4 * 633nm} = 5.03mm \pm 0.5mm$$

Given that the lens does not perfectly couple both colors and the blue laser has significantly more power available, it was preferred that the red laser beam was optimally coupled during alignment. Utilizing a zero-order half-wave plate attached to a polarizing beamsplitter for both laser lines controls power. Power of the laser is typically measured before entering the objective lens and was kept at approximately $30\mu W$ for each color, unless otherwise specified.

The back aperture of our objective (Zeiss C-Apochromat 63x/1.2 NA Water Corr) is 7mm. As demonstrated by Hess et. al, under filling the objective can be used to elongate and enlarge the illumination volume at the focus of the objective while simultaneously reducing the effective NA of the illumination, which helps create a 2D Gaussian-Lorentzian beam profile, more stretched out than one would expect with a 3D Gaussian.[93] The effect of this on the axial separation between the confocal volumes and the relative cross-correlation volume was highlighted in figure 15.

A triplet lens was chosen so that both colors could be collimated with the same optical element with minimal focal shift and chromatic aberrations, and would result in a Gaussian beam diameter of 4.8mm that under fills the objective by 2/3. Given the numerical aperture of the single mode fiber and the desired collimated beam diameter, the required focal length of the lens was calculated as $21.82mm$. Although not exact, the most appropriate lens was the TRH127-020-A-ML with a focal length of $20mm$.

$$f = \frac{D}{2NA_{fiber}} = \frac{4.8mm}{2(0.11)} = 21.82\ mm$$

The excitation laser light was centered on the triplet lens and collimated according to the alignment procedure in **Appendix II**, resulting in a 4.8mm Gaussian beam entering the objective lens.

The triplet lens has a modest focal shift between the $488nm$ and $633nm$ wavelengths (figure 18) and results in the majority of the axial separation that is expected. The expected maximum axial (z) shift (Δz) resulting from the triplet lens is calculated as:

$$\frac{f_{triplet}}{Shift_{triplet}} = \frac{f_{obj}}{Shift_{obj}} \rightarrow \frac{20.0mm}{0.01mm} = \frac{2.61mm}{x} \rightarrow \mathbf{1.305um}\ \text{max expected z shift}$$

where the focal length of the objective length was calculated as follows,

$$\frac{tube\ length}{M} = \frac{164.5mm}{63} = 2.61mm = f_{obj}$$
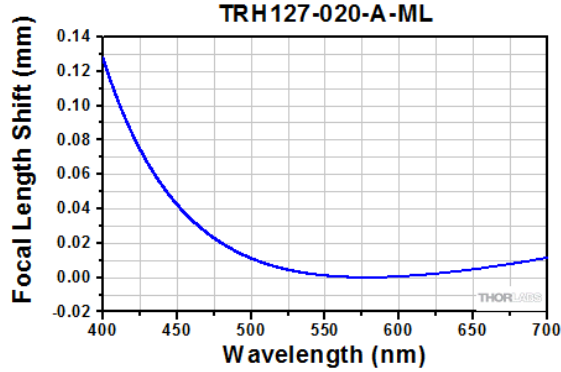
Figure 18 – Focal Shift of TRH127-020-A-ML lens

Because the objective lens is underfilled, the effective NA of the system on the excitation side is

$$NA_{eff} = NA_{obj}\frac{4.8}{7.0} = 0.823$$

ii. Emission pathway

Following excitation of the sample, the fluorescent light is re-collimated by the Zeiss objective and transmitted through the dichroic beamsplitter. A second 580nm single edge dichroic mirror separates the emission pathway into two lines, one for each color. The emitted light has an effective NA of 1.2.

Each color is coupled to another fiber launch system so that the collimated fluorescent light can be focused onto a multimode fiber, which serves as the effective pinhole. Two multimode fiber diameters were used in the following experiments, $25\mu m$ and $50\mu m$ (#4 figure 19). The collimated emission light is centered onto the pinhole in the fiber coupler through the adjustment of the X/Y alignment stage (#1 figure 19).

The signal is evenly split into two detectors using a 50/50 1x2 multimode fiber splitter (Thorlabs). Each color is auto-correlated with itself to eliminate any detector effects such as those resulting from after-pulsing.

The emission fiber coupler is illustrated in further detail in Figure 19.
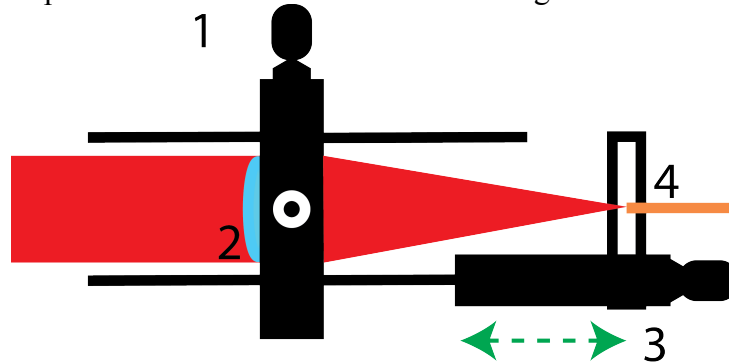
Figure 19 – Emission pathway Fiber Coupler. 1) X/Y lens adjusters 2) Achromatic Doublet Lens 3) Axial (Z) adjuster 4) Multimode fiber

The fiber coupler in the emission pathway relies on achromatic doublet lenses (#2 figure 19). The choice of focal length for the blue and red pathways was made so that the spot size of the two colors onto the multimode fiber pinhole would be similar (table 1). To verify the appropriate lens for the emission pathway focusing of the beam, one can determine the appropriate parameters from the following relation,

$$\theta = \frac{2\lambda}{\pi\omega_0} \approx \frac{D}{f}$$

where θ is the beam half angle, ω_0 the radius of the spot size. The beam angle can be approximated by the relation of the incoming beam size ω_0, aperture D, and the focal length of the lens, f. With the parts listed in **Appendix II**, the setup has the following parameters:

Table 1 – Expected Effective Size of Focused Light on Pinhole

Wavelength (nm)	488 nm	633nm
Airy Disk Diameter (um)	31.01	32.18
Gaussian waist size $\frac{1}{e^2}$ (um)	16.18	16.79
Gaussian FWHM (um)	13.75	14.27

A z translation stage (#3 figure 19) provides for the adjustability of the distance between the pinhole and the doublet lens, allowing for maximum control of the z positioning of the spot size.

One can calculate what the effective sizes of the different fibers would be. For example, our objective has a magnification of 63x calculated for the standard tube length of 164.5mm. In our setup, for the 488nm channel, we are using a 125mm lens focusing on either a 25µm or 50µm pinhole. A 25µm pinhole reduces to a 0.261µm aperture in the object plane. The calculation is performed as shown,

$$a = \frac{r_{fiber}}{M} * \left(\frac{t_l}{f_{em-lens}}\right)$$

where r_{fiber} is the radius of pinhole fiber, M the magnification, t_l the tube length, and $f_{em-lens}$ the focal length of the emission lens.

Table 2 – Determination of Confocal Aperture a

λ (nm)	Focal length (mm)	Fiber Diameter (um)	a (um)
488	125	25 / 50	0.261 / 0.522
633	100	25 / 50	0.326 / 0.652

In summary, several modifications are incorporated together to result in a novel and more robust implementation of FCCS design. First, the two laser colors are aligned and couple together within a single single-mode optical fiber improving radial alignment later on within the system. Second, the two colors are collimated and focused with an achromatic triplet lens that minimizes chromatic aberrations that contribute to axial separation of the confocal volumes as well as allowing us to underfill the main objective back aperture, therefore allowing for a clear characterization of the confocal volumes. Third, a multimode fiber is utilized as a confocal pinhole. Fourth, four detectors are utilized, with two dedicated to each color. Coupled with a 1x2 multimode fiber splitter, detector effects are removed by correlating each color with two

detectors. Further photo-physical effects such as triplets are removed by correlating the average correlation from each color with each other.

C. Methods – Alignment and Calibration of the FCCS

i. Dye Selection

The dyes of choice were Atto 488 and Atto 633 (Atto TEC Gmbh). They were chosen because of their relative photo-stability, insensitivity to large differences in pH, and spectral separation between them. Relevant fluorophore diffusion coefficients are located in **Appendix III.** Chosen dyes had precisely measured diffusion coefficients verified by multiple experimental groups with multiple techniques. The diffusion coefficients were adjusted according to the temperature dependence as shown in **Appendix IV.**

The choice of dyes is critically important for proper FCS calibration measurements. For example, Alexa / Atto 647 dyes show peculiar effects on the ACF in timescales less than 10^{-4} seconds independent of laser excitation energy, which greatly affect the fitting and determination of the confocal volume and amplitude of the ACF.[101]

ii. Alignment of FCCS

Proper utilization of the FCCS platform requires careful calibration and alignment of both color channels to ensure maximum overlap of both laser volumes, critical for consistent two color measurements. A step-by-step alignment protocol is located in **Appendix II**.

Once the optics are properly aligned, this only guarantees alignment in the radial directions, X and Y, and not axial alignment. While the wavelength and the focal length of the emission pathway fiber coupler lens provide an approximate idea of what point along the axial direction (Z-axis) the image of the confocal volume is focused, it is necessary to verify the correct positioning of the multimode fiber for each color.

The easiest and most effective way to determine the correct z position of the pinhole is to perform a series of measurements along the axial direction of the pinhole. The pinhole is started at an initial position and shifted a fixed distance outward from the lens. This process is repeated at least three times for each calibration, in the same direction, prior to the acquisition of a new set of experimental measurements. At each new step in z, the X/Y translator is adjusted for maximum intensity followed by a 90 second measurement of the auto-correlation function at that position using a standard solution of a dye with known diffusion parameters.

Typical calibration parameters are as follows: ~1.5nM solutions of both Alexa 488 (Invitrogen) and Atto 633 (Atto-TEC Gmbh) within a buffer of DI water mixed with 0.05% by volume of Tween-20, $30\mu W$ of excitation power before the objective for both colors. A couple limitations of this method include the precision of the axial stage (#3 figure 19) and the precision of the X/Y translator at finding the optimum value.

Basic fitting of the acquired ACFs in each color is performed in order to extract the amplitude of

the ACF at $G(0) = \frac{1}{N}$ and the width at half maximum, which corresponds to an approximation of the diffusion time (τ_D). Relative minimums for both N and τ_D are found, corresponding to proper positioning of the pinhole at the minimum spot size.[96] All subsequent calibration and experimental measurements are performed at the established minimum position, which can vary with any realignment or adjustment of the excitation or emission optics described previously.
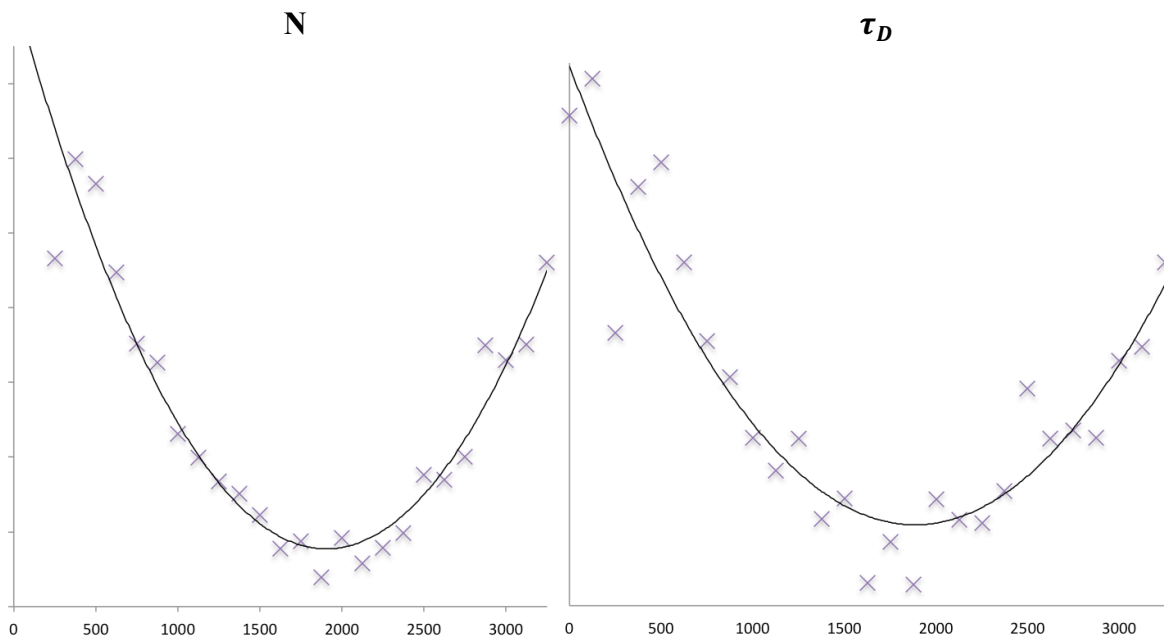
Figure 20 – Example Z-positioning data for N (left) and τ_D (right). X-axis axial (z) position of the micrometer

iii.   Dye Standard calibration

Each dye solution (atto 488 or 633) was prepared from a stock solution of 100uM, which was aliquoted at 1uM concentrations and subsequently frozen in DI water. The stock solution concentrations were verified using a UV-VIS spectrophotometer. The absorbance of a serial dilution ranging across several orders of magnitude and the extinction coefficient report for each dye is used to determine the actual, experimental concentration. This step is critical, as more often than not, the exact weighed amount of dye does not correspond to the label. Coupled with pipetting errors (highlighted in **Appendix V**), the concentration can be significantly over- or under-estimated in stock, and therefore negatively affect calibration measurements. Expected concentrations were found to differ from actual concentrations by a range of factors from ~0.5x to 1.5x depending on the dye or the particular stock.

For all measurements stock was diluted in a buffer of either 1x Tris-EDTA mixed with 0.5% w/v Tween 20 detergent to avoid any aggregates. This is extremely important when dealing with free dyes as any charged dye such as these Atto dyes are prone to aggregation.

Aliquots used in the following FCCS calibration measurements have their estimated concentration multiplied by the factors 1.482 ± 0.089 and 0.762 ± 0.037 for AT488 and AT633, respectively, in order to obtain the true experimental concentration. The dilution series is

a serial dilution done by a factor of two. A typical concentration dilution series for calibration measurements is,

$$12.5nM, 6.25nM, 3.125nM, 1.5625nM$$

Power is kept at $25 \pm 0.5\mu W$, as measured before entering the objective lens, as it provides the best balance between count rate and avoiding optical saturation effects, which become prevalent above $\sim 90\mu W$.[87, 91]

iv. FCCS Calibration Standard – Oligonucleotide

For FCCS standard, we use a 40bp custom designed ds-oligonucleotide. The standard is comprised of two complementary single strand oligos labeled at the 5' end with either Atto 488 or Atto 633. The two single strands are annealed together at equimolar concentration in an annealing buffer (10 mM Tris, pH 7.5–8.0, 50 mM NaCl, 1 mM EDTA).[102] The mixture is heated to 95°C for five minutes and then cooled to room temperature.

The size of the oligo standard was chosen specifically given that at 40bp (~13.6nm length) both ends of the same molecule will always be present in the confocal volume at the same time.

v. Data Capture

Data is captured with a 4-channel correlator (Correlator.com Flex03LQ-01 Digital Correlator).

For free dye measurements, each dilution concentration is measured for at least 20 repeats per color. Each ACF repeat measurement was captured over a time of at least 120 seconds and run under identical optical alignment configuration. The correlator is arranged as shown in table 3 / figure 21. The two ACFs for each color are averaged together. The average ACF from each repeat measurement is then averaged together, resulting in one final ACF per color per concentration along with standard deviations at each time point. This scheme eliminates most noise due to uncorrelated photo-physical effects or detector effects.

Table 3 – Dye Dilution Series Correlator Measurement Scheme

Correlator Ch	Channel 1	Channel 2	Channel 3	Channel 4
ACF	Blue 1	Blue 2	Red 1	Red 2
APD	1 x 2	2 x 1	3 x 4	4 x 3
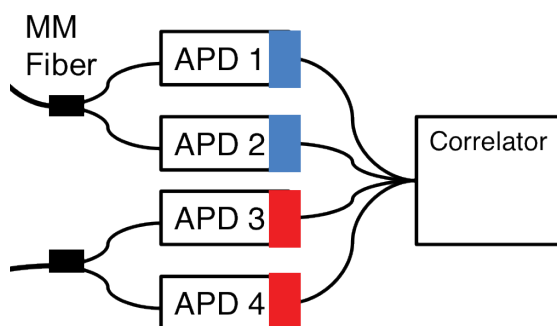
Figure 21 – APD Setup by Color

For FCCS oligo standard measurements the correlator is set up as follows. Similar to the dye measurements, 20 repeats are performed for a measurement time of 180 seconds. The measurement scheme for the oligo captured two ACFs (one for each color) and two cross-correlation functions (overlap between colors) as illustrated in table 4. Cross 1 and Cross 2 are averaged, and all 20 repeats are averaged to obtain a global Blue ACF, Red ACF, and a CCF (cross-correlation function). All three curves are fit simultaneously.

Table 4 – FCCS Standard Correlator Measurement Scheme

Correlator Ch	Channel 1	Channel 2	Channel 3	Channel 4
ACF/CCF	**Blue**	**Red**	**Cross 1**	**Cross 2**
APD	**1 x 2**	**3 x 4**	**1 x 4**	**2 x 3**

vi.   Data Fitting

We aim to address data fitting limitations of previous FCS studies resulting from the use of a 3D Gaussian model by adapting a numerical fitting method that characterizes the confocal volume as a 2D Gaussian – Lorentzian in order to more closely relate the fitting parameters to the physical optical parameters of the aforementioned FCCS system.

Further theoretical elaboration and derivation is provided in **Chapter III**.

A critical point of emphasis for a FCCS system is the importance of not only knowing the confocal volume of each color, but also precisely determining the axial separation between the two volumes (figure 22). As mentioned in the previously, alignment within X/Y directions is accomplished through the optical alignment, while Z cannot be similarly adjusted because of factors such as the focal shift of the triplet lens and optical characteristics of the Zeiss objective. This greatly affects the calibration in that provides information regarding the maximum level of cross correlation possible for the system, without which it is impossible to extract quantitative information for more complex molecules, such as longer DNA molecules.
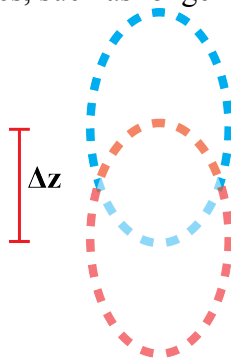
Figure 22 – Axial separation between two color confocal volumes and respective overlap. Δz is defined as the distance between the center of both color volumes.

For comparison, we implement both the traditional analytical 3D Gaussian fitting method, as described theoretically in **Chapter III** and first published by Rigler et. al.[78] and the numerical

2D Gaussian – Lorentzian (Gaussian Beam) fitting method as first described by Enderlein et. al.[87] All fitting is performed in python using multiple packages, which primarily include, but are not limited to, numpy and lmfit. Numpy is a collection of array and mathematical functions while lmfit offers a parameter based method for performing non-linear least squares fitting. More information regarding these fitting packages can be found in the following references and will not be further elaborated on in this document.[103, 104]

The averaged autocorrelation datasets (for free dyes) were fit in the following order: first, the ACFs for freely diffusing fluorophores of known concentration were fitted with known D(diffusion coefficients) and concentrations. Both Gaussian and Numerical / Gaussian Beam (Gaussian-Lorentzian) fits were performed to extract the radial w_{xy} and axial w_z waists for the former and radial waist and w_{xy} and aperture R_0. After an initial fit, the datasets were run in a global fit to refine the previously fitted parameters.

For fitting, the fixed, known diffusion coefficient of the dye was adjusted based on the temperature at the time of experimental ACF capture (see **Appendix IV**). The concentrations were also fixed within a tight range as defined by the errors mentioned in the previous section.

Utilizing the parameters obtained above, the FCCS double labeled oligonucleotide is measured and it's two ACF's and cross correlation function (CCF) are fit together to obtain a diffusion coeeficient D, concentration C, and confocal volume separation distance, in microns Δz.

D. Results

Multiple complete sets of dilution series and oligonucleotide standard measurements were completed; however, for simplicity and brevity, a representative sample set is presented here. Because subtle changes in the alignment occur between each data set and are prone to various errors, not all data sets result in identical fitting parameters describing the waist and confocal volume. Despite this, we are successfully able to reliably and consistently extract a diffusion coefficient and concentration for two-end labeled calibration oligonucleotide in agreement with theory.

i. Calibration Dyes

The following sets of ACFs show the fitting of a fluorophore dye at a concentration of 3.125nM for both blue and red channels. Fitting was performed with Gaussian and Numerical fitting methods utilizing a global fit over a dilution series. The fitted parameters are presented in table 5/6. The summarized fits can be seen in figures 23 and 24 for the $25\mu m$ and $50\,\mu m$ pinholes. Both channels seem to fit similarly, regardless of pinhole; however, the numerical method appropriately fits an larger or smaller aperture R_0 dependent on the pinhole size. Another important point lies in the fact that the red confocal volume waist increases from the $25\,\mu m$ to $50\,\mu m$ pinhole. This indicates, as was shown earlier, that part of the confocal volume is being cut off in the X/Y directions. This carries through and relates to the quality of the fits of the oligo.

Table 5 – Fitting parameters for Free Dyes – 25 um Pinhole

Method	Parameter	Blue (μm)	Red (μm)
Gaussian	w_{xy}	0.236 ± 0.004	0.313 ± 0.008
	w_z	2.76 ± 0.02	2.51 ± 0.03
Numerical	w_{xy}	0.193 ± 0.004	0.291 ± 0.004
	R_0	0.207 ± 0.001	0.206 ± 0.001

Table 6 – Fitting parameters for Free Dyes – 50 um Pinhole

Method	Parameter	Blue (μm)	Red (μm)
Gaussian	w_{xy}	0.255 ± 0.003	0.369 ± 0.008
	w_z	3.15 ± 0.03	3.43 ± 0.03
Numerical	w_{xy}	0.193 ± 0.004	0.326 ± 0.003
	R_0	0.123 ± 0.003	0.147 ± 0.005
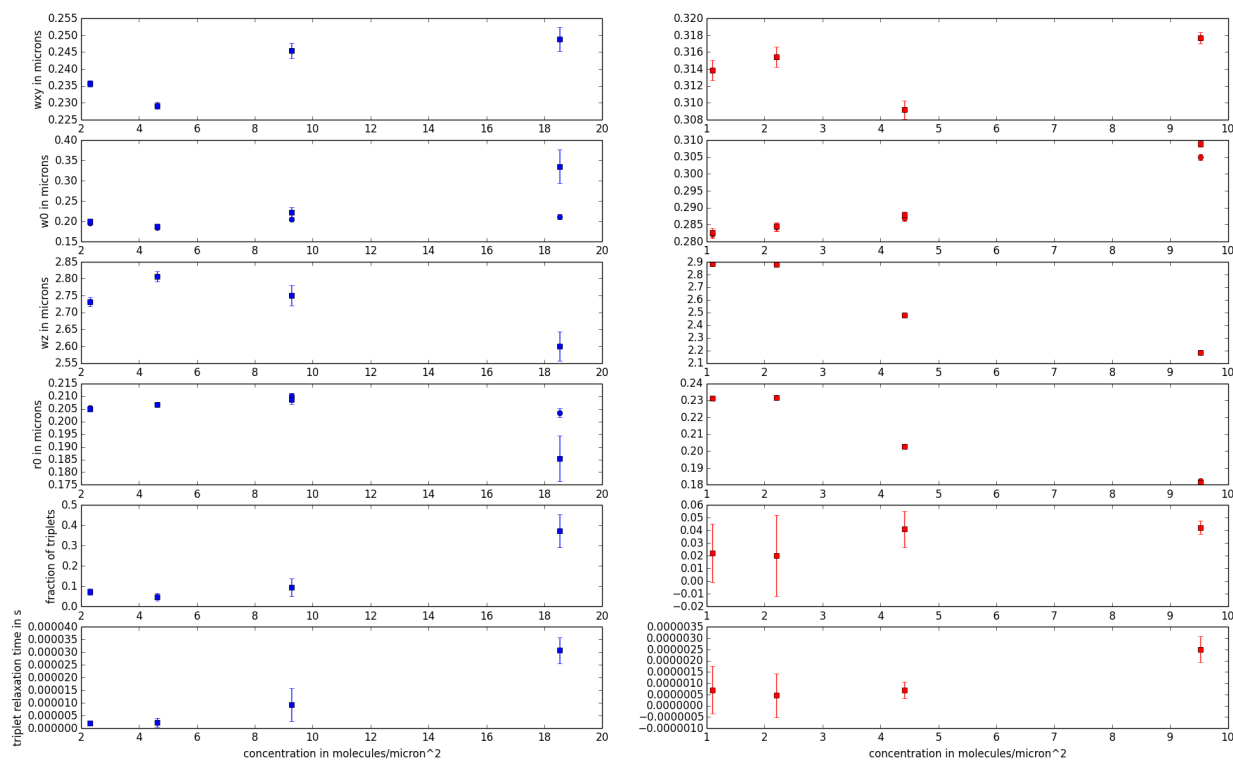
Figure 23 – Fitting parameters for dye, Gaussian and Numerical, 25 um Pinhole
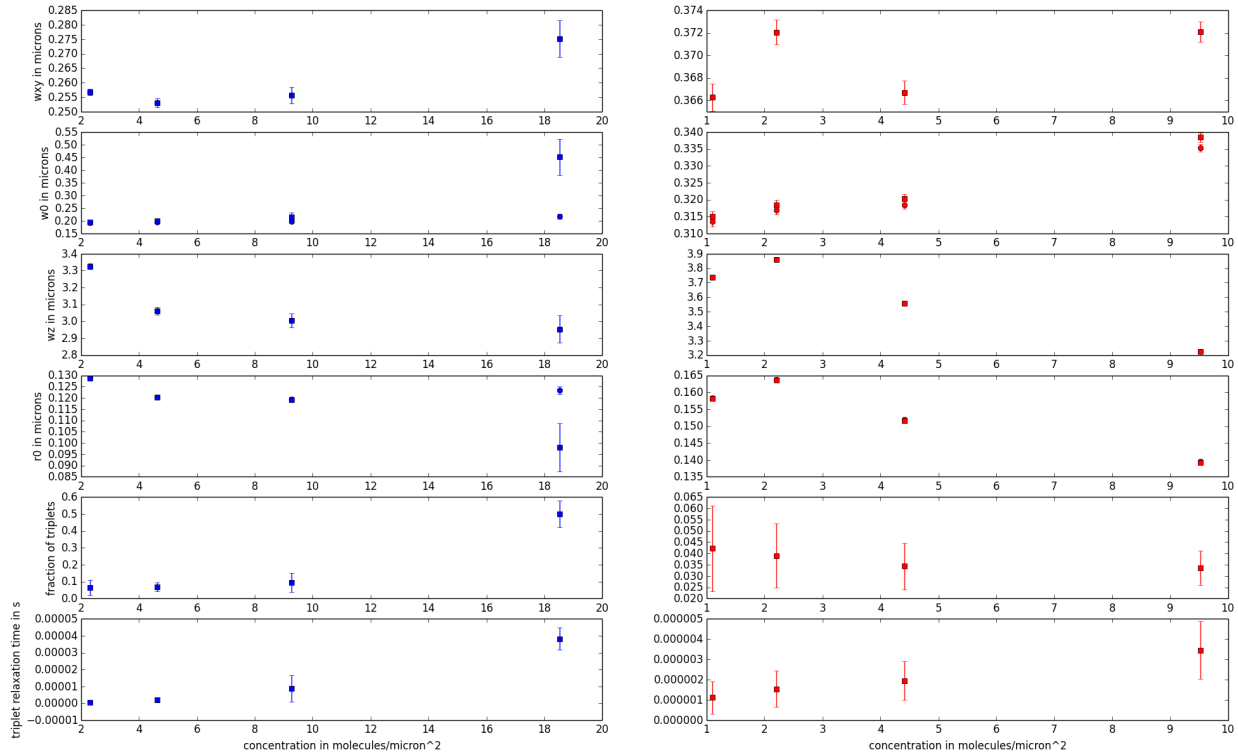
Figure 24 – Fitting parameters for free dye, Gaussian and Numerical, 50 um Pinhole

Figures 25, 26, 27, and 28 highlight individual fits obtained for a particular dilution concentration. Both the Gaussian and Numerical fits produce similar fit qualities, as can be seen by analyzing the residuals ($data - fitted\ line$), although it could be argued that the numerical fitting produces marginally better fits. In all the figures, a residual within ±1 indicates that the fitted line is within ±1 standard deviation, as calculated from ACF averaging. Given these results, it might seem unnecessary to utilize a more complicated and timely fitting method for fitting FCS curves; however, in terms of fitting parameters, only the numerical method is able to account for and adjust physical parameters accordingly related to the changing pinhole sizes. The Gaussian method results in different structure parameters and waist in both the radial and axial directions for both channels, whereas the numerical method sees only a change in the red channel, as expected from theoretical expectations of the optical system. Additionally, both fits show minimal improvement with the inclusion of a triplet fraction and triplet time parameters, indicating minimal influence of triplets. This is expected given the choice of dyes (Atto 488 / 633).
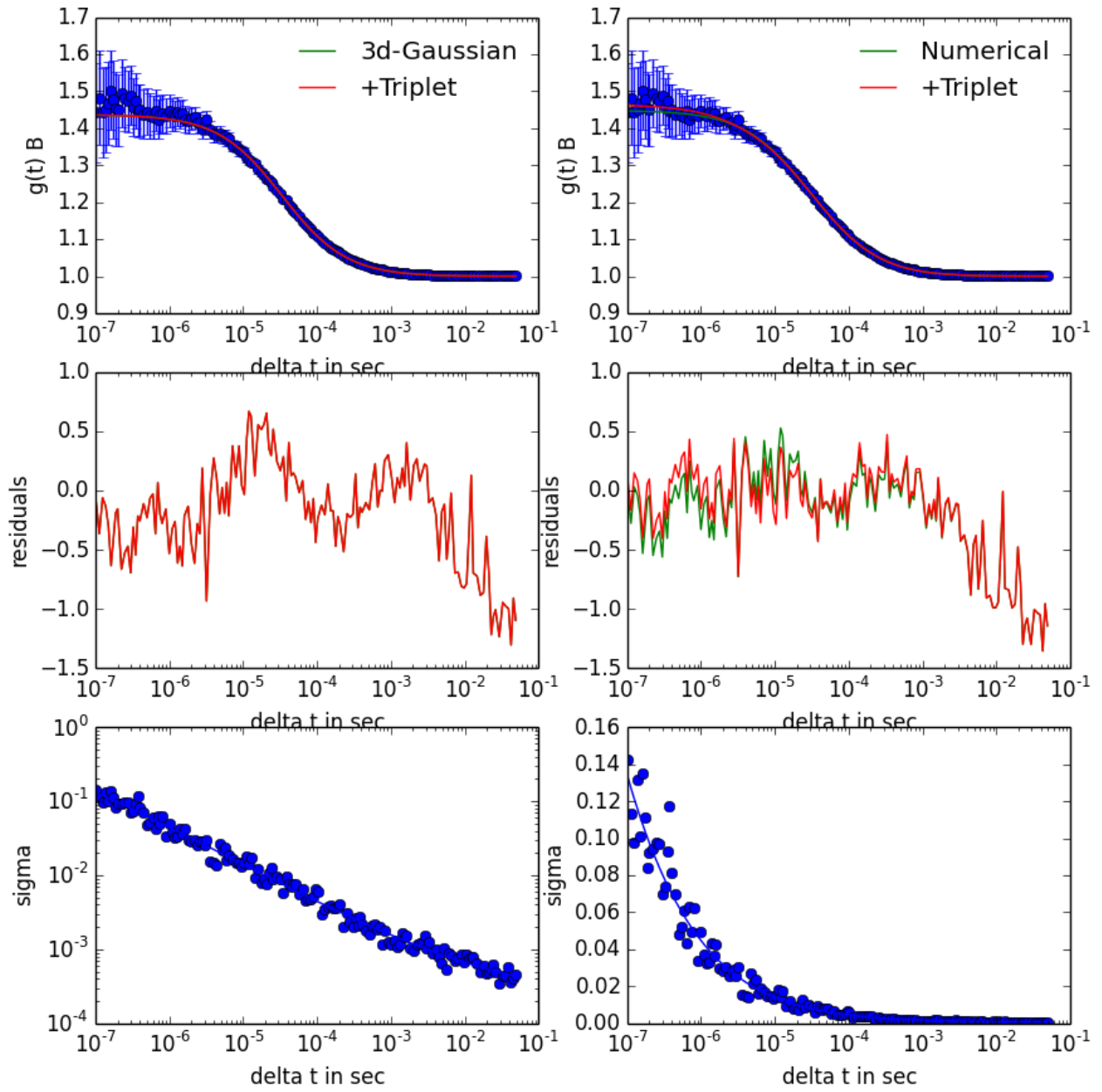
Figure 25 – Gaussian (left) and Numerical (right) fits for **Atto 488**, **25um pinhole**
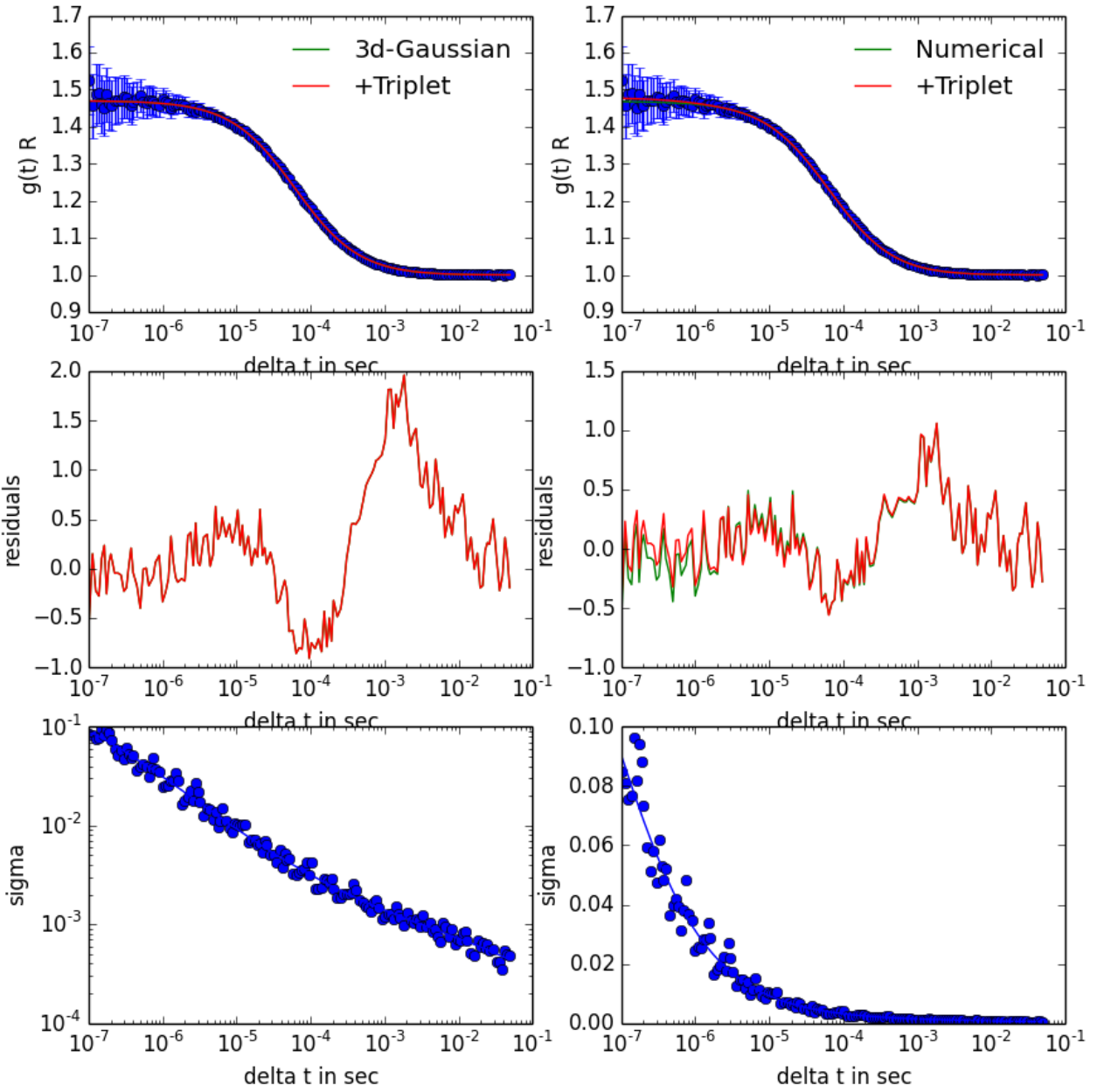
Figure 26 - Gaussian (left) and Numerical (right) fits for **Atto 633**, **25um pinhole**
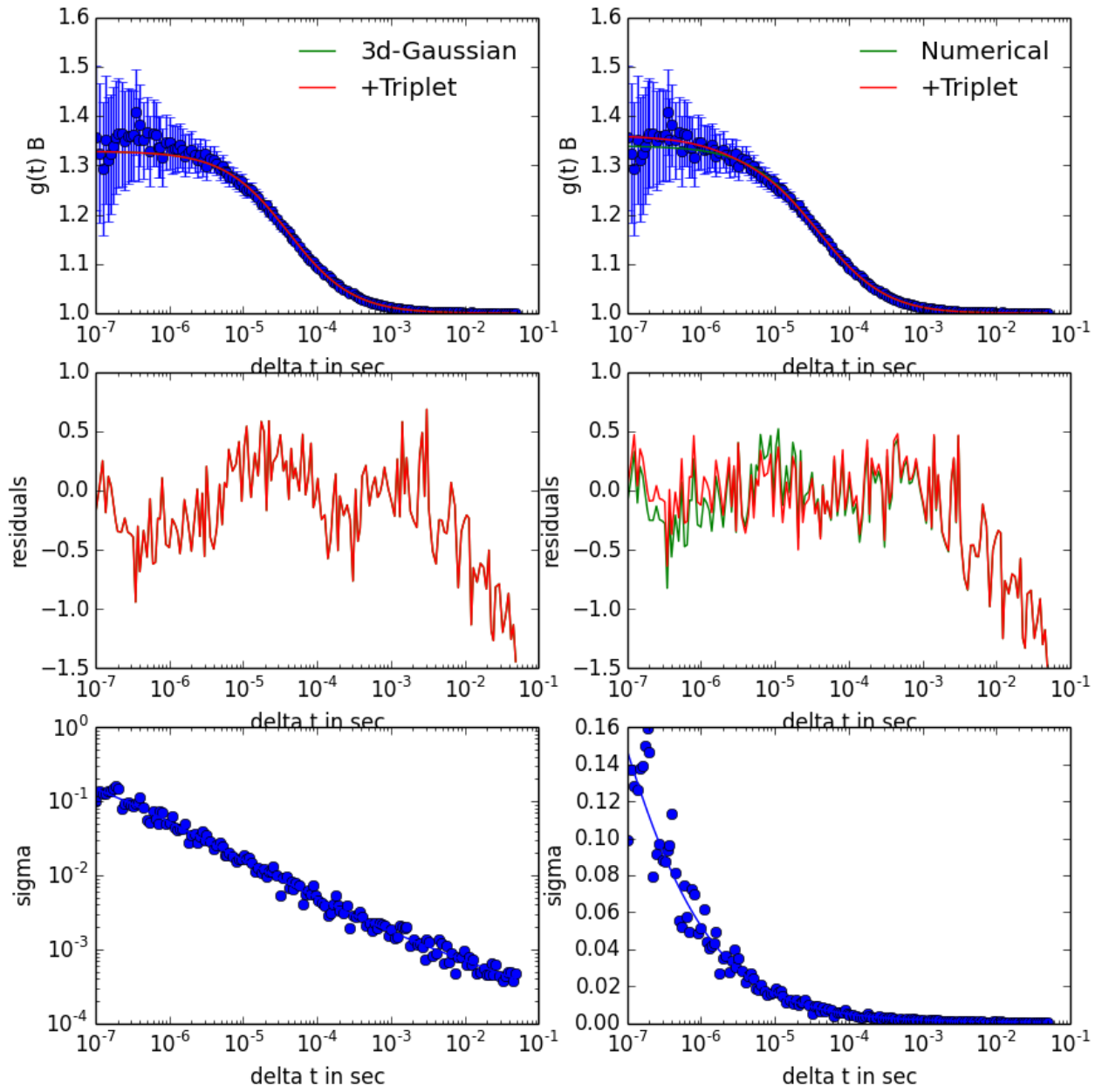
Figure 27 – Gaussian (left) and Numerical (right) fits for **Atto 488**, **50um pinhole**
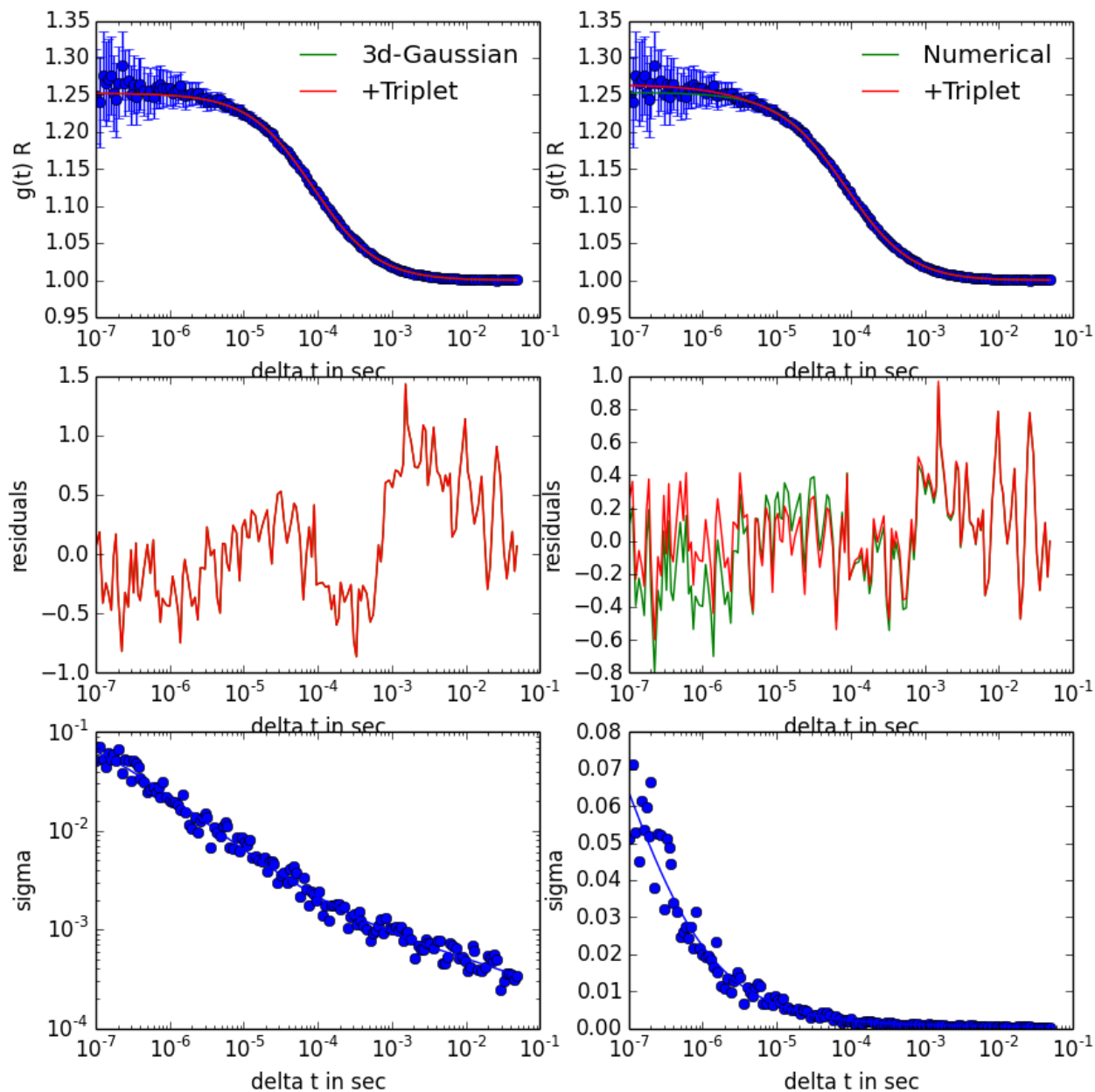
Figure 28 – Gaussian (left) and Numerical (right) fits for **Atto 633**, **50um pinhole**

ii. Double Labeled Short Oligos for Calibration

Theoretical curves were plotted for the numerical fitting method to show the effect of changing diffusion coefficients and confocal volume seperation distances on the shape and position of the ACF and CCF. The illustrated curves utilize the same fitted parameters obtained with the numerical fitting of the calibration dyes with a 50um pinhole. Increasing D (slower molecule) shifted both the ACFs and CCF to longer timescales (figure 29). The diffusion coefficient was plotted over a range of 55 to 87 um^2/s. The Δz had a range of 0.5um to 1.5um. Increasing seperation distance reduced the amplitude of the CCF (figure 30).
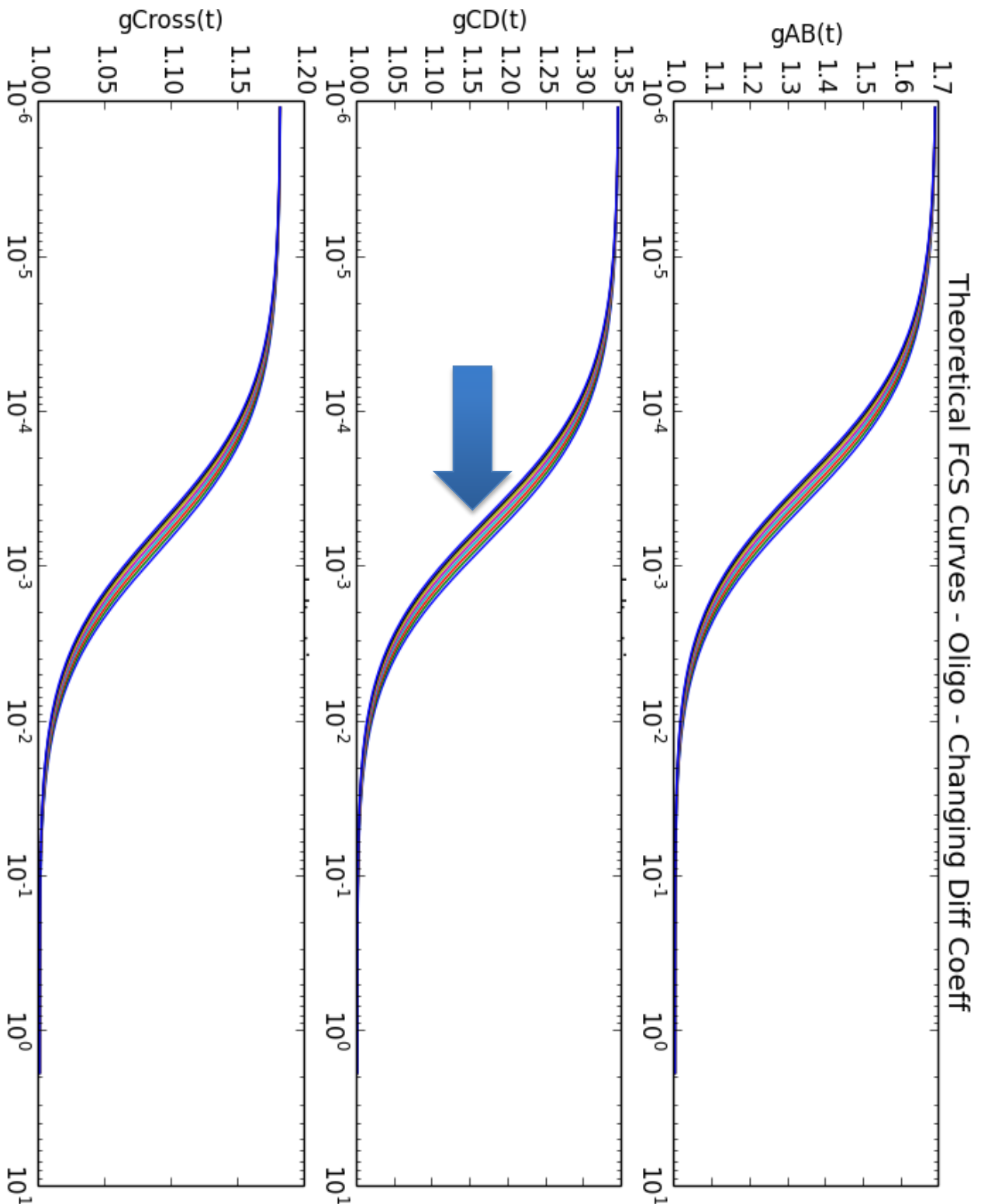
Figure 29 – Theoretical Numerical Fitting Curves for changing Diffusion Coefficients (arrow indicates direction of slower diffusion, smaller diffusion coefficients)
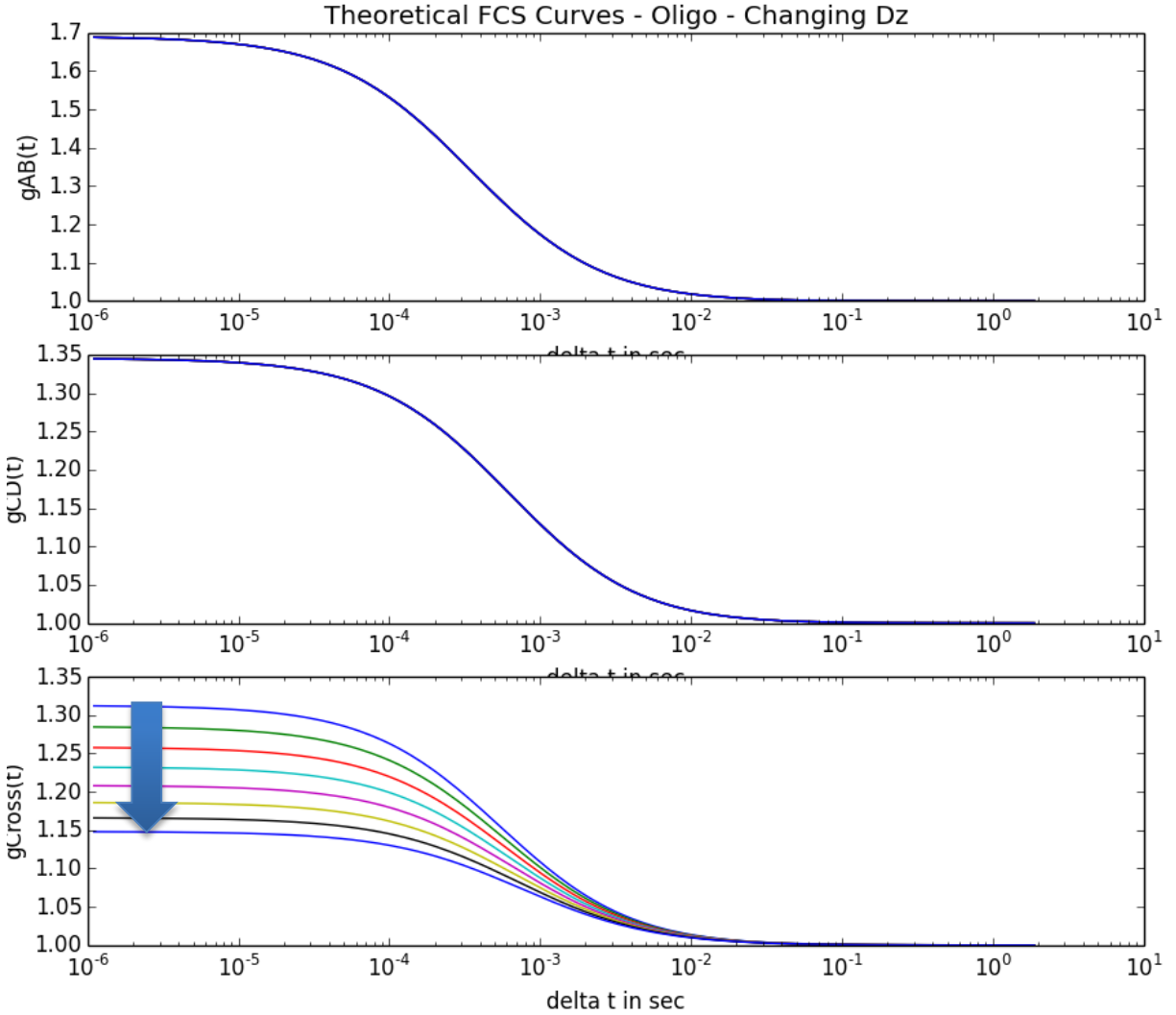
Figure 30 – Theoretical Numerical Fitting Curves for changing Axial Separation Δz. Downward arrow indicates increasing axial separation.

Given that the persistence length of ds-DNA is 50nm, this short oligo can be assumed to be a rigid rod.[46] With $t = 2nm$, $L = 40bp * .34nm$, the theoretical diffusion coefficient of the standard is,

$$D_G = \frac{(D_\| + 2D_\perp)}{3} = \frac{ln\left(\frac{L}{t}\right)k_B T}{3\pi\eta_w L} \rightarrow D_{ol\ go} = 69.2\frac{\mu m^2}{s}$$

Experimental curves were fitted with both the Gaussian and numerical fitting methods for both pinholes were performed with the FCCS double-labeled oligo standard as detailed above as shown in figures 31, 32, 33, and 34. What can quickly be discerned is the robustness of the numerical method for not only being able to fit both pinholes more accurately, but to do so over the entire range of the time scales for all three curves simultaneously. While the Gaussian method was able to fit similar values for the diffusion coefficient, it was not able to properly account for the axial separation nor fit all three curves with a global fit without significant over-

and under-fitting.

The numerical method was the only one that was able to not only account for the different pinhole methods, but able to match the theoretical diffusion coefficient and concentration within 5% and the result in a fit not only in line with the expected axial separation as demanded by the optics, but also within 12%.

Ideally, it would be worthwhile to validate the axial separation through additional experimental tests; however, at the time of this study, the tools required to do so were unavilable. Given the smallness of the separtation, one would require well below sub-micron precision axial movement such as the kind offered by a piezo-electric automated stage (ideally $> 0.1\mu m$). One could then utilize a system of fixed red and blue dye, such as free dye within a fixed size nano channel to scan axially to see where a minimum in the amplitude of the autocorrelation curve occurs for both channels. The minimum would correspond with a maximum in the concentration and volume.

The results are summarized below:

Expected $D = 69.2 \ \mu m^2/s, C = 2.0 \pm 0.1 \ nM, \Delta z = 1.305 \ \mu m$

Numerical Results

25 μm $\quad D = 72.7 \pm 0.8 \ \mu m^2/s, C = 1.98 \pm 0.01 \ nM, \Delta z = 1.13 \pm 0.01 \ \mu m.$

50 μm $D = 70.87 \pm 0.4 \ \mu m^2/s, C = 2.09 \pm 0.01 \ nM, \Delta z = 1.17 \pm 0.006 \ \mu m.$

Gaussian Results

25 μm $D = 69.5 \pm 0.9 \ \mu m^2/s, C = 1.92 \pm 0.01 \ nM, \Delta z = 4.13 \pm 0.03 \ \mu m.$

50 μm $D = 67.8 \pm 0.7 \ \mu m^2/s, C = 2.11 \pm 0.02 \ nM, \Delta z = 4.57 \pm 0.05 \ \mu m.$

Other groups have also looked at the axial separation of the confocal volumes, but have focused their efforts on explaining this within the 3D Gaussian model by introducing fudge factors. This is untenable if one were to try to study more complex molecular species to extract quantitative information, which relies on a quantitative description of the confocal volume. Other groups arbitrarily select the pinhole that results in the "best" fit, rather than quantifying what effect it may have on the values produced by the fit.

Due to imperfect optics the best ratio of $\frac{G_{BR}(0)}{G_R(0)}$ is ~0.5 for the 50μm pinhole and about ~0.3 for the 25μm pinhole. As has been shown by others, even small misalignments in either the excitation or emission pathways is sufficient to significantly reduce the ratio [105]. The same misalignment was observed on a commercial Zeiss Confocor 3 [105]. Importantly, and counter to results reported by other groups, the ratio of $\frac{G_B(0)}{G_R(0)} > 1$. This confirms the expected result that the volume for the red channel should be larger than that for the blue and therefore, more red molecules should be observed.
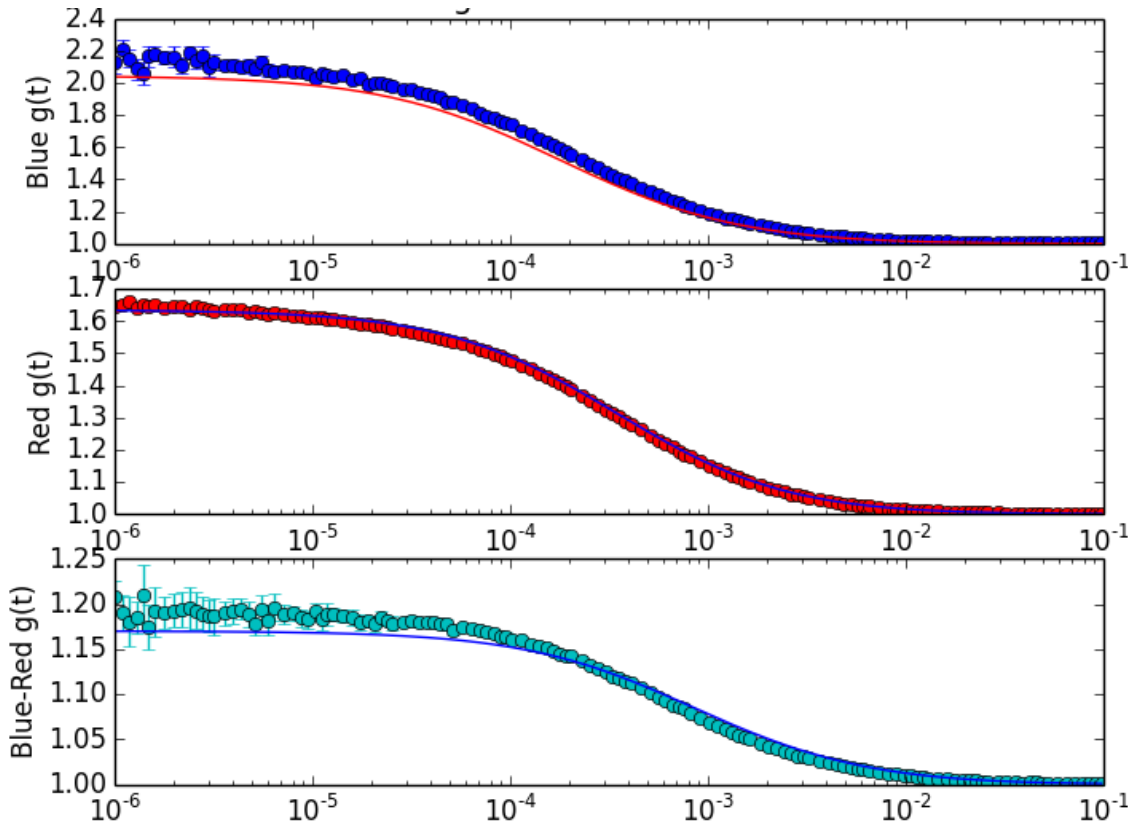
Figure 31 – Numerical Fit of Oligo – 25um Pinhole
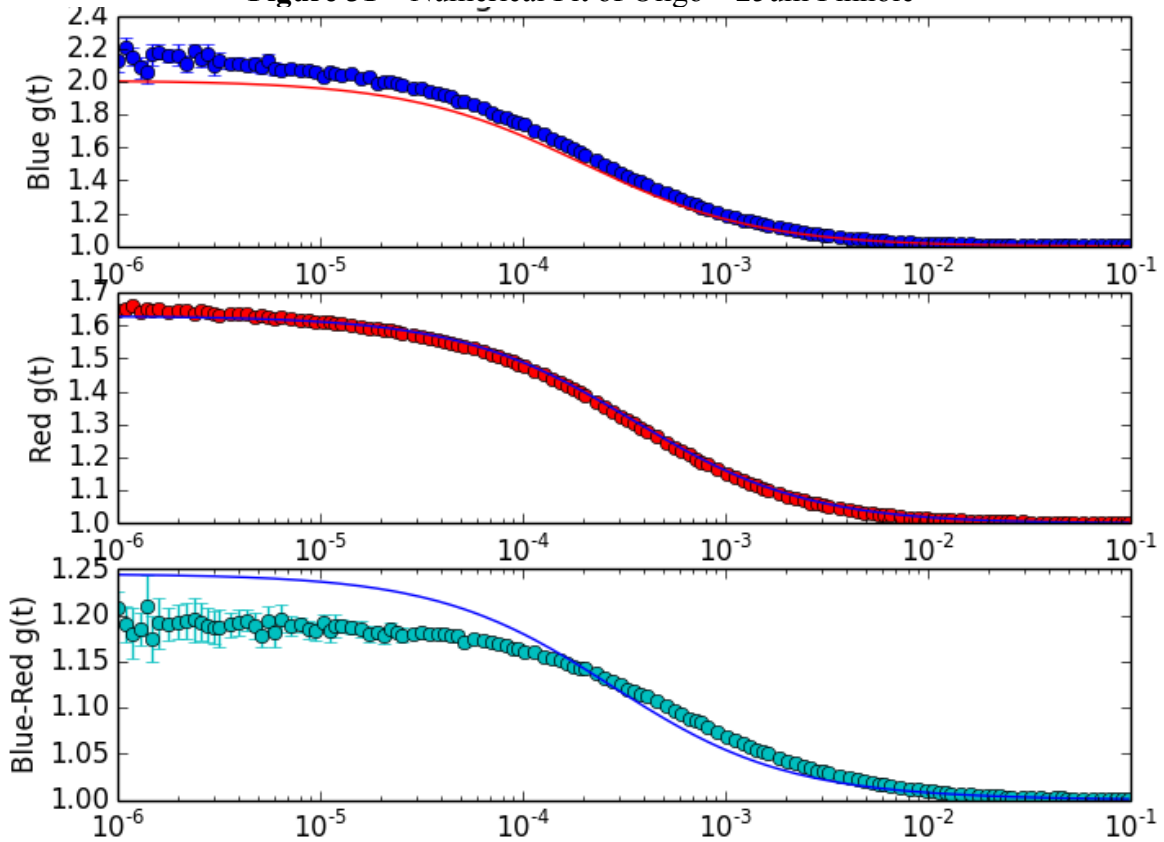
Figure 32 – Gaussian Fit of Oligo – 25um Pinhole
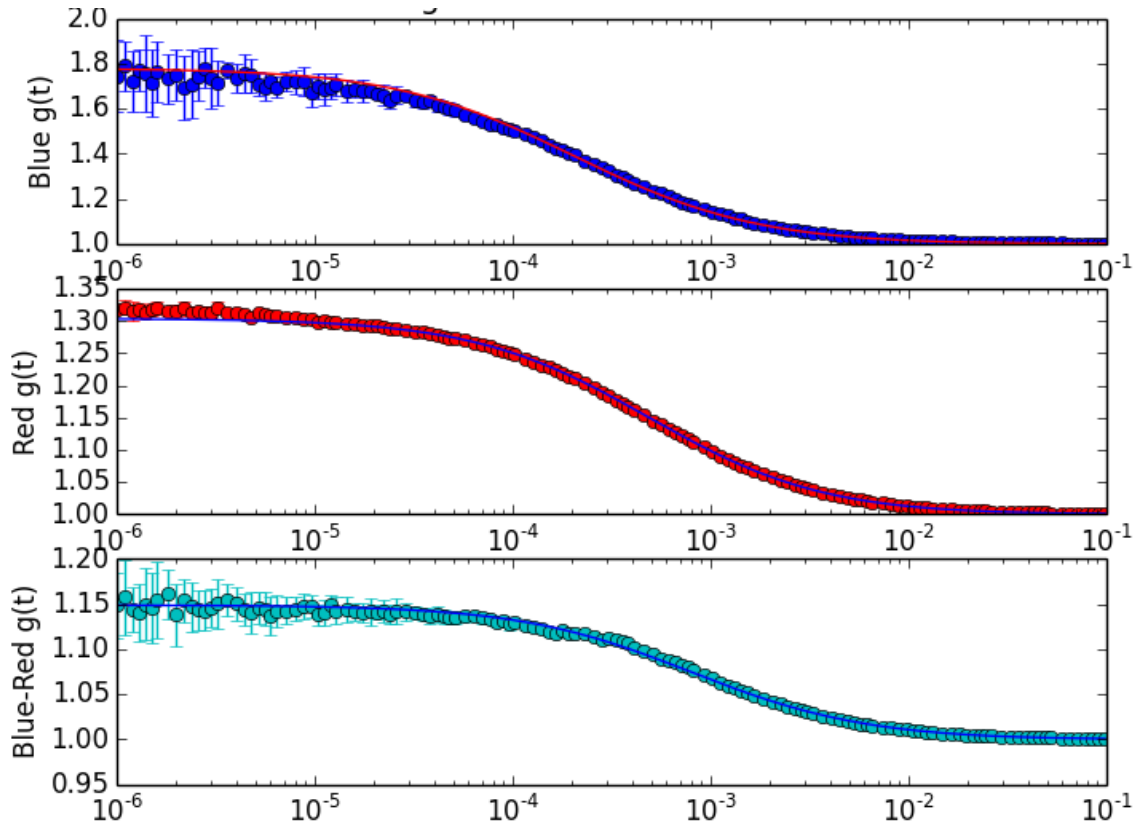
Figure 33 – Numerical Fit of Oligo – 50um Pinhole
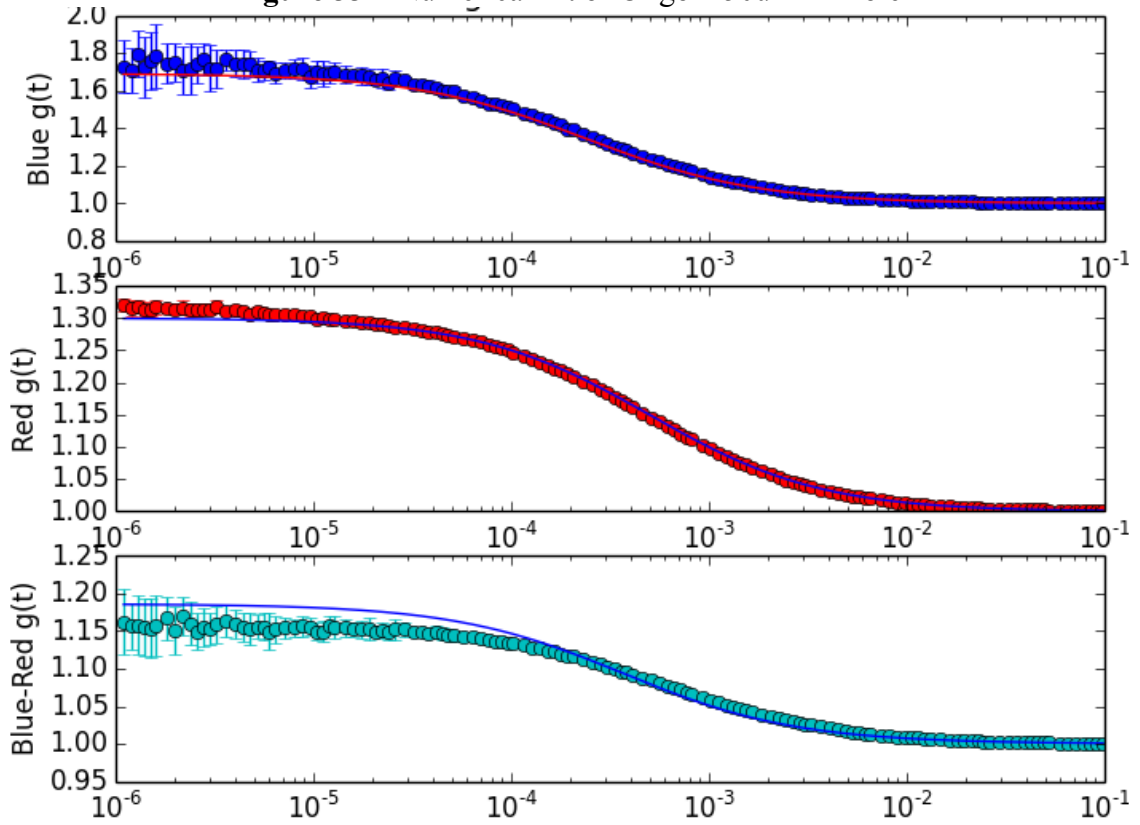
Figure 34 – Gaussian Fit of Oligo – 50um Pinhole

45

Additional tests of the FCCS setup and its functionality were done by performing a titration study of FCCS standard. This was done to determine the sensitivity of the FCCS setup and the efficiency of the double labeling. Double labeled oligo was mixed with fixed ratios of single labeled samples, as shown in figure 35. Fits were performed by removing the restriction on a global concentration and fitting three independent concentrations (one for each color channel and one for the cross-correlation), totaling three. As a test, the axial separation parameter was both fixed and allowed to vary to determine the sensitivity of the numerical fit and if it would be able to provide a reasonable fit.
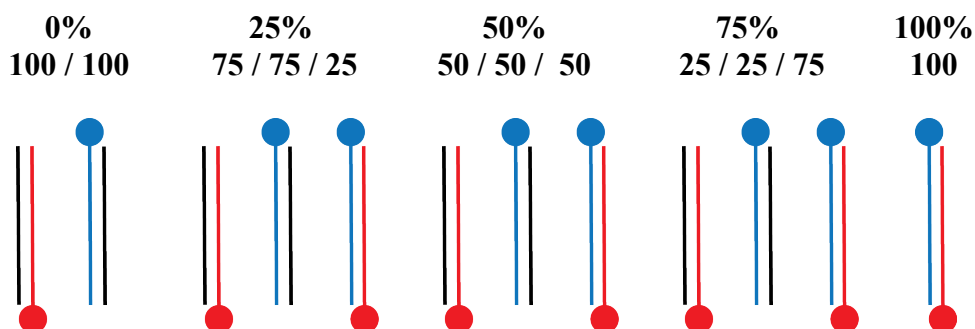
Figure 35 - Percentage Ratios of Single label and double label oligonucleotides for each mixture

Counter-intuitively, the cross-correlation function *decreases* in amplitude as less double-labeled oligos are present and more single-labeled oligos replace them. Typically, one expects the amplitude of a correlation function to increase when the concentration of a species drops; however, the effect on the cross-correlation curve is the opposite. This effect has been seen by multiple other groups and can be summarized as follows, [81, 106, 107]

$$\frac{C_{BR}}{(C_B + C_{BR})(C_R + C_{BR})} * \frac{1}{V_{eff}} \propto \frac{p}{C}$$

where p is the ratio of the concentration of double label to single label species. Therefore, when the amount of double labeled species, e.g. double-labeled oligo, is mixed with a varying concentration of single labeled oligos, the amount by which the amplitude of the cross-correlation function drops can be account for through the factor p.

An alternative method of describing the relation of single and double-labeled species where C_{DL} is the concentration of a 100 percent double-labeled oligo solution is as follows:

$$C_{BR} = pC$$
$$C_B = (1 - p)C$$
$$C_R = (1 - p)C$$
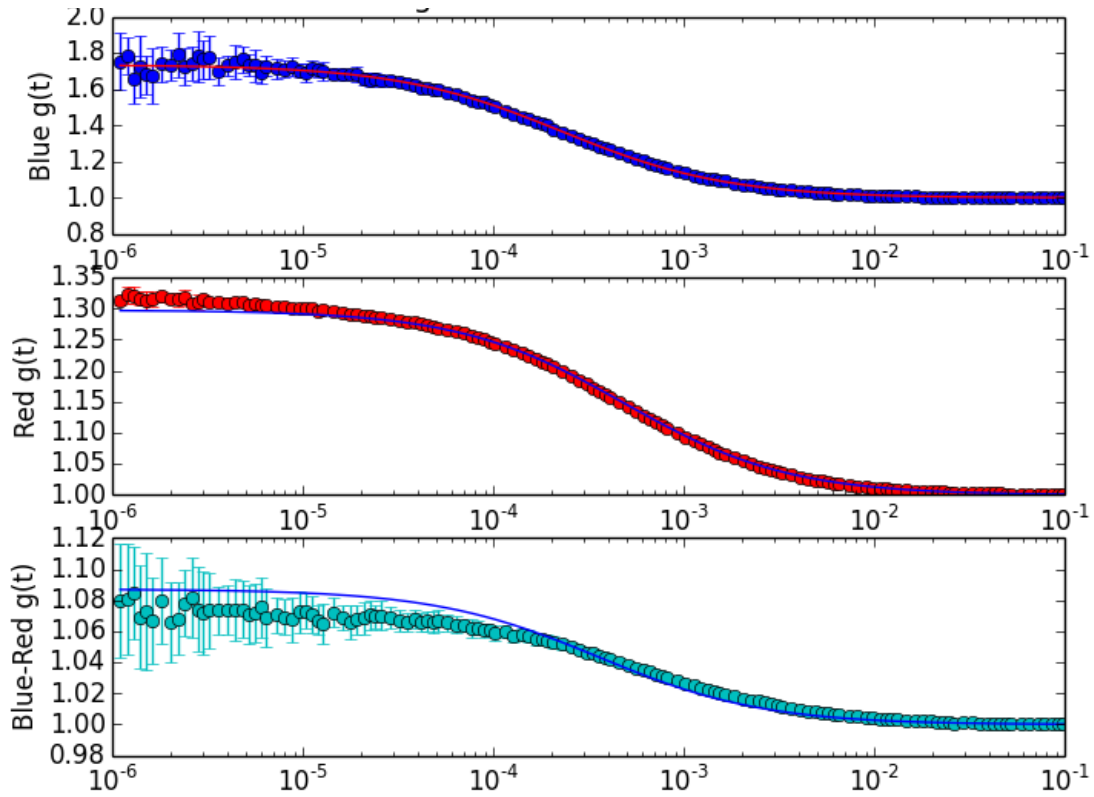
Figure 36 – Gaussian Fit 50% Single Label / Double Label Mix
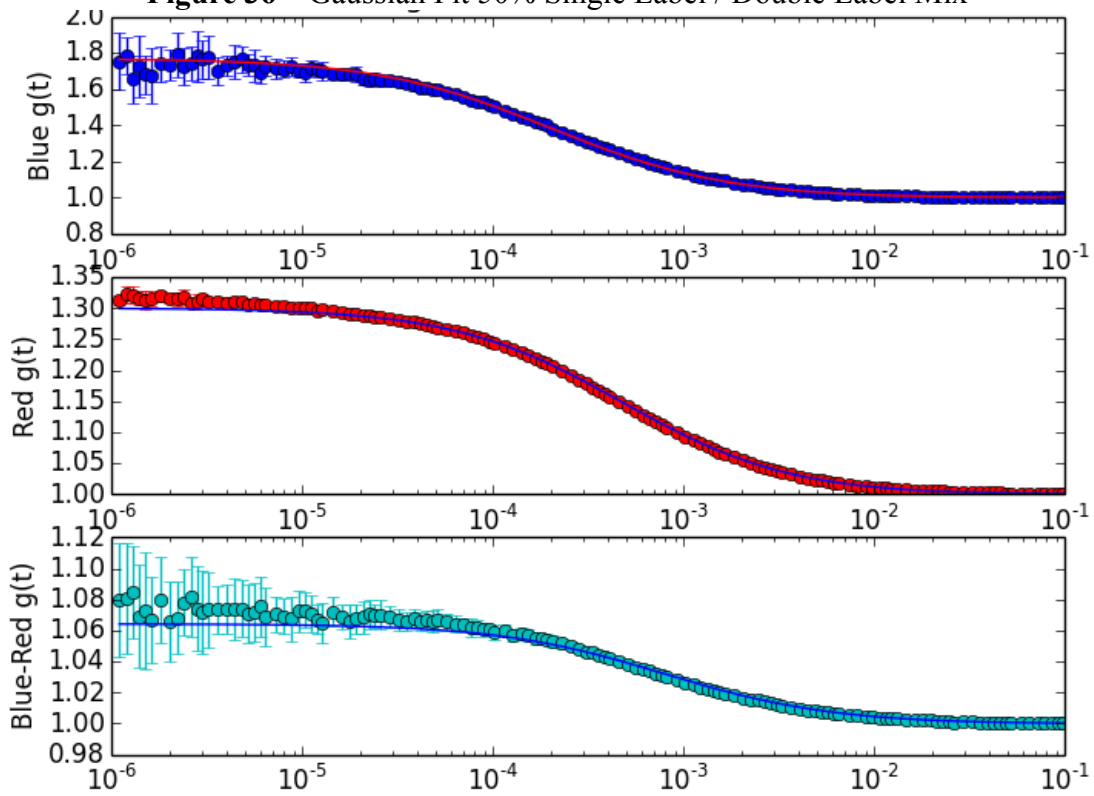
Figure 37 – Numerical Fit 50% Single Label / Double Label Mix
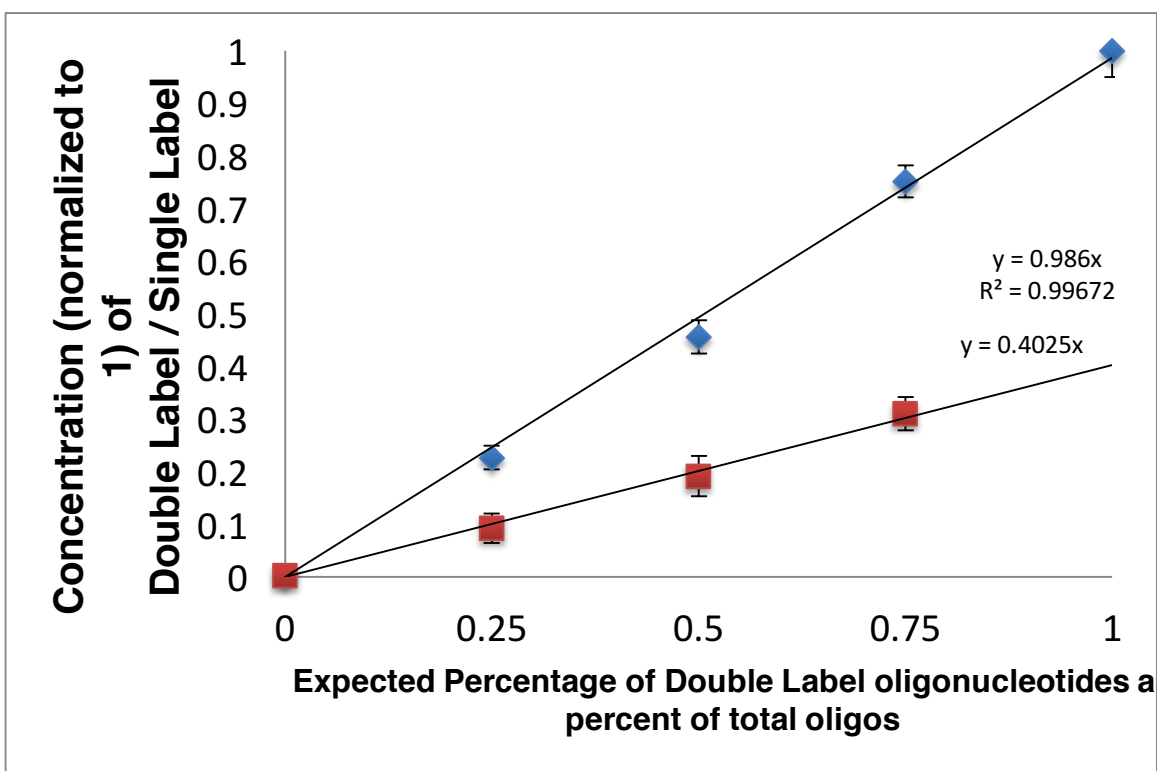
Figure 38 – Experimental measurement of double label oligonucleotide concentration. Blue numerical fit, Red Gaussian fit

The results are shown in Figure 36, 37, and 38. The fits once again are much stronger when performed numerically. The Gaussian fits result in significant over- and under- fitting in a global fit. Previous studies that have performed similar titrations only compared the amplitude $G(0)$ rather than performing a fit.[106, 107] Therefore, they only compared relative concentrations, rather than verifying concrete, quantitative values. Only the numerical fit (blue diamonds) results in realistic, quantifiable concentrations (figure 38). While the Gaussian fit is also able to show a linear relationship, it cannot provide quantitative values, only relative ones. The reliance on 3D Gaussian model prevents one from incorporating any optical characteristics of the system and therefore impossible to objectively compare two sets of results captured and fit on two independent FCS apparatuses. Without a careful understanding of the optics and an arbitrary selection of the pinhole, the results from FCS result in fits that look "good", but that cannot be translated to meaningful physical information about the system under study.

E. Conclusion

Fluorescence Correlation Spectroscopy can be a powerful experimental technique; however, its previous experimental application has been lacking. Many previous studies focused on a "black box" approach to FCS by failing to properly describe the optics of the system and, therefore, failing to properly describe the size and shape of the confocal volume. Previous studies have also overwhelmingly focused on a 3D Gaussian approach to data fitting. These approaches and assumptions break down when attempting to extract reliable, quantitative information when shifting to a two-color system.

We sought to address these limitations and others by outlining in this paper how one would design, build, and characterize a two-color Fluorescence Cross-Correlation Spectroscopy setup for a fraction of the cost of a typical commercial FCCS setup. We carefully selected the optics and added control and precision to the alignment, calibration, and measurement with the system. We implemented an improved numerical fitting model based on a 2D Gaussian-Lorentzian confocal volume shape that more accurately reflects the true physics of the system by incorporating the optical parameters of the hardware within the model. We also were able to account for the drop in the cross-correlation curve amplitude relative to the auto-correlation curve through describing the optics of the FCCS system.

Utilizing this approach we showed clearly how one can quantitatively and consistently determine the confocal volume of two colors as well as the specific overlap between them. We hope that this approach to FCCS design will serve as a clear guide for anyone who hopes to build their own FCCS system as well as offer a platform for reliable quantitative measurement of more complicated single molecule systems such as the measurement of double-labeled DNA.

V. Characterizing DNA Dynamics in Solution with FCCS

As has already been highlighted, developments in single-molecule experimental techniques in recent years have opened up the possibility for studying the detailed dynamics of double-stranded DNA in solution. Previous results by other groups have focused on single end-labeled molecules, limiting their experimental utility.[19, 20] These initial results have spurred multiple studies regarding whether Rouse or Zimm dynamics are evidenced in solution, with significant theoretical work and experimental studies applying FCS to polymer dynamics.[21, 73, 74, 108, 109] The controversy in the literature extends beyond whether what dynamics are displayed and whether FCS is able to elucidate polymer dynamics at all given the limits of diffraction limit.[75, 110]

It remains questionable whether single color FCS can be applied to the study of polymer dynamics. With two colors, resulting in triple the amount of information (2 ACFs and CCF), and avoiding the incorrect assumptions of a Gaussian fitting model, we aim to get past the limitations of these previous studies with our FCCS design. Furthermore, confinement, as attempted in **Chapter VI**, would further slow the dynamics and stretch out the molecules.

We aim to apply our custom FCCS design to determine the diffusion coefficients, relaxation modes, and mean squared displacements (MSD) of a wide range of double-end labeled polymers in solution. Several methods are tested to try and tease out the polymer dynamics. Numerical fitting methods (**Chapter III**) are expanded upon to incorporate theories of polymer dynamics. Additionally, a novel approach focused on extracted the MSD from the auto- and cross-correlation functions. Polymer scaling exponents are compared to traditional theories of polymer dynamics.

A. Theory of Polymer Dynamics

The primary information we hope to probe directly with our setup includes the first order relaxation time, the diffusion coefficient, and the MSD. For polymers in free solution, $D \sim 1/R_g$.[46] Thus, knowing information about the Diffusion allows one to determine the radius of gyration of the polymer directly if the appropriate theory is employed. As derived for the Zimm model in a good solvent the relaxation time τ_r and diffusion of center of mass D_G of a polymer are as follows (for Zimm $\nu \cong 0.588$):

$$\tau_p = \frac{\zeta_p}{k_p} \quad \tau_p = \frac{\tau_1}{p^{3\nu}} \tag{V-1}$$

$$\tau_1 = \tau_r = \frac{\zeta_1}{k_1} \cong \frac{\eta_s \bar{R}^3}{k_b T} = 0.325 \frac{\eta_s N^{3\nu} b^3}{k_b T} \tag{V-2}$$

$$R_g \cong \bar{R} * numerical\ factor = \frac{1}{\sqrt{6}} * N^\nu b \tag{V-3}$$

$$\tau_r = 4.777 \frac{\eta_s}{k_b T} R_g^3 \tag{V-4}$$

$$D_G \cong \frac{k_b T}{\eta_s N^\nu b} \cong \frac{k_b T}{\eta_s R_g} = 0.196 \frac{k_b T}{\eta_s \bar{R}} = 0.2030 \frac{k_b T}{\sqrt{6}\eta_s R_g} \ (good\ solvent) \tag{V-5}$$

Calculation of D_G with renormalization group theory was first done by Oono et al. with the limit in good solvent as written in V-5.[111]The MSD can be thought of as the spatial extent of the

random motion or diffusion of the polymer or, more simply, how much space has been explored by a "random walker." Typically for a simple system, such a free dye, the $MSD = 2Dt$ for a single dimension. This is incorporated in the fitting of the ACF or CCF; however for complex molecules such as semi-flexible or flexible polymers, this theory must be modified to incorporate polymer dynamics.

Figure 39 - Schematic of Fluorescence Correlation experiments on end-labeled polymers. (left) Pure diffusion; (middle) Single end-label; (right) Double two-color end-labels.

We derived an appropriate polymer theory for a single end label and double-end label, a schematic of which is shown in figure 39. The pure diffusion model with the simplest MSD was used in the fitting of both free dye and the oligonucleotide. The single end-label case of the derivation is used in the fitting of the ACF of a long polymer, while the double-end label case is needed to fit the CCF. The theory follows:

We define normal coordinated in the following way:

$$\vec{X}_p = \frac{1}{N}\int_0^N dn\cos\left(\frac{p\pi n}{N}\right)\vec{R}_n(t) \tag{V-6}$$

with the inverse transform

$$\vec{R}_n = \vec{X}_0 + 2\sum_{p=1}^{\infty}\vec{X}_p\cos\left(\frac{p\pi n}{N}\right) \tag{V-7}$$

The solution has the following form

$$\left\langle\left(X_{0\alpha}(t)-X_{0\alpha}(0)\right)\left(X_{0\beta}(t)-X_{0\beta}(0)\right)\right\rangle = \delta_{\alpha\beta}2D_G t \tag{V-8}$$

and

$$\left\langle X_{p\alpha}(t)X_{q\beta}(0)\right\rangle = \delta_{pq}\delta_{\alpha\beta}\frac{k_B T}{k_p}\exp(-t/t_p) \tag{V-9}$$

We are interested in two special cases:
1) Single end-label

$$\left\langle\left(\vec{R}_0(t)-\vec{R}_0(0)\right)^2\right\rangle = \left\langle\left(\left(\vec{X}_0(t)-\vec{X}_0(0)\right)+2\sum_{p=1}^{\infty}\vec{X}_p(t)-2\sum_{p=1}^{\infty}\vec{X}_p(0)\right)^2\right\rangle \tag{V-10}$$

for each component i=x,y,z the result is

$$\left\langle\left(\vec{R}_{0i}(t)-\vec{R}_{0i}(0)\right)^2\right\rangle = 2D_G t + 8\sum_{p=1}^{\infty}\frac{k_B T}{k_p}\left(1-\exp(-t/t_p)\right) \tag{V-11}$$

in this case, for t=0 the mean square displacement is zero.

2) Two end labels

$$\left\langle \left(\vec{R}_0(t) - \vec{R}_N(0) \right)^2 \right\rangle = \left\langle \left(\left(\vec{X}_0(t) - \vec{X}_0(0) \right) + 2\sum_{p=1}^{\infty} \vec{X}_p(t) - 2\sum_{p=1}^{\infty} (-1)^p \vec{X}_p(0) \right)^2 \right\rangle \quad \text{(V-12)}$$

for each component i=x,y,z the result is

$$\left\langle \left(\vec{R}_{0i}(t) - \vec{R}_{Ni}(0) \right)^2 \right\rangle = 2D_G t + 8\sum_{p=1}^{\infty} \frac{k_B T}{k_p} \left(1 - (-1)^p \exp(-t/t_p) \right) \quad \text{(V-13)}$$

For the special case where **t=0** the mean square displacement simplifies to

$$\left\langle \left(\vec{R}_{0i}(0) - \vec{R}_{Ni}(0) \right)^2 \right\rangle = 16\sum_{p=1}^{\infty} \frac{k_B T}{k_{2p}} \quad \text{(V-14)}$$

where for the Zimm model in good solvent we have,

$$k_p = \frac{6\pi^2 k_B T}{(N^\nu b)^2} p^{2\nu+1} \quad \text{(V-15)}$$

which, when using the following result,

$$\sum_{p=1}^{\infty} \frac{1}{(2p)^{2.2}} = 0.32437849411162745 \quad \text{(V-16)}$$

results in a mean square displacement of

$$\langle \left(\vec{R}_{0i}(0) - \vec{R}_{Ni}(0) \right)^2 \rangle = \frac{13}{15\pi^2} (N^\nu b)^2 \approx 0.0878(N^\nu b)^2 = G(0) \quad \text{(V-17)}$$

Thus, one can relate the amplitude of the CCF to the radius of gyration of the polymer after normalizing against the maximum CCF possible, as determined in **Chapter IV** using the oligo.

In order to appropriately fit polymers using the numerical methods outlined in **Chapter IV**, the fitting function must be modified to incorporate the multiple relaxation modes evident in the previously summarized theory. This is done by replacing the normal MSD within the ACF or CCF with the appropriate form as derived above.

$$2Dt \rightarrow 2Dt + a = 2Dt + 8\sum_{p=1}^{\infty} \frac{k_b T}{k_p} \left(1 - e^{-\frac{t}{t_p}} \right) \quad \text{(V-18)}$$

Plugging in k_p and t_p, where $\nu = 0.588$ (Zimm) results in,

$$2Dt + 8\sum_{p=1}^{\infty} \frac{R_g^2}{\pi^2 (p^{2.176})} \left(1 - e^{-\frac{t}{\tau_1}} \right) \quad \text{(V-19)}$$

For numerical fitting, the summation of p is performed over a limited range from 1 to 20, as the value of k_p at 20 is less than 1% of the value at $p = 1$, which is a sufficient approximation. To reduce fitting parameters, one can replace radius of gyration dependence with an equivalent form in terms of diffusion coefficient.

B. Theoretical Fits of Polymers Utilizing Numerical Methods

Theoretical FCS curves were calculated for the full range of molecular weights (500bp to 6kbp) incorporating the previously derived theory for single and double end labeled situations. The values used for diffusion coefficient, relaxation time, and radius of gyration utilized for each case are provided in their respective tables. The first set is based off of theoretical values calculated using the Zimm model in good solvent (table 7 / figure 40). The Radius of gyration was calculated from **V-3**. The relaxation time t_1 was calculated from **V-2**. For all calculations herein, we utilized a η_S(dynamic viscosity of water) of $0.894cP$ or $8.94 * 10^{-4} Pa * s$. The second set is values extrapolated from previously published experimental results utilizing dynamic light scattering of longer ds-DNA chains (table 8 / figure 41).[112, 113]

Table 7 – Zimm Model Theoretical Values

DNA(kbp)	L (um)	N	R_g (nm)	t_1 (ms)	D_{Gth}(um^2/s)
0.5	0.17	1.67	55.2	0.174	11.92 (rod) / 7.76 (semi)
1	0.34	3.33	82.9	0.589	4.60
2	0.68	6.67	124.6	2.005	3.06
4	1.36	13.3	187.2	6.809	2.04
6	2.72	20.0	237.6	13.92	1.60
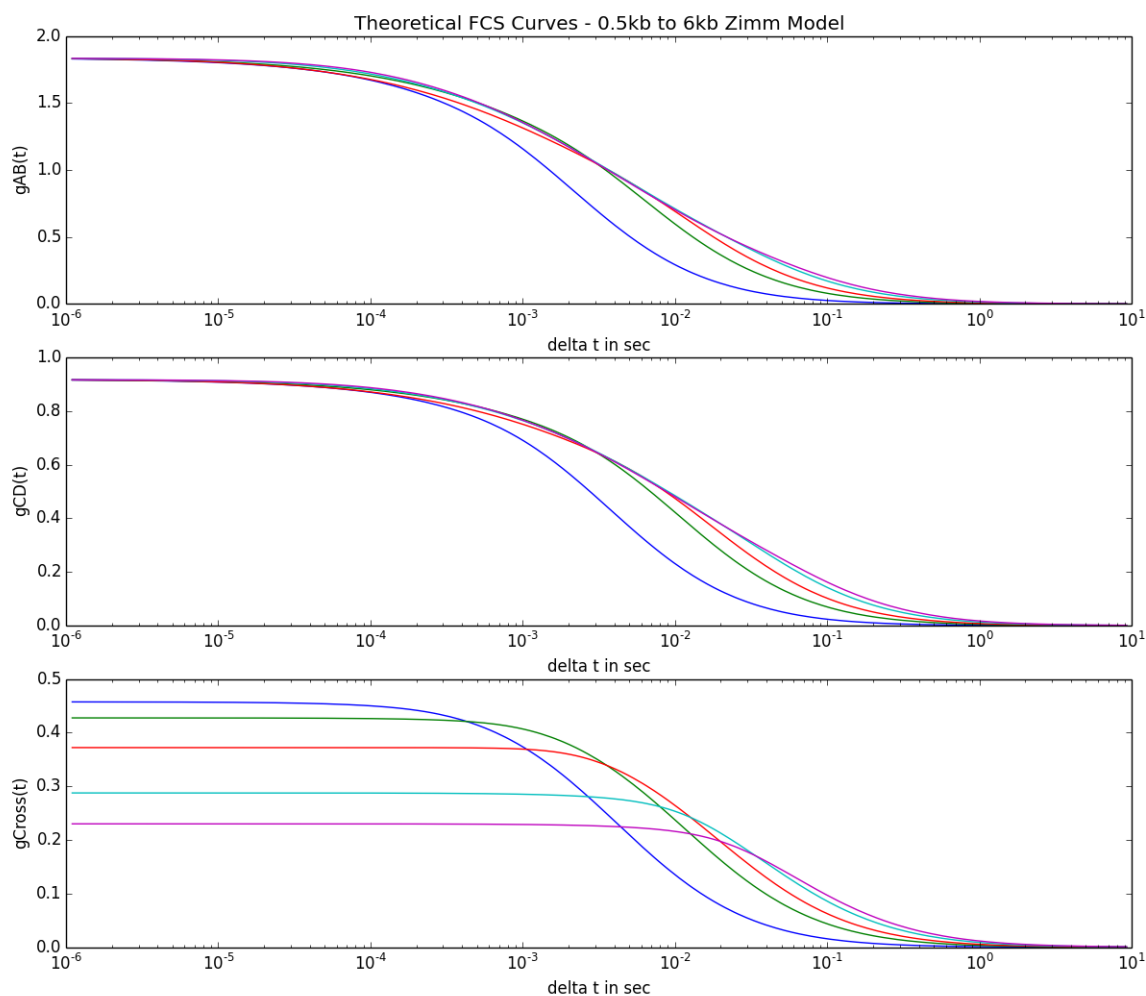
Figure 40 – Theoretical FCS curves incorporating polymer dynamics theory and values from

Table 7. 500bp (blue), 1000bp (green), 2000bp (red), 4000bp (cyan), 6000bp (purple)

Table 8 – Experimental Fitting Parameters extrapolated from Sorlie and Pecora[113]. Alternative R_g(right) calculated from Smith et al.[47, 54]

DNA(kbp)	R_g (nm)	t_1 (ms)	D_{exp}
0.5	37.1 / 52.7	0.012	12.28
1	59.9 / 80	0.049	7.68
2	96.9 / 121.3	0.204	4.81
4	157 / 183.8	0.841	3.01
6	207 / 234.4	1.926	2.28
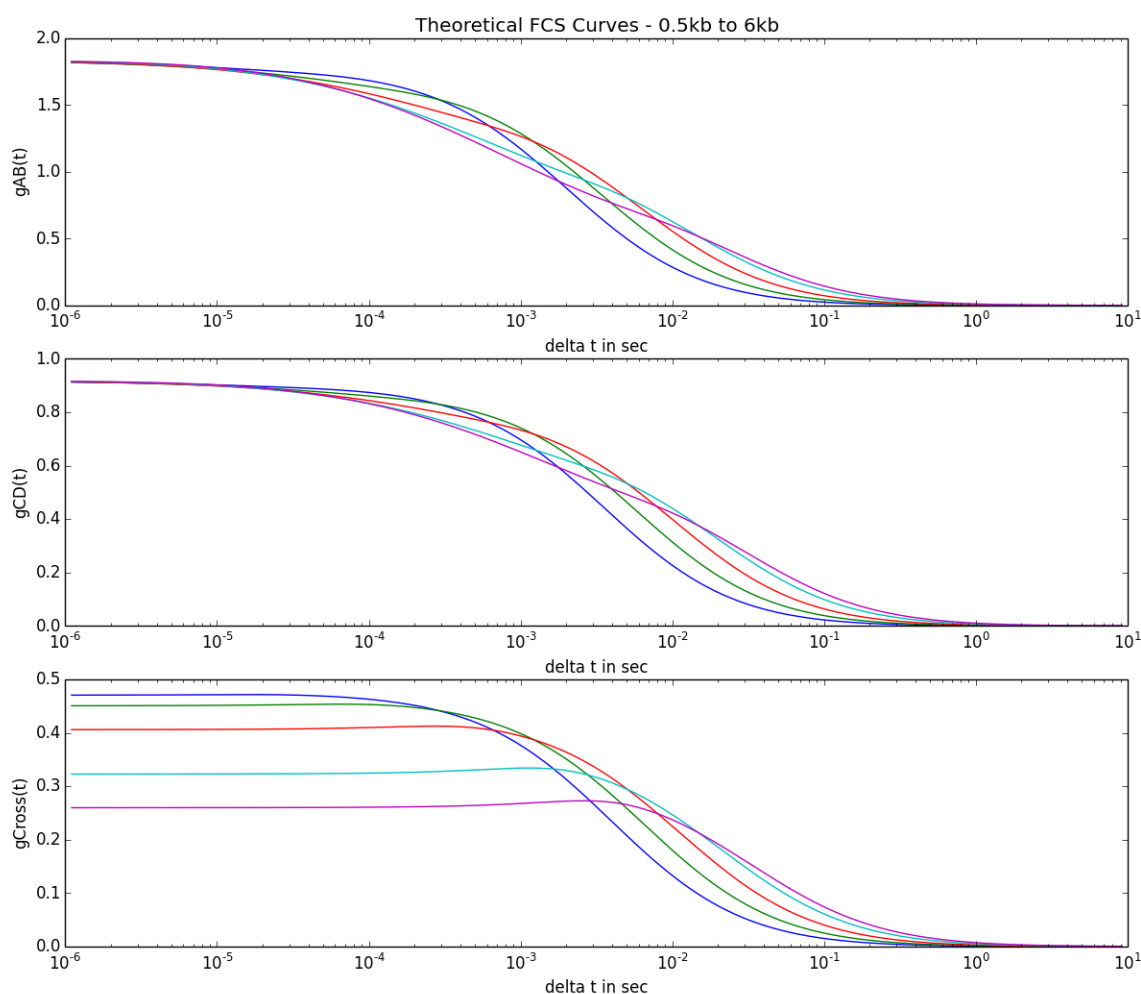
Figure 41 – Theoretical FCS curves incorporating polymer dynamics theory and values from Table 8. 500bp (blue), 1000bp (green), 2000bp (red), 4000bp (cyan), 6000bp (purple)

To better visualize the effect of the diffusion coefficient, radius of gyration, and relaxation time on the fitting of polymer dynamics in auto- and cross-correlation curves, figures 42, 43, and 44 isolate the individual effects by varying each in turn using the theoretical equations derived

above. As expected, the effect of the diffusion coefficient is to shift the correlation function along the x-axis, where smaller diffusion coefficients / slower diffusion occurs as you move to the right. The more significant and unusual changes occur when varying the radius of gyration and relaxation time. The changing relaxation time, which is focused on the first mode relaxation, has a more subtle, but important effect on the correlation curves. Given the sensitivity of FCCS and the polymer dynamics at play, it is estimated that only the first order relaxation time plays a significant role.
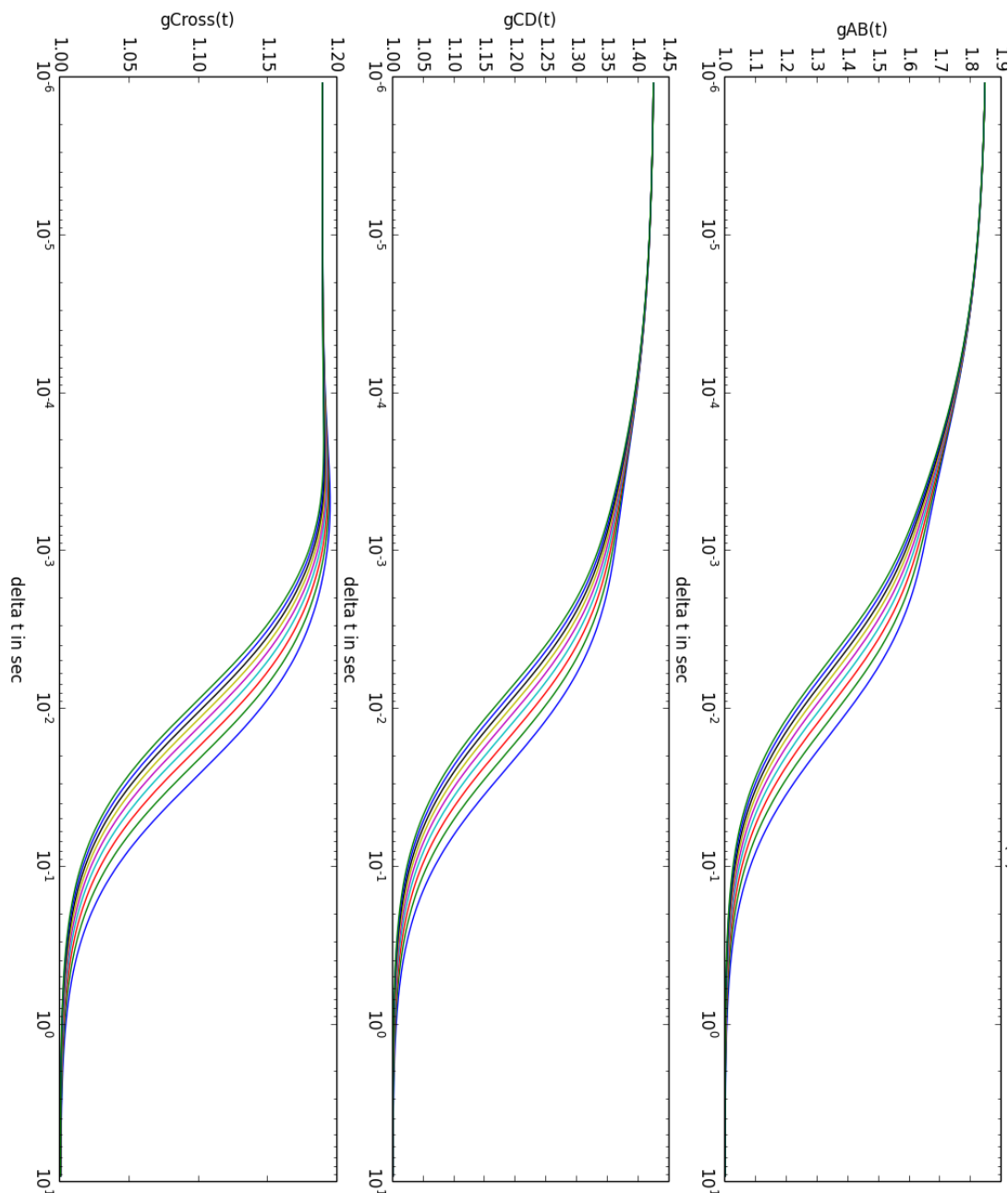
Figure 42 – Effect of changing *Diffusion coefficients* on theoretical FCS curves fitted with polymer dynamics
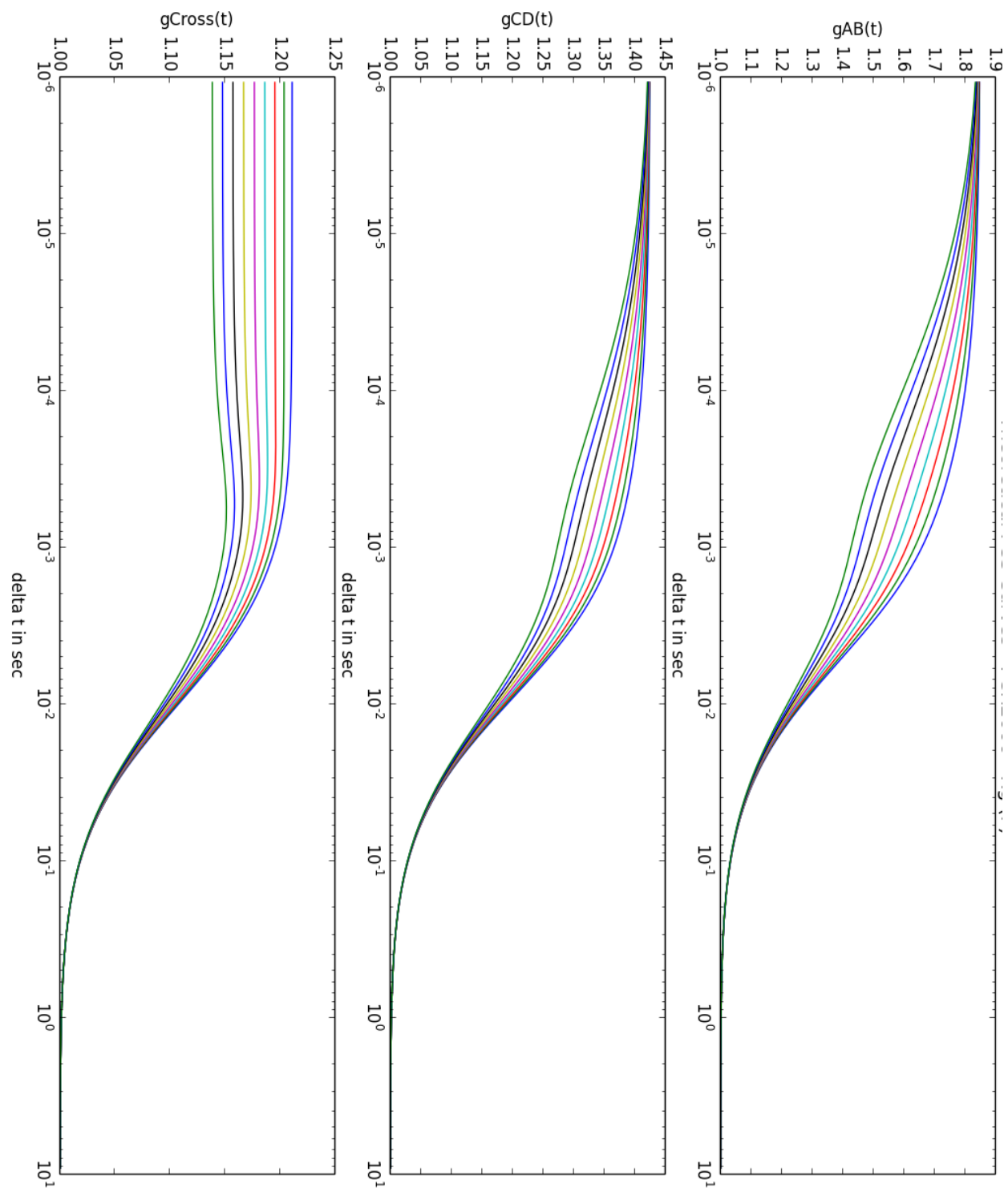
Figure 43 – Effect of changing *Radius of Gyration* on theoretical FCS curves fitted with polymer dynamics
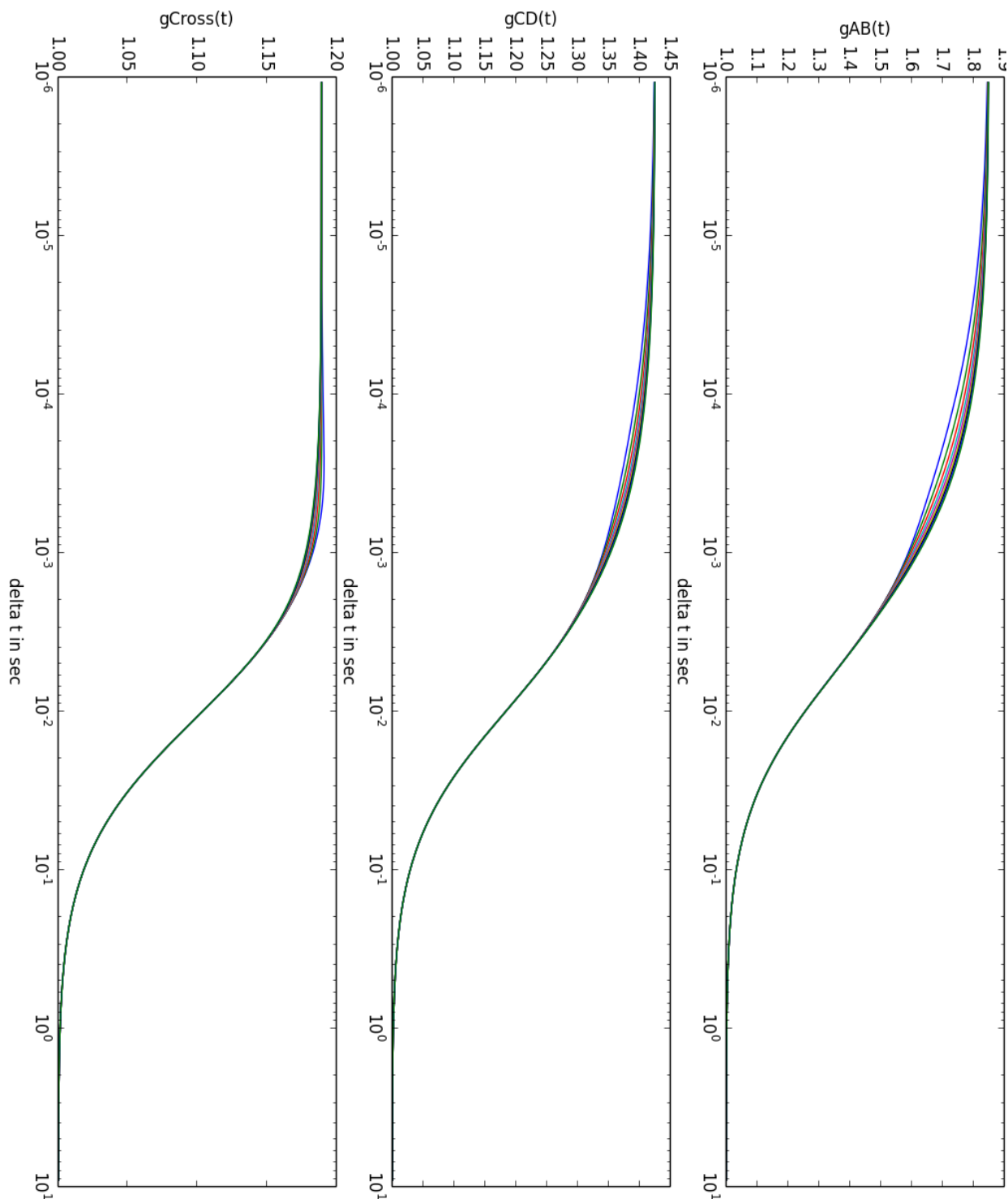
Figure 44– Effect of changing *Relaxation Time* on theoretical FCS curves fitted with polymer dynamics

These theoretical curves give a good starting point for comparison to what expected

experimental results from our FCCS might look like and how they would be fit. An important characteristic of the CCFs for both models is the fact that instead of plateauing, as was visible with the FCCS standard, the CCF demonstrates a drop in the amplitude of the curve as it approaches $t(0)$. A similar, but opposite effect, is seen for the ACFs as the curves evidence a rising at short time scales rather than a plateauing and a flattening of the curve at intermediate time scales. These effects are important as it highlights some of the important polymer dynamics expected.

C. Methods

Multiple strategies were initially employed for the double-end labeling of DNA. These included
1. **Complementary DNA-oligo assembly** with two different fluorescent labels are attached through the use of restriction enzymes and bridge oligos
2. **PCR** DNA double labeling utilizing forward and reverse primer pairs for developing different sized DNA fragments less than 20kb
3. **Quantum dot** double end labeling following methods

The DNA primarily used in these experiments is lambda phage, a virus that infects E. Coli, and commonly referred to as λ-DNA. It is well studied as a model organism and characterized physically as a model polymer.[50, 114] It is approximately 48kbp in length.

After multiple tests with all three methods, the easiest and most consistent results were found with the PCR approach as first reported by Takagi et. al. for using lambda DNA as a backbone and utilizing custom fluorescently labeled oligonucleotide primers.[115] Following PCR reaction, a polymer of whatever desired length can be produced. We focused on a range of 500bp to 6kbp, providing a range of stiffer, rod-like polymers and flexible ones. PCR was conducted using Platinum PCR Supermix (Invitrogen).

PCR primers were obtained from MWG Operon technologies with either Alexa 488, Atto 488, or Atto 633 dyes attached at the 5' ends. Primers were suspended as directed in 1x TE buffer at pH 7.5. Aliquots were created and frozen at -20°C. Samples were unfrozen prior to PCR. PCR was performed using Platinum Supermix (Life Technologies). Primers were diluted in reaction to a concentration of 2μM. Optimal PCR results were obtained by using 1μg of lambda DNA per 1.25mL of reaction solution. Standard PCR protocols were followed. DNA samples ranging from 500 to 6000bp were created.

Following PCR, each sample was purified in a 0.8% agarose gel (pre-cast / Invitrogen) to eliminate any primers, free dye, and other unwanted fragments. Samples were then further purified using either ethanol precipitation or the Nucleospin Gel and PCR clean-up kit (Machery-Nagel). The two purification steps were necessary to remove any unattached dyes, extraneous primers, and SYBR Safe dye that attached during gel purification. Without gel purification, FCS measurements showed significant increases in measured Diffusion coefficients, indicating the presence of smaller fragments.

Auto- and cross-correlation measurements of double-labeled DNA molecules of varying molecular weights were performed in solution. Buffer was 10mM each of HEPES, NaCl, and

EDTA. Each sample was measured for at least 20 repeats for a length 600 seconds or more. Repeats were then averaged and standard deviations determined. Collection followed the same scheme as illustrated in Table 4 for the FCCS standard.

D. Results - DNA in Solution

Two approaches were taken with the fitting of correlation curves obtained with PCR derived double-labeled DNA samples in solution. The first involved the determination of the MSD through an interpolation method and the second involved a modified numerical fit incorporating the polymer dynamics of DNA derived in **section V-B** within the numerical 2D Gaussian-Lorentzian fitting model derived in **Chapter III**. The implementation of both methods in python is shown in **Appendix VII**.

We first developed a method for extracting MSD information from correlation curves through the use of interpolation. Several experimental groups, notably Petrov et al, have previously utilized this method.[19, 20, 116] The method is focused on taking the correlation curve, which is typically fitted as a function time, and modifying it so that correlation is instead a function of MSD. This can be done by recalling that the MSD is related to time and diffusion coefficient as shown in equations V-11 and V-13. In order to calculate an MSD, one needs to first normalize the experimental ACF or CCF. The interpolation is performed over very short time scales with no expected polymer dynamics ($1e^{-6} - 1e^{-7}$ seconds). The bias is tested over a range of $\pm 15\%$ to ensure proper fitting. The interpolation bias and its choice can widely change the effectiveness of the MSD fitting approach. In fact,

From the logarithmic plot of $G(MSD)$ vs. MSD, one can interpolate values of MSD. These values are then plotted versus time.

For simple diffusion, the MSD is equal to,
$$MSD = 2Dt$$
When only simple diffusion dominates, the slope of the curve is linear, when plotted on a logarithmic scale. For more complex samples, such as longer DNA molecules, the MSD would exhibit bends or kinks at longer and shorter time scales as dynamics other than pure diffusion dominant. Additionally, more complex molecules require an additional fitting factor:
$$MSD = 2Dt + a$$

Equations V-11 and V-13 illustrate the respective fitting factors that are incorporated for single color (auto-correlation) and two color (cross-correlation) systems.

Utilizing multiple ACFs and a CCF one can further extend this method further by extracting the more complex features of the MSD by subtracting the interpolated results of ACF from the CCF. The pure diffusion term and the odd modes of the polymer dynamics, because of the $(-1)^p$ term in the double end label, would cancel, leaving only the even modes. Thus only the polymer dynamics of the correlation between the two ends would remain.

Figures 45, 46, and 47 demonstrate a typical fitting procedure for two molecular weight samples of double-labeled DNA, 4kbp and 6kbp. Figure 45 illustrates the original auto-correlation curves

for both color channels as they are normalized to a scale of 0 and 1 on the y-axis and graphed as function of mean square displacement. The fitting of these normalization curves utilizes the previous fit parameters already established for our FCCS system in **Chapter IV.** Next we focus on determining what the MSD is over a wide range of time by interpolating at fast time scales. In order for this interpolation to work, one needs to first find where the slope is equal to 1. This is typically at long time scales; however, as can be seen from figure 46, not only is it difficult to reliably judge where the proper normalization for the interpolation can be found, but also the interpolation is extremely sensitive to the normalization.
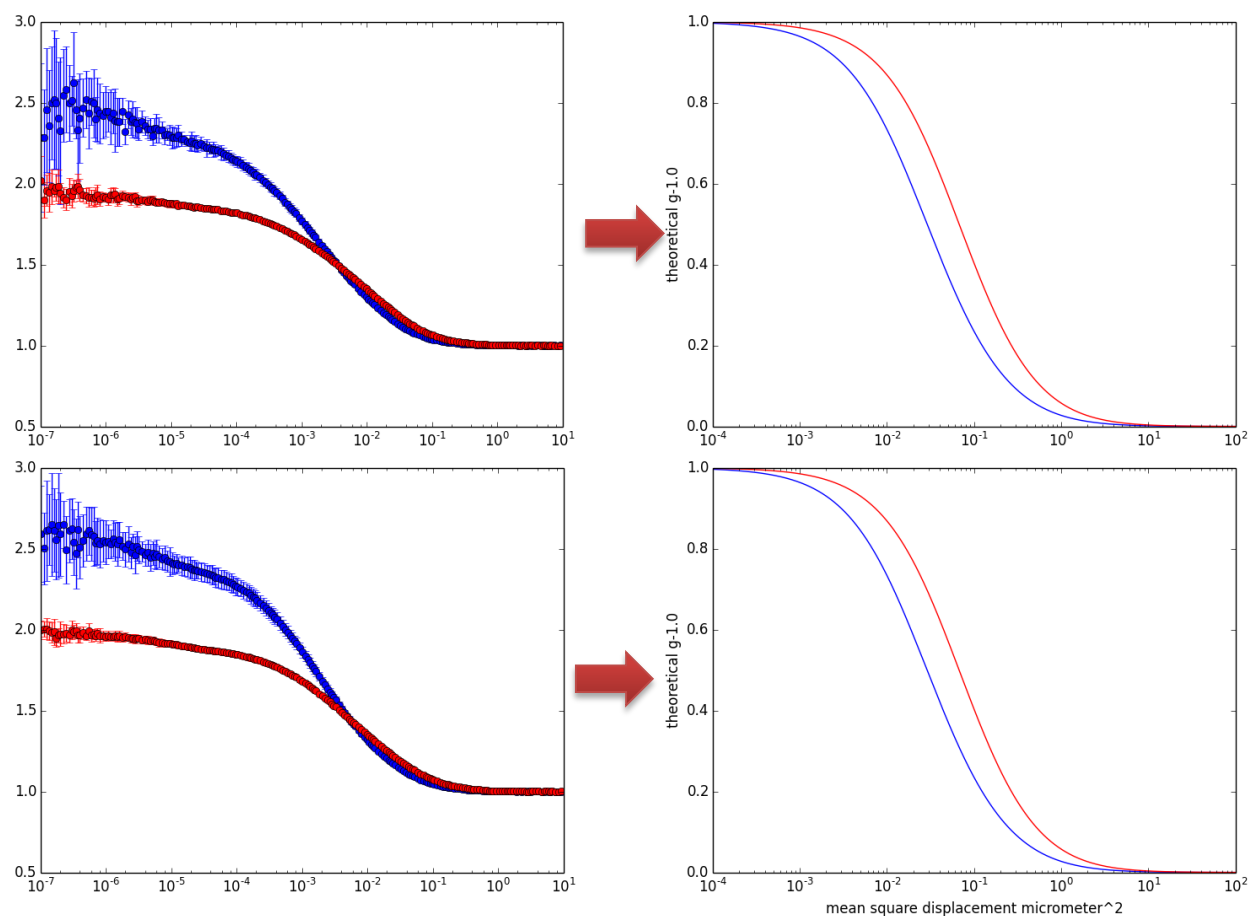
Figure 45 – Normalization of multiple auto-correlation curves for DNA of 4000bp (top row) and 6000bp (bottom row). Original auto-correlation curves are displayed in the left column and normalized curves are graphed as a function of mean squared displacement in the right column

The final interpolation fit is shown in figure 47. Unlike previous groups that focused on only one end label, we had an internal control through the use of two end labels. However, in performing the MSD analysis, both end labels were found to consistently diverge in intermediate and short time scales. The limited agreement in intermediate time scales prevents one from determining what the actual MSD might be and therefore comparing with the cross correlation function. It is therefore unlikely that previous groups were able to effectively capture the polymer dynamics of their systems correctly and may go some way in explaining differences seen amongst multiple groups in terms of the dynamic regimes reported (Rouse, Zimm, other).[20, 72, 117, 118]

Additionally, previous literature focused on teasing out polymer dynamics using a mean square displacement interpolation approach failed to elaborate on the precise methods utilized. Depending on the interpolation bias set during fitting, the final result can be arbitrary. It also becomes difficult to rationalize this approach particularly given that past implementations have relied on the use of the MSD within the 3D Gaussian model, which has been shown to be a poor quantitative model when applied to anything beyond simple systems. It reinforces some criticisms that have been leveled against the use of FCS to try to extract information that may not be possible.[75]
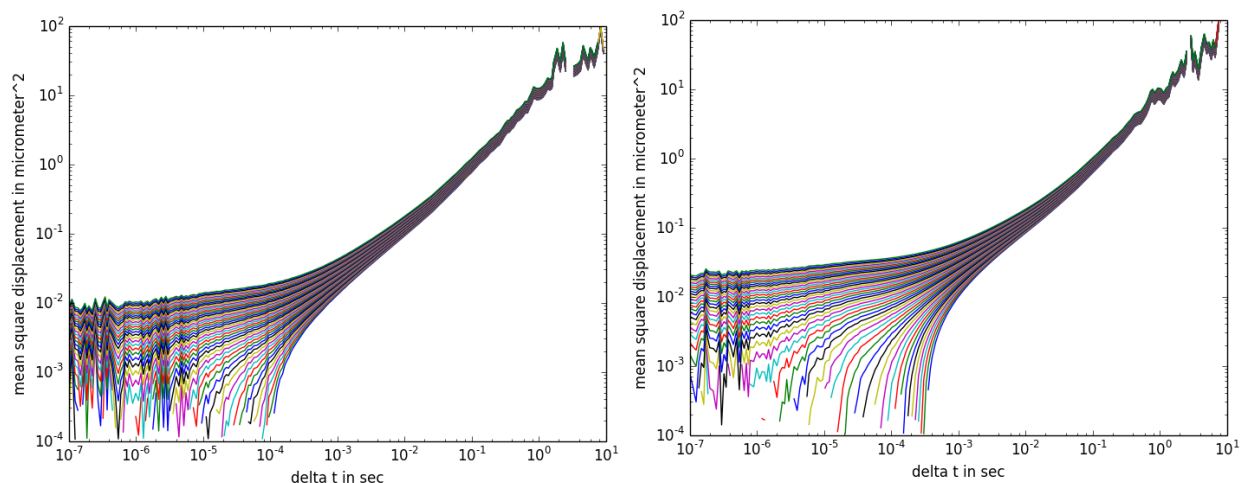
Figure 46 – Interpolation of the normalized FCS curves shown in Figure 45 for 4000bp sample. Blue end label interpolation shown on left. Red end label interpolation shown on right.
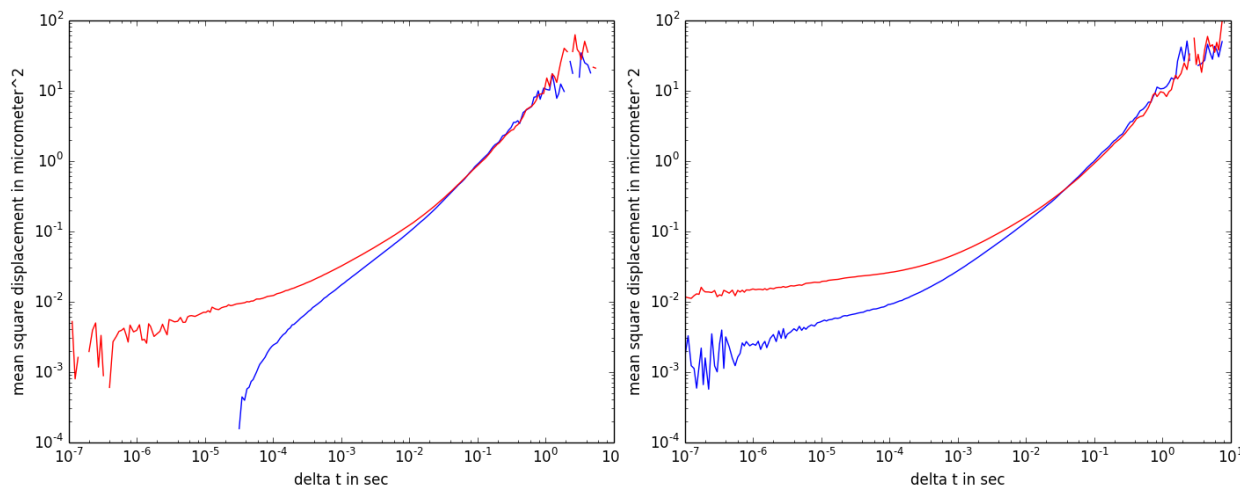
Figure 47 – Graph of MSD vs time for 4000bp (left) and 6000bp (right)

Our second approach focused on implementing the MSD theory derived in **Chapter V-B** within the numerical fitting model.

An example full fit of (auto- and cross-correlations) for the same longer PCR sample (4000bp) as in Figure 47 is shown in figures 48 and 49. Calibration measurements performed with dyes and oligos informing the fitting parameters. The fitting program utilizes a fixed $w_{xy}, R_0, \Delta z$ to

determine the $D, C, R_g, t1$ with a global fit. As can be seen, the CCF drops off significantly as compared to the oligo and predicted by theory (figure 41).

As expected, the model proposed does not entirely fit the experimental curves perfectly, nor does it produce values that are entirely in line with either previously published results or theory (Zimm model); however, diffusion coefficients seem to agree better with previous experimental results (table 8) than the theoretical values (table 7). The precise values for the radius of gyration and relaxation time, while adhering to expected trends by increasing appropriately with increasing molecular weight / length, do not match expected physical values.

This could be for multiple reasons. The first is that the current model was calibrated by using the Zimm model as the backbone (equation V-19). As a result, it's structure and power laws may not be entirely representative of the experimental situation. Additionally, the current implementation of the theory in the fitting model seems to not entirely account for the rise of the ACFs on short time scales.

Fitting each molecular weight along a single color channel utilizing radii of gyration taken from the Zimm model values results in the fits seen in figures 50 thru 54. The same fits were performed for the blue end label. Both ACFs resulted in different values for concentration, diffusion coefficient, and relaxation time. This indicates the inability to conclusively extract any quantitative information from single color FCS curves, as is usually done by several experimental groups, without a significant adjustment of the fitting model to incorporate both auto- and cross-correlation curves as well as address the model limitations.[20, 72, 117, 118]

Realizing the limitations of the current polymer dynamics model, the ACFs for the polymers were fitted with fixed radii of gyration in order to extract values for D and t1 (relaxation time). This is justified both in that the radii of gyration have been measured many times before and can be easily calculated and that the fits can be done purely in terms of diffusion and relaxation time. The Rouse and Zimm models indicate that the first order relaxation time t_1 should scale according to a power of $1 + 2v$ and $3v$, while the diffusion coefficient should scale with the power of $\sim MW^{-1}$ and $MW^{-\frac{2}{3}}$, respectively.

Previous results have indicated that Zimm regimes have been observed for DNA molecules greater than 23kbp, while intermediate Rouse-like regimes were reported for molecules in between 2.4kbp and 23kbp; however these results have seen contested and the only consistency in identifying Zimm regimes has been for very long polymers far exceeding 10kbp. [19, 20, 117, 118]

The use of the Zimm model was chosen as a starting point, but our experimental results, while close, do not seem to match either theory (figures 55 and 56). They highlight the differences between the two single end labels. Additionally, these power laws indicate that further study and refinement of the fitting models will be required to fully elucidate the dynamics at play.
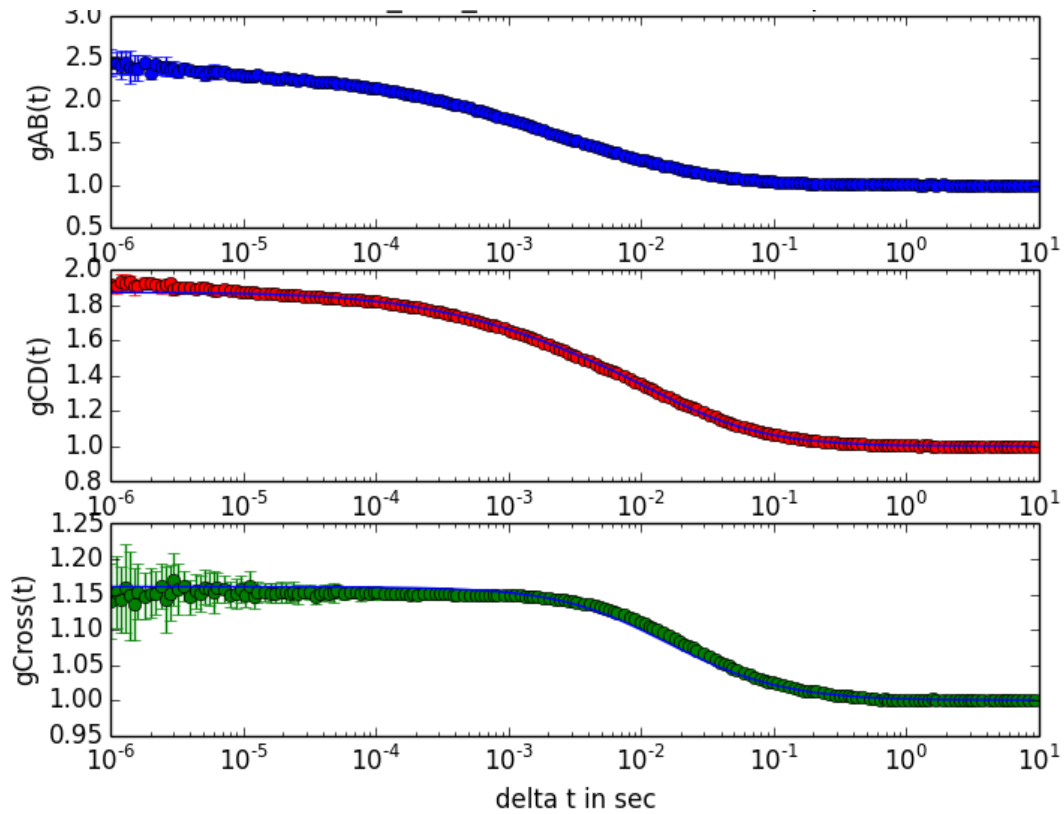
Figure 48 – Numerical fit of 4000bp PCR sample
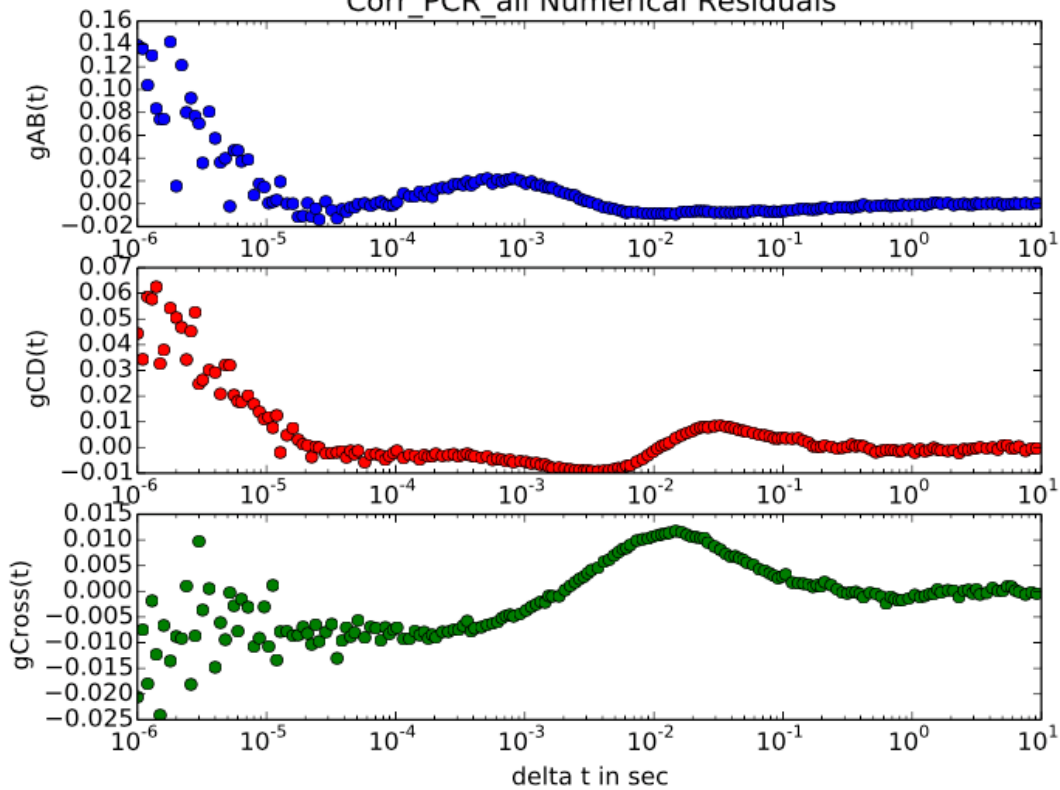
Figure 49 – Residuals of results from figure 45
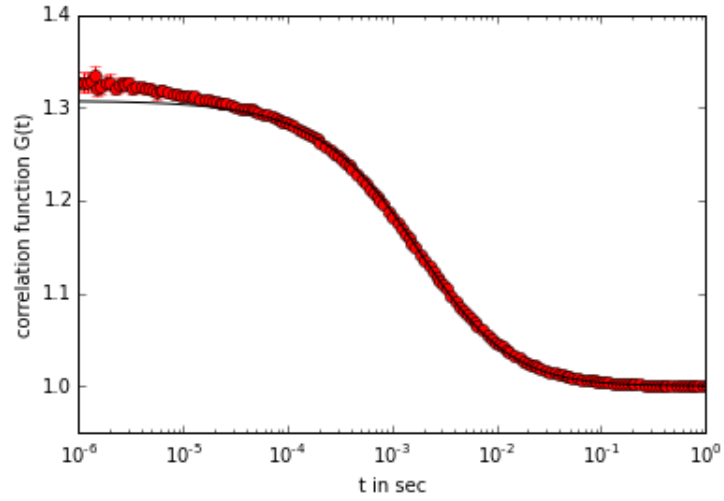
Figure 50 – 500bp Red label Autocorrelation fit
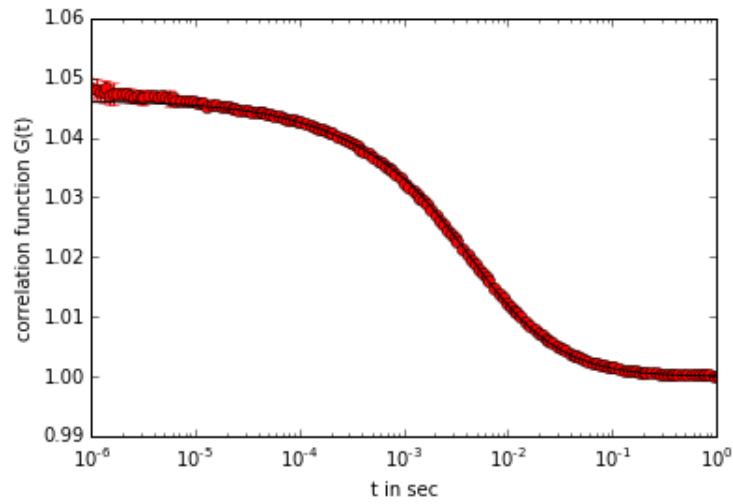
Figure 51 – 1000bp Red label Autocorrelation fit
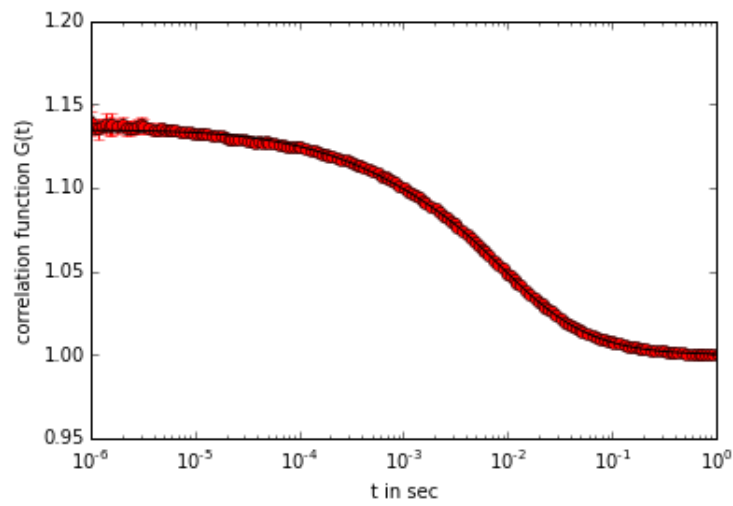
Figure 52 – 2000bp Red label Autocorrelation fit
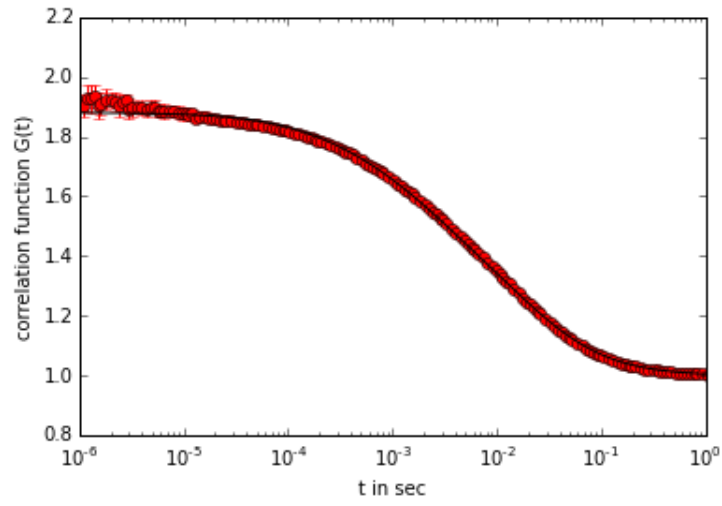
Figure 53 – 4000bp Red label Autocorrelation fit
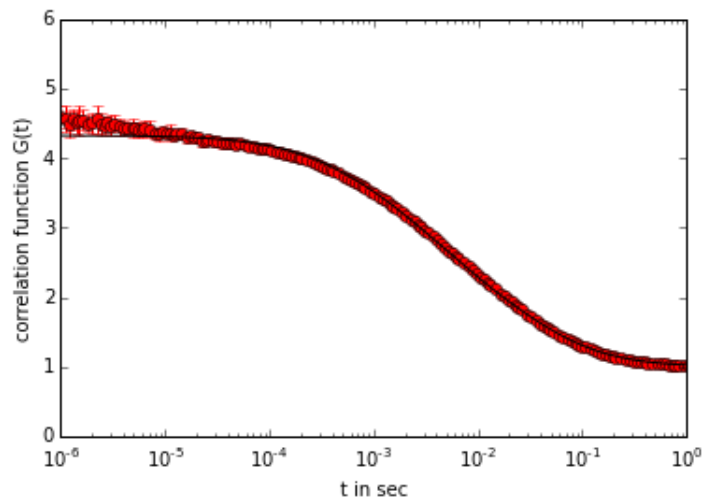
Figure 54 – 6000bp Red label Autocorrelation fit
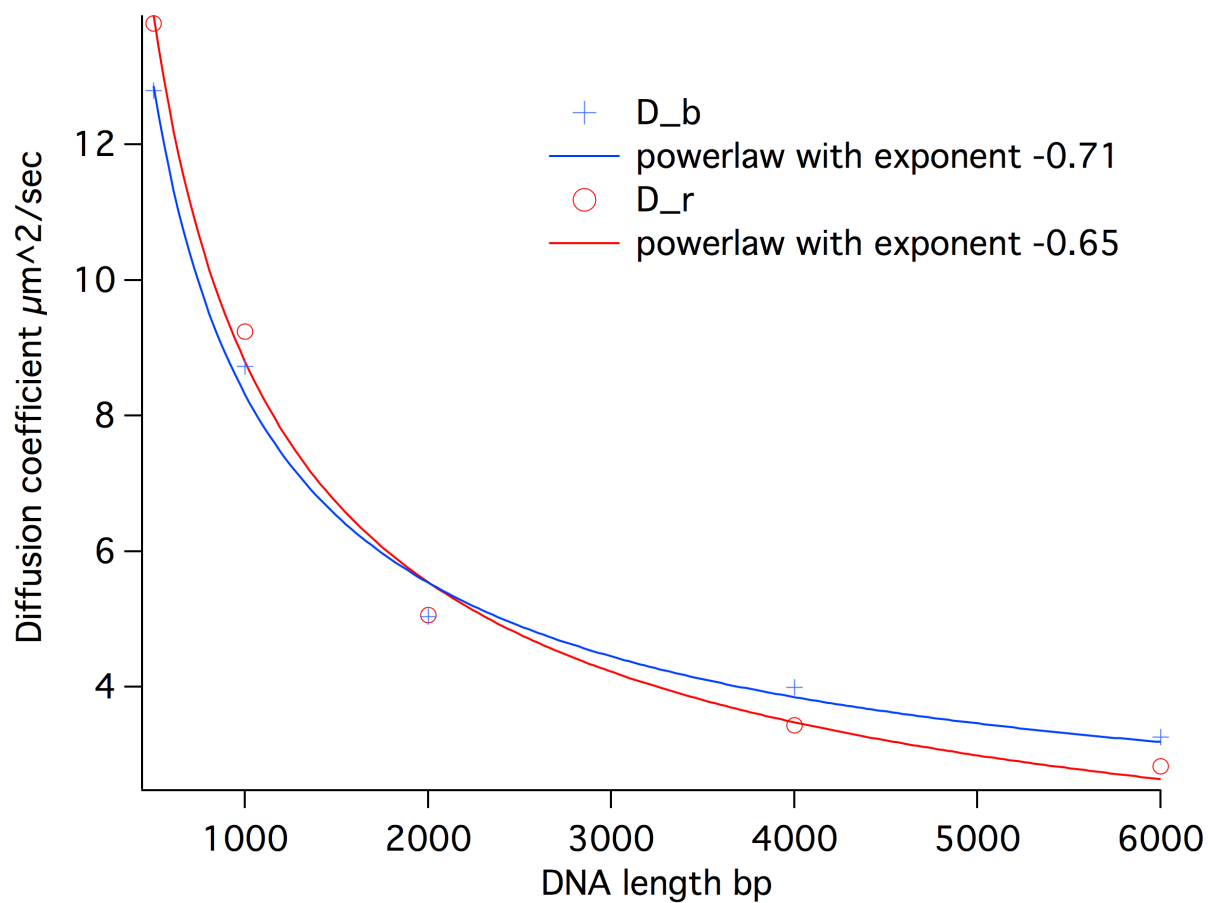
Figure 55 – Diffusion coefficient vs DNA length
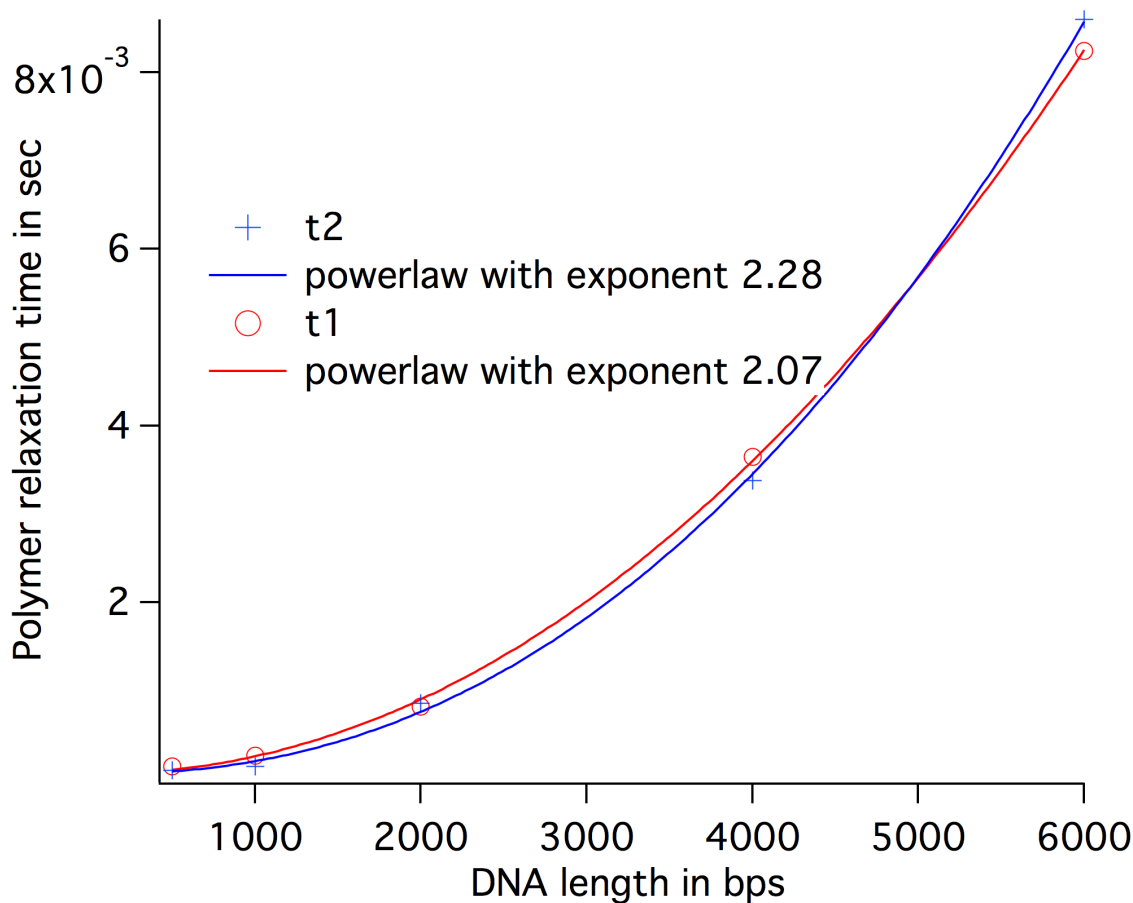
Figure 56 – Relaxation time vs DNA length

E. Conclusions and Future Work

We illustrated the utility of the FCCS platform as a way to quantiatively measure the dynamics of DNA at molecular weights smaller than previously tested with similar setups. We highlighted the quantitative determination of diffusion coefficients and first order relaxation times along with power laws for both that are in line with previous dynamic light scattering experiments and theory, but highlight important differences. Additioanlly, the limitations of previous approaches utilizing only a single-end label measurement and determination of MSD through an interpolation approach were demonstrated.

Future work will be necessary to flesh out the inconsistencies highlighted in the previous sections, especially as related to the power laws identified for the DNA. The combination of theoretical and experimentally fitted curves underscore that the incorporation of the MSD in it's current form is only a starting point as the dynamics witnessed in experimental curves seems to not follow either Rouse (expected) or Zimm models (less expected result). It is known that the theoretical frameworks that are in play in polymer dynamics are imperfect estimations.

The focus will have to be on a continual refinement of the two approaches. The polymer

dynamics theory will have to be tested against additional DNA measurements and utilized perhaps to calculate additional theoretical curves by varying the power laws in play and the parameters that are allowed to vary and under what boundary conditions.

The theoretical and experimental foundation is set to definitively elucidate the polymer dynamics and corresponding power laws at play that may indicate the need for revised theoretical treatment beyond the standard Zimm model.

VI.   DNA In Confined Geometries

The ultimate goal of this work is to extend the characterization of double-labeled DNA samples into nano-fabricated channels utilizing the platform FCCS built in **Chapter IV** and compare the polymer dynamics under confinement with those obtained in solution (**Chapter V**). We hope that the initial work in this chapter lays the groundwork for future studies, taking advantage of the advances made in the previous chapters.

Nano-slit (shallow, wide channels) chips were designed and fabricated in borosilicate glass utilizing standard nanofabrication techniques. Multiple strategies for bonding/sealing nanostructures were tested. Significant time and effort was spent troubleshooting and developing a clear nanofabrication protocol; however, construction still suffers from limited consistency. Both freely diffusing fluorophore and double-labeled DNA oligonucleotides were preliminarily tested within nano-slits utilizing the FCCS previously designed and characterized. Preliminary issues were identified.

I.   DNA Under Nanoconfinement

Polymers confined in nanostructures evidence unique dynamics not present in bulk solution. Confining molecules to regions below the 100nm length scale allows polymers to be controlled and observed individually rather than in bulk.

The goal of this work was to fabricate sealable and reusable nano-slits, which are defined as shallow and wide channels, through which to flow DNA molecules through and capture dynamics information utilizing both fluorescence microscopy and FCCS. This would extend the work of several research groups.[5, 6, 8, 119, 120] The result of these studies can be summarized as follows: at moderate confinements (Radius of gyration R_g > h > Persistence length l_p) both the lateral diffusion as well as the slowest internal relaxation time scale inversely with the channel height. For strong confinement (h < l_p) the internal relaxation time gets smaller as the molecule becomes more confined. This behavior is associated with the transition from the DeGennes regime to the Odijk regime in which the molecule becomes essentially two-dimensional. Additional discussion of theory can be found in **Chapter I-E**.

All previous studies have employed fluorescence microscopy to measure the diffusion coefficients and internal relaxation times, which as previously discussed, limits the size of molecule that can be studied and the information that can reasonably be extracted. [5, 6, 8, 119, 120] By extending the study of confined semi flexible polymers to smaller molecular weights (less than 20kbp) and utilizing FCCS, one would be able to access relaxation times and dynamics not verified experimentally.

DNA can be delivered in solution into nano-slits or channels through capillary forces. Typically, an electric field is applied as a driving force in order to manipulate the DNA within the channels.[121] A voltage of 10-30V potential across the nanostructure is typically sufficient to drive DNA within.[122]

The theory for fitting with FCCS would have to be modified as only a small fraction of the

confocal volume would be located within the nano-slit (figure 32).[123]
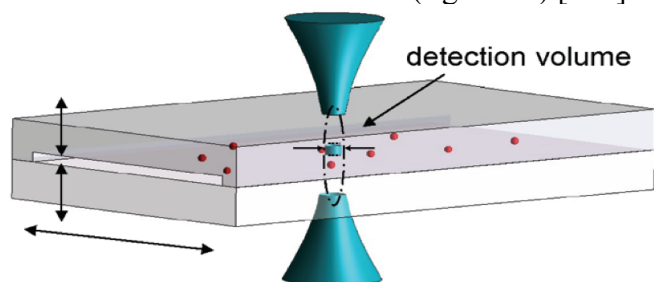
Figure 57– Illustration of the reduction in confocal volume size within a nano-slit. Adapted from et. al.[123]

A 2D Gaussian could be utilized, given the small heights (~100nm) relative to the axial size of the confocal volumes (at least one order of magnitude larger). Several studies have focused on the use of a 2D Gaussian within nanoconfinement, although none of them utilized more than one color. [123, 124]

The 2D Gaussian-Lorentzian form established early could serve as a more robust fitting method. By knowing the axial separation of the confocal volumes precisely, one could scan along the axial direction to determine where the minimum $G(0)$ would be measured. This point, if found for both colors would allow for precise positioning of the two confocal volumes and, therefore, a precise estimation of the overlapping confocal volume within the nano-structure (figure 58).
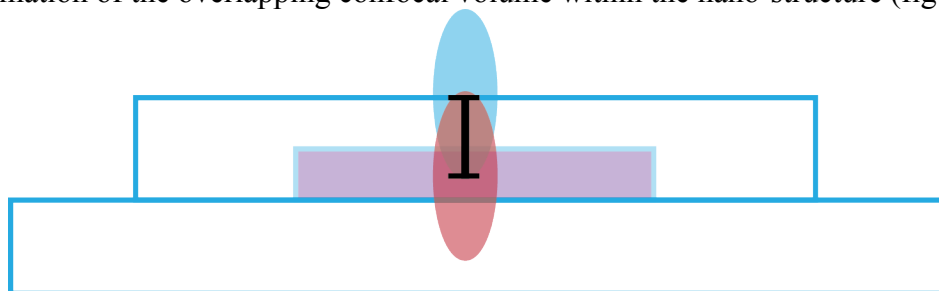
Figure 58 – Schematic of axial separation of confocal volumes in nanostructure

II.   Nanofabrication

Two alternatives are presented in figure 59. Both are similar, with the method demonstrated in B being technically easier with the primary differences being the time required for the protocol as well as channel height differentiation across one chip.

In the first method, different heights for the micron wide access channels and nano-channels/slits are established. In the second method, the wide access channels and nano-channels/slits share a common height profile.

Both protocols are mapped out in full detail in **Appendix VIII** with the differentiating steps marked out clearly. Each step indicates precise chemical and material requirements as well as any variation from standard operating procedure. Some parameters are flexible depending on

material and technological availability. All steps were carried out at the Center for Functional Nanomaterials at Brookhaven National Labs, Upton, NY
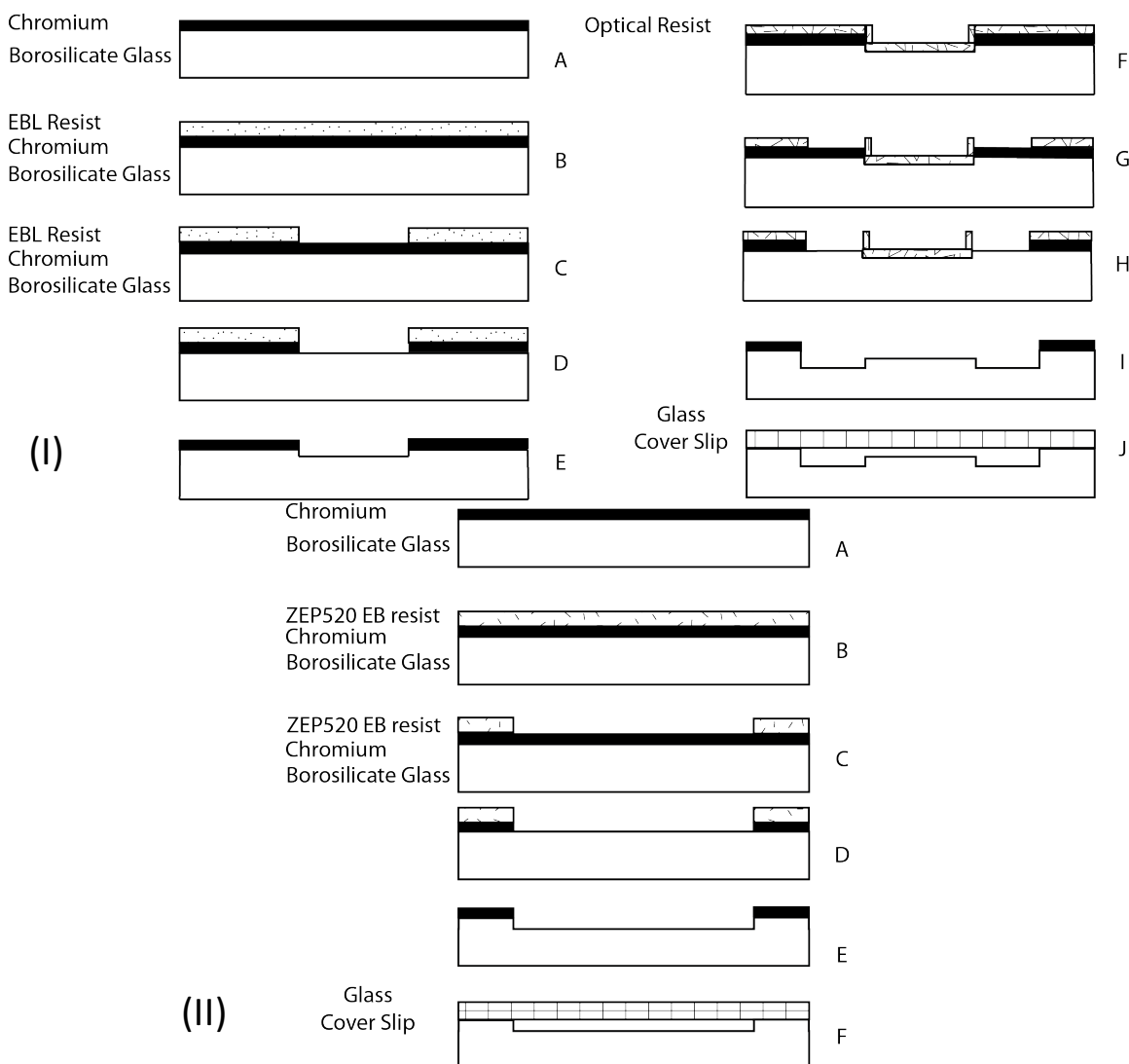
Figure 59 - Two alternative strategies for nanochannel fabrication (Side view)

I in more detail:

We start with a borosilicate glass piece or wafer that is ideally double side polished in order to minimize roughness and bowing. We then evaporate a thin layer of chromium (25 to 50nm / variable) on top of the polished side of the wafer (A). Electron beam lithography resist (ZEP520A) is spun on top of the chromium layer (B). Following e-beam lithography (JEOL JBX-6300FS), the pattern is developed using xylene (C). Pattern is transferred to chrome using a chromium wet etch (Transene Chromium Etchant 1020) (D). Sample is cleaned to remove any remaining resist. Pattern is etched into glass using either a HF wet etch or a reactive ion dry etch (Oxford Plasmalab 100) (E). Optical resist (Shipley S1800 series) is applied on top of the processed sample (F). Optical lithography (Karl Suss MA6) is performed using alignment marks

(G). Sample is developed using photodeveloper (MF312) mixed with DI water (G). Pattern is transferred into glass using either a HF wet etch or a reactive ion dry etch (Oxford Plasmalab 100) (H). Remaining resist and Chrome is removed (I). Blank glass coverslip is bonded to the sample (J).

II in more detail:

We start with a borosilicate glass piece or wafer that is ideally double side polished in order to minimize roughness and bowing. We then evaporate a thin layer of chromium (25 to 50nm / variable) on top of the polished side of the wafer (A). Electron beam lithography resist (ZEP520A) is spun on top of the chromium layer (B). Following e-beam lithography (JEOL JBX-6300FS), the pattern is developed using xylene (C). Pattern is transferred to chrome using a chromium wet etch (Transene Chromium Etchant 1020) (D). Sample is cleaned to remove any remaining resist. Pattern is etched into glass using either a HF wet etch or a reactive ion dry etch (Oxford Plasmalab 100) (E). Chrome and any remaining resist are removed. Blank glass coverslip is bonded to the sample (F).

The main difference between Figure 59-I and –II is the type of lithographic method employed. Optical lithography also offers the flexibility of quickly testing some larger new designs as compared to electron beam lithography (EBL). EBL is required for more advanced unique geometries. An example is an array of spherical cavities of varying diameters (on the order of 1um) interconnected by thin (on the order of 100nm) nanochannels of varying lengths and widths (figure 60).
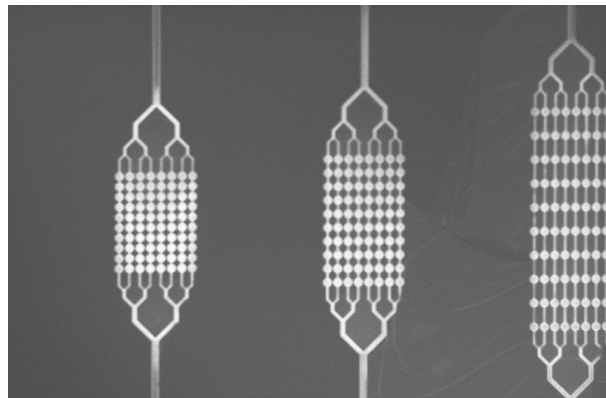
Figure 60 - SEM of nano-cavity array

Both dry and wet etching were tested with varying materials (silica wafers coated with silicon dioxide, fused silica glass, and borosilicate glass) and varying etch masks. Characterization of the etching was done with SEM and AFM to verify etch depth. The roughness of these channels was found to typically be minimal at less than 5 angstroms, as shown in figure 61.
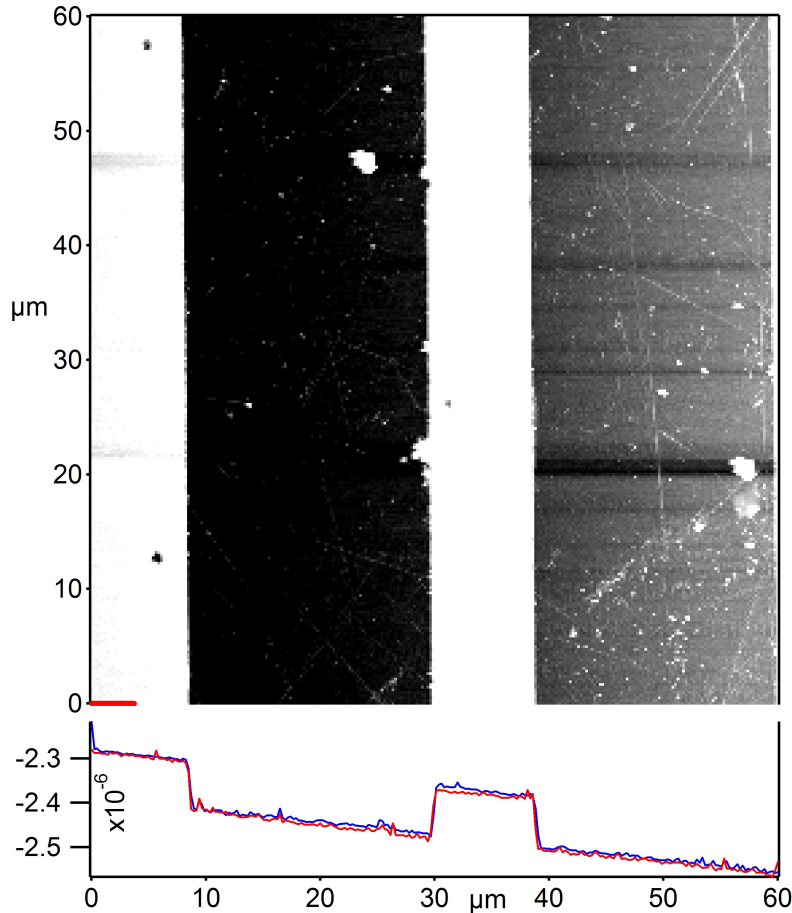
Figure 61 – AFM measurement of typical etched glass substrate

The final aspect of the fabrication involves bonding of the etched channel surface to a blank glass piece. This aspect of the work served as one of the most difficult roadblocks in the nanofabrication process.

Three strategies for addressing this were tested. The first and initial strategy attempted involves fusion thermal bonding; however, this technique is notoriously finicky and inconsistent in its application. It requires a dust free environment and careful optimization of the bonding protocol. Following consultation with the Doyle Group at MIT, based off of the work of Mao et. al, some success was obtained, but fewer than 10% of channels fabricated resulted in permanent bond.[125] Most bonds were imperfect showing significant interference fringes.

Another limitation of thermal bonding is the development of cracks that occur during the sealing process because of the difference in the thermal expansion between the substrate and the sealing material.[56, 126-129]

The second proposed alternative strategy involves Indium bonding. As suggested in discussions with CFN staff, 100 Angstroms of Indium was sputter evaporated onto a flat glass surface. The surface was sandwiched to the other glass chip with the etched channels. The thin layer of Indium was suggested to bond under compression if the sample is cleaned prior to bonding utilizing piranha etch and subsequently activated with oxygen plasma; however, further study found that without a strong electric potential being applied, this process would not work.

A third alternative strategy focused on bonding utilizing PSQ (polysilsesquioxane) thin film activated with O2 plasma, eliminating the need for thermal fusion bonding. PSQ is a silicon

73

resin, synthesized using trifunctional organosilane compounds. Apart from excellent heat, electrical, and chemical resistance, it also is highly transparent. The high Young's Modulus helps prevent collapsing.[130] This involves simple spinning of PSQ onto glass slide, followed by exposure to O2 plasma for activation, followed by room temperature bonding.[131] The mechanism of bonding is suspected to be similar to that involved in PDMS/glass bonding. O2 plasma treatment converts the surface hydrocarbon groups of PSQ to silanol groups (–SiOH) that can form strong (Si–O–Si) bonds with silanol groups on the glass surface through a condensation reaction.[132, 133] The method has since been extended for various micro- and nano-fabrication by other groups in recent years. [121, 134-136] The use of a relatively high pressure and low power plasma is crucial for preventing too much roughening of the PSQ surface prior to bonding. The exact protocol is listed in **Appendix VIII**. Approximately 50% of the samples made were successfully bonded, although bonded samples still show significant surface areas that were not ideally bonded i.e. interference fringes.
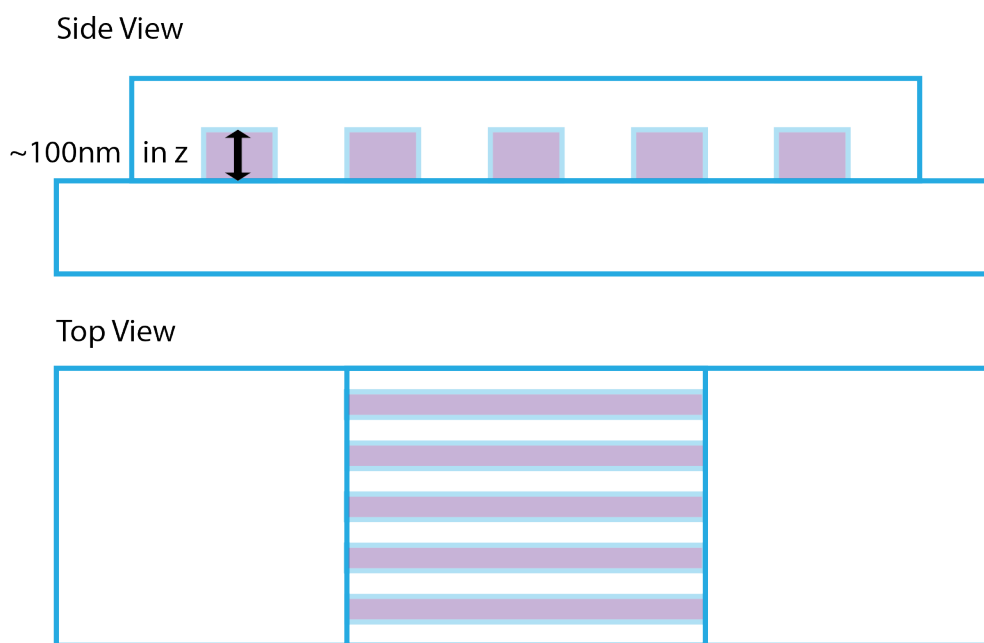
Figure 62 – Schematic of nanoslits, side and top views, not to scale

A schematic of a completed nano-slit chip is shown in Figure 62. Figure 63 illustrates nanochannels (100nm / widths ranging from 100um to 10um) filled with fluorescein solution to show that nanochannels do not collapse following thermal bonding and can be successfully made following the currently used protocol with a very large height to width ratio. Channel depth ranged between 50nm and 500nm with a minimum aspect ratio of 0.0004 with PSQ bonding.
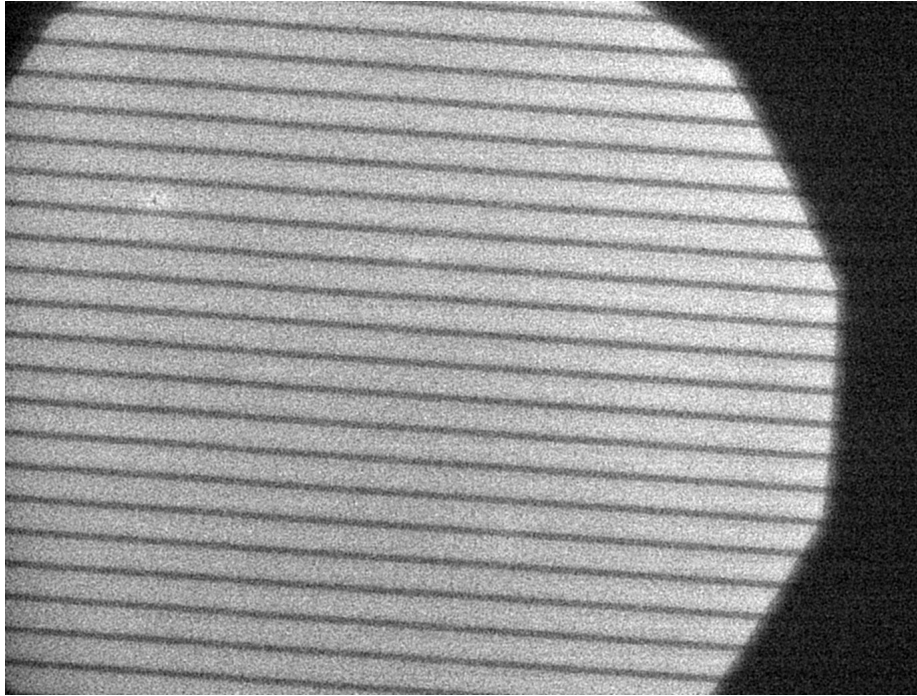
Figure 63 - Fluorescence Microscopy of nanoslits, width 10um, depth 100nm, lighter indicates fluorophore, darker sections indicate channel walls

VII. Conclusions and Future Work

The initial aims of this project focused on studying the internal polymer dynamics of DNA less than 50kbp under nanoconfinement. Fluorescence correlation spectroscopy was identified as a possible technique for observing these dynamics. In pursuit of these intial aims, it was identified that there were several shortcomings in the literature related to FCCS and it's application to polymer dynamics in solution as well as nanofabrication protocols.

Within the available time and the scope of this thesis, the focus was shifted towards addressing the aforementioned shortcomings and laying the groundwork for addressing our initial aim in future work.

In this work, we have designed, built, and characterized a custom built two-color FCS (FCCS) system at a tenth of the cost of commercial setups. Our hardware setup offers more control and flexibility and could serve as a more effective platform for answering several outstanding biological questions, in addition to polymer dynamics.

We developed an improved theoretical and fitting method by applying numerical methods to correlation analysis. We identified that a 2D Gaussian-Lorentzian model performs significantly better than a 3D Gaussian for extracting quantitative information with regards to the confocal volume. We addressed issues related to determining the axial separation of the two color confocal volumes. Our characterization shows the value of this method as compared to the traditional 3D Gaussian fitting approach.

We also further explored the dynamics of polymers in solution and how to properly utilize a FCCS towards extracting polymer dynamics. Utilizing the platform developed herein, future work studying and reliably quantifying the dynamics of polymers under confinement is now possible. No experimental group has yet to combine a fully quantitative approach to two-color FCS with nano-confinement to study polymer dynamics and the results remain an open question. Following successful measurements with nano-slits, the work can quickly be expanded into more complex nano-structures, such as the cavity arrays shown in figure 59. The end-labeled DNA would be introduced into the cavity arrays where FCCS could used to measure the frequency of unsuccessful and successful attempts to move from one cavity to the next and whether those attempts are end-first or by forming loops (figure 63). Many other exciting possibilities also exist.
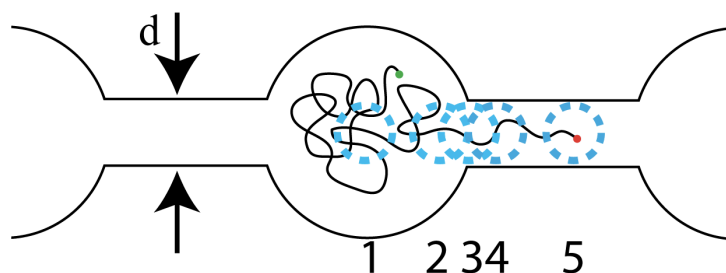
Figure 63 – Proposed FCS experiments to probe threading dynamics with each point illustrating a location to perform FCCS measurements.

References

1. Klotz AR (2011) Statics and Dynamics of DNA in a Network of Nanofluidic Entropic Traps. Master of Science (McGill University).
2. Salieb-Beugelaar GB, Dorfman KD, van den Berg A, & Eijkel JCT (2009) Electrophoretic separation of DNA in gels and nanostructures. *Lab on a Chip* 9(17):2508-2523.
3. Reisner W*, et al.* (2005) Statics and dynamics of single DNA molecules confined in nanochannels. *Phys Rev Lett* 94(19):-.
4. Schoch RB, Han JY, & Renaud P (2008) Transport phenomena in nanofluidics. *Reviews of Modern Physics* 80(3):839-883.
5. Bonthuis D, Meyer C, Stein D, & Dekker C (2008) Conformation and Dynamics of DNA Confined in Slitlike Nanofluidic Channels. *Phys Rev Lett* 101(10):108303.
6. Strychalski EA, Levy SL, & Craighead HG (2008) Diffusion of DNA in Nanoslits. *Macromolecules* 41(20):7716-7721.
7. Nykypanchuk D, Hoagland DA, & Strey HH (2009) Diffusion of Circular DNA in Two-Dimensional Cavity Arrays. *ChemPhysChem* 10.
8. Persson F, Utko P, Reisner W, Larsen NB, & Kristensen A (2009) Confinement Spectroscopy: Probing Single DNA Molecules with Tapered Nanochannels. *Nano Letters* 9(4):1382-1385.
9. Lin P-k, Hsieh C-C, Chen Y-L, & Chou C-F (2012) Effects of Topology and Ionic Strength on Double-Stranded DNA Confined in Nanoslits. *Macromolecules* 45(6):2920-2927.
10. Akerman B (1996) Barriers Against DNA-Loop Formation in a Porous Matrix. *Phys. Rev. E* 54:6685-6696.
11. Akerman B (1997) Threading Dynamics of a Polymer through Parallel Pores: Potential Applications to DNA Size Separation. *J. Chem. Phys.* 106:6152-6159.
12. Kholodenko AL (1996) Reptation theory: geometrical and topological aspects. *Macromol. Theory Simul.* 5:1031-1064.
13. Nechaev AGaS (1993) Polymer topology. *Advances in Polymer Science* 106:1-29.
14. Mukamel UAaD (1997) Gel electrophoresis and diffusion of ring-shaped DNA. *Physical Review E (Statistical, Nonlinear, and Soft Matter Physics)* 55:1783-1793.
15. Marko JF & Siggia ED (1994) Fluctuations and Supercoiling of DNA. *Science* 265:506-508.
16. Marko JF & Siggia ED (1994) Bending and Twisting Elasticity of DNA. *Macromolecules* 27:981-988.
17. M. Muller JPWaMEC (2000) Topological effects in ring polymers. II. Influence of persistence length. *Physical Review E (Statistical, Nonlinear, and Soft Matter Physics)* 61:4078-4089.
18. Rubinstein M (1986) Dynamics of Ring Polymers in the Presence of Fixed Obstacles. *Phys Rev Lett* 57:3023-3026.
19. Petrov EP, Ohrt T, Winkler RG, & Schwille P (2006) Diffusion and Segmental Dynamics of Double-Stranded DNA. *Phys Rev Lett* 97(25):258101.
20. Shusterman R, Alon S, Gavrinyov T, & Krichevsky O (2004) Monomer Dynamics in Double- and Single-Stranded DNA Polymers. *Phys Rev Lett* 92(4):048303.

21. Shusterman R, Gavrinyov T, & Krichevsky O (2008) Internal Dynamics of Superhelical DNA. *Phys Rev Lett* 100(9):098102.
22. Espejo RT, Canelo ES, & Sinsheim (1969) *Proc. Natl Acad. Sci.* 63:1164.
23. Arsuaga J & al. e (2002) Knotting probability of DNA molecules confined in restricted volumes: DNA knotting in phage capsids. *Proc. Natl Acad. Sci.* 99:5373.
24. Smith DE (2001) The bacteriophage [phis]29 portal motor can package DNA against a large internal force. *Nature* 413:748-752.
25. Kim Y*, et al.* (2011) Nanochannel confinement: DNA stretch approaching full contour length. *Lab on a Chip* 11(10):1721-1729.
26. Halford SE & Marko JF (2004) How do site‑specific DNA‑binding proteins find their targets? *Nucl. Acid. Res.* 32(10):3040-3052.
27. Berg OG & von Hippel PH (1985) Diffusion-controlled macromolecular interactions. *Annu Rev Biophys Biophys Chem.* 14:131-160.
28. Riggs AD, Bourgeois S, & Cohn M (1970) The lac repressor-operator interaction. 3. Kinetic studies. *J Mol Biol.* 53(3):401-417.
29. Berg OG, Winter RB, & Von Hippel PH (1981) Diffusion-driven mechanisms of protein translocation on nucleic acids. 1. Models and theory. *Biochemistry* 20(24):6929-6948.
30. von Hippel PH & Berg OG (1989) Facilitated target location in biological systems. *J. Biol. Chem.* 264(2):675-678.
31. I.M. Sokolov RM, K. Pant, and M.C. Williams (2005) Target Search of N Sliding Proteins on a DNA. *Biophys. J.* 89:895.
32. C. A. Brackley MEC, and D. Marenduzzo (2012) Facilitated Diffusion on Mobile DNA: Configurational Traps and Sequence Heterogeneity. *Phys. Rev. Lett.* 109:168103.
33. Florescu AM & Joyeux M (2009) Description of nonspecific DNA-protein interaction and facilitated diffusion with a dynamical model. *J. Chem. Phys.* 130:015103.
34. Gerland U, Moroz JD, & T. Hwa T (2002) Physical constraints and functional characteristics of transcription factor–DNA interaction. *Proc. Natl Acad. Sci.* 99:12015.
35. Schötz T, Neher RA, & Gerland U (2011) Target search on a dynamic DNA molecule. *Phys Rev E* 84(5):051911.
36. van den Broek B, Lomholt MA, Kalisch SMJ, Metzler R, & Wuite GJL (2008) How DNA coiling enhances target localization by proteins. *Proceedings of the National Academy of Sciences* 105(41):15738-15742.
37. Elf J, Li G-W, & Xie XS (2007) Probing Transcription Factor Dynamics at the Single-Molecule Level in a Living Cell. *Science* 316(5828):1191-1194.
38. Elf J, Li GW, & Xie XS (2007) Probing Transcription Factor Dynamics at the Single-Molecule Level in a Living Cell. *Science* 316:1191.
39. Wang YM, Austin RH, & C. CE (2006) Single Molecule Measurements of Repressor Protein 1D Diffusion on DNA. *Phys. Rev. Lett.* 97:048302.
40. P. Hammar PL, A. Mahmutovic, E.G. Marklund, O. G. Berg, and J. Elf (2012) The lac Repressor Displays Facilitated Diffusion in Living Cells. *Science* 336:1595.
41. Crick F (1970) Central Dogma of Molecular Biology. *Nature* 227:561-563.
42. J. D. Watson FHCC (1953) Molecular Structure of Nucleic Acids: A Structure for Deoxyribose Nucleic Acid. *Nature* 171:737-738.
43. Bao G (2002) Mechanics of biomolecules. *Journal of the Mechanics and Physics of Solids* 50(11):2237-2274.

44. De Gennes PG (1979) *Scaling Concepts in Polymer Physics* (Cornell Univ. Press, Ithaca).

45. Bustamante C, Bryant Z, & Smith SB (2003) Ten years of tension: single-molecule DNA mechanics. *Nature* 421(6921):423-427.

46. Doi M & Edwards SF (1986) *The Theory of Polymer Dynamics* (Oxford Univ. Press, New York).

47. Smith DE, Perkins TT, & Chu S (1996) Dynamical scaling of DNA diffusion coefficients. *Macromolecules* 29(4):1372-1373.

48. G. Beaucage SR, S. Sukumaran, M. M. Satkowski, L. A. Schecht- man, and Y. Doi. (1997) Persistence length of isotactic poly(hydroxy butyrate). *Macromolecules* 30(14):4158-4162.

49. B. G. Ricart BJ, D. Lee, C. A. Hunter, and D. A. Hammer (2011) Dendritic cells distinguish individual chemokine signals through ccr7 and cxcr4. *The Journal of Immunology* 186(1):53-61.

50. Bustamante C, Marko JF, Siggia ED, & Smith S (1994) Entropic Elasticity of lambda-Phage DNA. *Science* 265:1599-1560.

51. Mannion JT, Reccius CH, Cross JD, & Craighead HG (2006) Conformational Analysis of Single DNA Molecules Undergoing Entropically Induced Motion in Nanochannels. *Biophysical Journal* 90(12):4538-4545.

52. Flory PJ (1975) *Science* 188:1268-1275.

53. Stellwagen NC, Gelfi C, & Righetti PG (1997) The free solution mobility of DNA. *Biopolymers* 42(6):687-703.

54. Smith DE, Perkins TT, & Chu S (1995) Self-Diffusion of an Entangled DNA Molecule by Reptation. *Phys. Rev. Lett.* 75:4146-4149.

55. Larson R (1999) *The structure and rheology of complex fluids* (Oxford University Press).

56. Tegenfeldt JO*, et al.* (2004) The dynamics of genomic-length DNA molecules in 100-nm channels. *Proc. Natl. Acad. Sci. U.S.A.* 101(30):10979-10983.

57. Witz G & al. e (2008) Conformation of Circular DNA in Two Dimensions. *Phys. Rev. Lett.* 101:148103.

58. Odijk T (1983) On the Statistics and Dynamics of Confined or Entangled Stiff Polymers. *Macromolecules* 16:1340-1344.

59. Reisner W*, et al.* (2005) Statics and Dynamics of Single DNA Molecules Confined in Nanochannels. *Phys Rev Lett* 94(Copyright (C) 2009 The American Physical Society):196101.

60. De Gennes PG (1976) Dynamics of Entangled Polymer Solutions. I. The Rouse Model. *Macromolecules* 9:587-593.

61. Daoud M & Degennes PG (1977) Statistics of Macromolecular Solutions Trapped in Small Pores. *Journal De Physique* 38(1):85-93.

62. Levy SL, Mannion JT, Cheng J, Reccius CH, & Craighead HG (2008) Entropic Unfolding of DNA Molecules in Nanofluidic Channels. *Nano Letters* 8(11):3839-3844.

63. Muthukumar M & Baumgärtner A (1989) Effects of Entropic Barriers on Polymer Dynamics. *Macromolecules* 22:1937-1941.

64. Nykypanchuk D, Strey HH, & Hoagland DA (2005) Single molecule visualizations of polymer partitioning within model pore geometries. *Macromolecules* 38(1):145-150.

65. Bennink ML*, et al.* (1999) Single-molecule manipulation of double-stranded DNA using optical tweezers: Interaction studies of DNA with RecA and YOYO-1. *Cytometry* 36(3):200-208.

66. Smith JPRaDE (2007) Single-Molecule Studies of DNA, Visualization and Manipulation of Individual DNA Molecules with Fluorescence Microscopy and Optical Tweezers. *Soft Matter: Scattering, Imaging and Manipulation*, ed Pecora RBaR (Springer), Vol 4.

67. Schnapp B. J. GJ, Sheetz M. P.   (1988) Nanometer-Scale Measurements Using
Video Light Microscopy. *Cell Motil Cytoskeleton* 10:47.

68. Woll EB, A. Deres, F. C. De Schryver, H. Uji-i, and J. Hofkens (2009) Polymers and single molecule fluorescence spectroscopy, what can we learn? *Chemical Society Reviews* 38:313.

69. S. R. Quake HB, and S. Chu (1997) The dynamics of partially extended single molecules of DNA. *Nature* 388:151.

70. P. Leduc CH, G. Bao, and D. Wirtz (1999) Dynamics of individual flexible polymers in a shear flow. *Nature* 399:564.

71. Winkler RG, Keller S, auml, & dler JO (2006) Intramolecular dynamics of linear macromolecules by fluorescence correlation spectroscopy. *Phys Rev E* 73(4):041919.

72. Petrov E, Ohrt T, Winkler R, & Schwille P (2006) Diffusion and Segmental Dynamics of Double-Stranded DNA. *Phys Rev Lett* 97(25).

73. Lisy V, Tothova J, & Zatovsky A (2006) The joint Rouse-Zimm theory of the dynamics of polymers in dilute solutions. *Condensed Matter Physics* 9:95.

74. Tothova BB, and V. Lisy (2007) Monomer dynamics in single- and double-stranded DNA coils. *The European Physical Journal E: Soft Matter and Biological Physics* 24(1):61.

75. Enderlein J (2012) Polymer Dynamics, Fluorescence Correlation Spectroscopy, and the Limits of Optical Resolution. *Phys Rev Lett* 108(10):108101.

76. Elson EL & Magde D (1974) Fluorescence Correlation Spectroscopy: 1. Conceptual Basis and Theory. *Biopolymers* 13(1):1-27.

77. Magde D, Elson EL, & Webb WW (1974) Fluorescence correlation spectroscopy. II. An experimental realization. *Biopolymers* 13(1):29-61.

78. Rigler R, Mets U, Widengren J, & Kask P (1993) Fluorescence Correlation Spectroscopy with High Count Rate and Low-Background - Analysis of Translational Diffusion. *European Biophysics Journal with Biophysics Letters* 22(3):169-175.

79. Schwille P, Korlach J, & Webb WW (1999) Fluorescence correlation spectroscopy with single-molecule sensitivity on cell and model membranes. *Cytometry* 36(3):176-182.

80. Taguchi H, Ueno T, Tadakuma H, Yoshida M, & Funatsu T (2001) Single-molecule observation of protein-protein interactions in the chaperonin system. *Nat Biotech* 19(9):861-865.

81. Schwille P, MeyerAlmes FJ, & Rigler R (1997) Dual-color fluorescence cross-correlation spectroscopy for multicomponent diffusional analysis in solution. *Biophysical Journal* 72(4):1878-1886.

82. S. Huang AAH, W. W. Webb (2002) Two-photon fluorescence spectroscopy and microscopy of NAD(P)H and flavoprotein. *Biophys. J.* 82:2811-2825.

83. J. Widengren PS (2000) Characterization of Photoinduced Isomerization and Back-Isomerization of the Cyanine Dye Cy5 by Fluorescence Correlation Spectroscopy. *J. Phys. Chem. A* (104):6416-6428.

84. Woll D (2014) Fluorescence correlation spectroscopy in polymer science. *RSC Advances* 4(5):2447-2465.

85. Sensor Technologies L (2008) FCS Theory Tutorials.

86. Schwille P (2001) Fluorescence correlation spectroscopy and its potential for intracellular applications. *Cell Biochem. Biophys.* 34(3):383-408.

87. Enderlein J, Gregor I, Patra D, Dertinger T, & Kaupp UB (2005) Performance of Fluorescence Correlation Spectroscopy for Measuring Diffusion and Concentration. *ChemPhysChem* 6(11):2324-2336.

88. Haustein E & Schwille P (2008) Fluorescence Correlation Spectroscopy. *Soft Matter Characterization*, eds Borsali R & Pecora R (Springer Netherlands), pp 637-675.

89. Bacia K & Schwille P (2007) Practical guidelines for dual-color fluorescence cross-correlation spectroscopy. *Nature Protocols* 2(11):2842-2856.

90. Volker Buschmann BKm, Felix Koberling, Rainer Macdonald, Steffen Rüttinger (2008) Application Note: Quantitative FCS: Determination of the Confocal Volume by FCS and Bead Scanning with the MicroTime 200. (PicoQuant GmbH).

91. Ruttinger S*, et al.* (2008) Comparison and accuracy of methods to determine the confocal volume for quantitative fluorescence correlation spectroscopy. *Journal of Microscopy* 232(2):343-352.

92. Koppel DE, Axelrod D, Schlessinger J, Elson EL, & Webb WW (1976) Dynamics of fluorescence marker concentration as a probe of mobility. *Biophysical Journal* 16(11):1315-1329.

93. Hess ST & Webb WW (2002) Focal Volume Optics and Experimental Artifacts in Confocal Fluorescence Correlation Spectroscopy. *Biophysical Journal* 83(4):2300-2317.

94. J. Enderlein IG, D. Patra, J. Fitter (2004) Art and Artefacts of Fluorescence Correlation Spectroscopy. *Curr Pharm Biotechno* 5:155-161.

95. Berland K & Shen G (2003) Excitation saturation in two-photon fluorescence correlation spectroscopy. *Applied Optics* 42(27):5566-5576.

96. Dertinger T*, et al.* (2007) Two-Focus Fluorescence Correlation Spectroscopy: A New Tool for Accurate and Absolute Diffusion Measurements. *ChemPhysChem* 8(3):433-443.

97. Haupts U, Maiti S, Schwille P, & Webb WW (1998) Dynamics of fluorescence fluctuations in green fluorescent protein observed by fluorescence correlation spectroscopy. *Proc. Natl. Acad. Sci. U.S.A.* 95(23):13573-13578.

98. Schwille P, Haupts U, Maiti S, & Webb WW (1999) Molecular dynamics in living cells observed by fluorescence correlation spectroscopy with one- and two-photon excitation. *Biophysical Journal* 77(4):2251-2265.

99. Krichevsky O & Bonnet G (2002) Fluorescence correlation spectroscopy: the technique and its applications. *Reports on Progress in Physics* 65(2):251-297.

100. Haustein E & Schwille P (2007) Fluorescence correlation spectroscopy: Novel variations of an established technique. *Annual Review of Biophysics and Biomolecular Structure* 36:151-169.

101. Buschmann V, Weston K, & Sauer M (2003) Spectroscopic study and evaluation of red-absorbing fluorescent dyes. *Bioconjugate Chem.* 14(1):195-204.

102. Sigma-Aldrich (Protocol for Annealing Oligonucleotides.

103. Newville M (2014) lmfit.

104. SciPy (2015) Numpy.

105. Foo Yong H, Naredi-Rainer N, Lamb Don C, Ahmed S, & Wohland T (2012) Factors Affecting the Quantification of Biomolecular Interactions by Fluorescence Cross-Correlation Spectroscopy. *Biophysical Journal* 102(5):1174-1183.

106. Weidemann T, Wachsmuth M, Tewes M, Rippe K, & Langowski Jr (2002) Analysis of Ligand Binding by Two-Colour Fluorescence Cross-Correlation Spectroscopy. *Single Mol.* 1.

107. Rippe K (2000) Simultaneous Binding of Two DNA Duplexes to the NtrC-Enhancer Complex Studied by Two-Color Fluorescence Cross-Correlation Spectroscopy. *Biochemistry* 39(9):2131-2139

108. Hinczewski M & Netz RR (2009) Global cross-over dynamics of single semiflexible polymers. *EPL (Europhysics Letters)* 88(1):18001.

109. Hinczewski M & Netz RR (2010) Dynamics of DNA: Experimental controversies and theoretical insights. *Physica A: Statistical Mechanics and its Applications* 389(15):2993-2996.

110. Krichevsky O (2013) Comment on "Polymer Dynamics, Fluorescence Correlation Spectroscopy, and the Limits of Optical Resolution". *Phys Rev Lett* 110(15):159801.

111. Oono Y & Kohmoto M (1983) Renormalization group theory of transport properties of polymer solutions. I. Dilute solutions. *The Journal of Chemical Physics* 78(1):520-528.

112. Pecora P (1991) DNA: A Model Compound for Solution Studies of Macromolecules. *Science* 251:893-898.

113. Sorlie SS & Pecora R (1990) A dynamic light scattering study of four DNA restriction fragments. *Macromolecules* 23(2):487-497.

114. H.-R. Rackwitz GZ, A.-M. Frischauf, and H. Lehrach (1984) Rapid restriction mapping of dna cloned in lambda phage vectors. *Gene* 30(1-3):195-200.

115. Takagi T, Kii H, & Kinjo M (2004) DNA measurements by using fluorescence correlation spectroscopy and two-color fluorescence cross correlation spectroscopy. *Curr Pharm Biotechno* 5(2):199-204.

116. Bernheim-Groswasser A, Shusterman R, & Krichevsky O (2006) Fluorescence correlation spectroscopy analysis of segmental dynamics in actin filaments. *J Chem Phys* 125(8):084903.

117. Wocjan T, Krieger J, Krichevsky O, & Langowski J (2009) Dynamics of a fluorophore attached to superhelical DNA: FCS experiments simulated by Brownian dynamics. *Phys Chem Chem Phys* 11(45):10671-10681.

118. Krieger JW, Singh AP, Garbe CS, Wohland T, & Langowski J (2014) Dual-color fluorescence cross-correlation spectroscopy on a single plane illumination microscope (SPIM-FCCS). *Opt Express* 22(3):2358-2375.

119. Jones JJ, van der Maarel JRC, & Doyle PS (2013) Intrachain Dynamics of Large dsDNA Confined to Slitlike Channels. *Phys Rev Lett* 110(6):068101.

120. Reisner W, Larsen NB, Flyvbjerg H, Tegenfeldt JO, & Kristensen A (2009) Directed self-organization of single DNA molecules in a nanoslit via embedded nanopit arrays. *Proceedings of the National Academy of Sciences* 106(1):79-84.

121. Yeh J-W, Taloni A, Chen Y-L, & Chou C-F (2012) Entropy-Driven Single Molecule Tug-of-War of DNA at Micro−Nanofluidic Interfaces. *Nano Letters* 12(3):1597-1602.

122. van Kan JA, Zhang C, Perumal Malar P, & van der Maarel JRC (2012) High throughput fabrication of disposable nanofluidic lab-on-chip devices for single molecule studies. *Biomicrofluidics* 6(3):036502.

123. Sanguigno L, De Santo I, Causa F, & Netti P (2010) A Closed Form for Fluorescence Correlation Spectroscopy Experiments in Submicrometer Structures. *Anal Chem*.

124. Milon S, Hovius R, Vogel H, & Wohland T (2003) Factors influencing fluorescence correlation spectroscopy measurements on membranes: simulations and experiments. *Chemical Physics* 288(2–3):171-186.

125. Mao P & Han J (2005) Fabrication and characterization of 20 nm planar nanofluidic channels by glass–glass and glass–silicon bonding. *Lab on a Chip* 5(8):837.

126. Kandlikar JLPaSG (2005) Review of fabrication of nanochannels for single phase liquid flow. *Microfluid. Nanofluid.* 2:185.

127. G. B. Salieb-Beugelaar JT, J. van Nieuwkasteele, D. Wijnperle, J. O. Tegenfeldt, F. Lisdat, A. van den Berg and J. C. T. Eijkel (2008) Field-Dependent DNA Mobility in 20 nm High Nanoslits. *Nano Lett.* 8:1785.

128. L. J. Guo XCaCFC (2004) Fabrication of Size-Controllable Nanofluidic Channels by Nanoimprinting and Its Application for DNA Stretching. *Nano Lett.* 4:69.

129. Q. Xia KJM, R. H. Austin and S. Y. Chou (2008) Sub-10 nm Self-Enclosed Self-Limited Nanofluidic Channel Arrays. *Nano Lett.* 8:3830.

130. Sriram KK, Chang CL, Rajesh Kumar U, & Chou CF (2014) DNA combing on low-pressure oxygen plasma modified polysilsesquioxane substrates for single-molecule studies. *Biomicrofluidics* 8(5):052102.

131. Gu J, Gupta R, Chou C-F, Wei Q, & Zenhausern F (2007) A simple polysilsesquioxane sealing of nanofluidic channels below 10 nm at room temperature. *Lab on a Chip* 7(9):1198-1201.

132. D. C. Duffy JCM, O. J. A. Schueller and G. M. Whitesides (1998) Rapid Prototyping of Microfluidic Systems in Poly(dimethylsiloxane). *Anal. Chem.* 70:4974.

133. S. Bhattacharya AD, J. M. Berg and S. Gangopadhyay (2005) Studies on surface wettability of poly(dimethyl) siloxane (PDMS) and glass under oxygen-plasma treatment and correlation with bond strength. *J Microelectromech S* 14:590.

134. Lesser-Rojas L*, et al.* (2014) Tandem array of nanoelectronic readers embedded coplanar to a fluidic nanochannel for correlated single biopolymer analysis. *Biomicrofluidics* 8(1):016501.

135. Leichlé T*, et al.* (2012) Biosensor-compatible encapsulation for pre-functionalized nanofluidic channels using asymmetric plasma treatment. *Sensors and Actuators B: Chemical* 161(1):805-810.

136. Liao K-T & Chou C-F (2012) Nanoscale Molecular Traps and Dams for Ultrafast Protein Enrichment in High-Conductivity Buffers. *J Am Chem Soc* 134(21):8742-8745.

137. Petrášek Z & Schwille P (2008) Precise Measurement of Diffusion Coefficients using Scanning Fluorescence Correlation Spectroscopy. *Biophysical Journal* 94(4):1437-1448.

138. Loman A. MCB, Koberling F., Richtering W., Enderlein J. (2008) Absolute and Precise Measurements of the Diffusion of Small Fluorescent Dye Molecules Across the Visible Spectrum. *14th International Workshop on Single Molecule Spectroscopy and Ultrasensitive Analysis in Life Sciences*.

APPENDIX

I. Part Listing

The following section lists the critical optical components comprising the homebuilt 2-color FCCS device. The part number is provided along with the spectra of the optics where appropriate. All optics were held together using standard Thorlabs posts, bases, clamps, and rail systems.

A. Excitation Pathway

1. Coherent Sapphire SF 488nm 20mW Laser
2. Thorlabs HeNe 633nm 5mW Laser, HNL050L
3. Ø1" Zero-Order Half-Wave Plate, SM1-Threaded Mount, 488 nm
   a. Cube-Mounted Polarizing Beamsplitter, 420 - 680 nm, CM1-PBS251
4. Ø1" Zero-Order Half-Wave Plate, SM1-Threaded Mount, 633 nm
   a. Cube-Mounted Polarizing Beamsplitter, 420 - 680 nm, CM1-PBS251
5. Ø1" (Ø25.4 mm) Protected Silver Mirror, 0.24" (6.0 mm) Thick, PF10-03-P01
6. Semrock 580 nm edge BrightLine® single-edge imaging-flat dichroic beamsplitter, FF580-FDi01-25x36
7. Fiber Launch system, Thorlabs KT110
   a. C230 TME-A lens, Thorlabs, $f = 4.51mm$

b. S405 XP Single mode optical fiber, Thorlabs
8. Fiber Launch system, Thorlabs KT110
a. TRH127-020-A-ML - Ø1/2" Achromatic Triplet, SM05-Threaded Mount, f = 20 mm, ARC: 400 - 700 nm
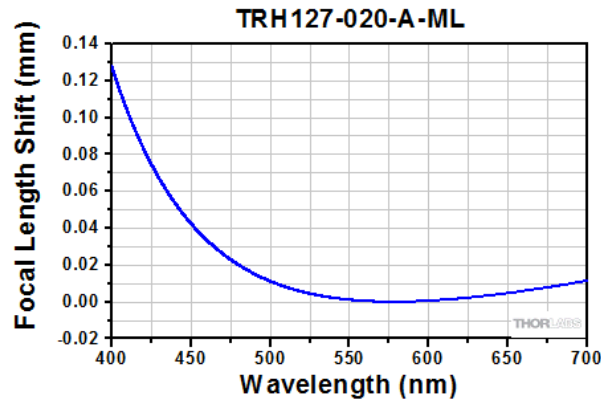
9. Semrock Dichroic Beamsplitter 500/646, FF500/646-Di01
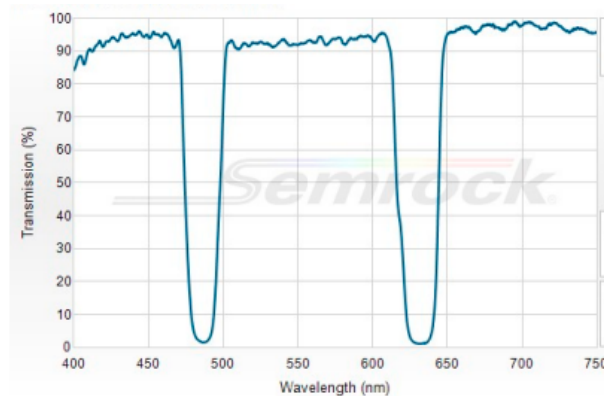
10. Zeiss C-Apochromat 63x 1.2 NA Water Objective

B. Emission Pathway

11. Ø1" (Ø25.4 mm) Protected Silver Mirror, 0.24" (6.0 mm) Thick, PF10-03-P01
12. Semrock 580 nm edge BrightLine® single-edge imaging-flat dichroic beamsplitter, FF580-FDi01-25x36
13. Ø1" (Ø25.4 mm) Protected Silver Mirror, 0.24" (6.0 mm) Thick, PF10-03-P01
14. Fiber Launch system, Thorlabs KT110
a. AC254-125-A-ML, f=125 mm, Ø1" Achromatic Doublet, SM1-Threaded Mount, ARC: 400-700 nm, Thorlabs
b. Semrock 520/44 nm BrightLine® single-band bandpass filter FF01-520/44-25
c. CT1 Cage Translation Stage, ½" Z-Axis Travel
15. Fiber Launch system, Thorlabs KT110
d. AC254-100-A-ML , f=100 mm, Ø1" Achromatic Doublet, SM1-Threaded Mount, ARC: 400-700 nm, Thorlabs
e. Semrock 661/20 nm BrightLine® single-band bandpass filter FF01-661/20-25
f. CT1 Cage Translation Stage, ½" Z-Axis Travel
16. Multimode Fiber

a. Ø25 μm, 0.10 NA, FC/PC-FC/PC Fiber Patch Cable, 1 m M67L01, Thorlabs
    b. Ø50 μm, 0.22 NA, FC/PC-FC/PC Fiber Patch Cable, 1 m M42L01, Thorlabs
17. 1x2 MM Coupler, 50/50 Split Ratio, 50 μm GI Fibers, FC/PC, FCMM50-50A-FC, Thorlabs
18. Perkin Elmer SPCM-AQR-14 Avalanche Photodiode
19. 50Ω coaxial cable
20. Correlator.com Flex03LQ-01 Digital Correlator

II.   Alignment of Fluorescence Cross-Correlations Optics

Note: Some steps and illustrations adapted from Stanford University Chem 184 lab protocol, Detection of Fluorescence from Single Molecules
http://www.stanford.edu/class/chem184/manual/LabProtocols2.pdf

1. Both lasers should be turned on for at least 1 hour prior to testing in order to stabilize the power output and temperature of the system.
2. Utilizing a power meter, verify independently that the each laser channel has a power of ~5mW prior to entering the first fiber coupler.
3. Test the power of each channel after the SM fiber coupler / triplet lens. It is important to maximize the power more for the Red channel than the Blue, given the additional power available in the blue channel. All of the following adjustments are made at the first collimator prior to the laser entering the first optical fiber. Typical power expected after the SM fiber should be about ~3mW in the Red channel and ~2mW in the Blue channel, assuming an input of ~5mW.
4. After maximum power is achieved through the first single mode fiber, adjustment of the second (triplet lens) collimator must be made. The beam first must be centered along the triplet lens. Place two alignment plates along rails in front of the triplet lens followed by a variable aperture. The use of a variable iris aperture is also useful for this section, in place of or in combination with the alignment plates. Either way, one should be within an inch or two of the lens, while the other as far away from the lens as possible using the rails. Use the X/Y adjusters of collimator to make sure the beam passes through as straight as possible. Power can also be measured at the lens and compared to after the second plate to see if it is maximal with minimal loss.
5. The collimation of the beam will now be checked. The size of the beam is measured at various points: 1) in front of the collimator 2) after mirror 1 3) after mirror 2 4) transmission through dichroic against back wall. Z adjustment of collimator was made until agreement on size of the beam could be found to within 4.8mm +-0.2mm. No positioning of the triplet lens in z could result in perfect collimation. There is always a larger beam immediately coming from the fiber straight out of collimator.
6. Additional checks of the collimation are made by re-routing the beam using an additional mirror after mirror 1 in the setup to check the collimation at distant points – in this case 2m and 4m to verify that the beam remains collimated over long distances.
7. The straightness of the excitation pathway should be verified through the objective / rail tower. The 63x objective is removed – in order to visualize if the beam is truly passing through the center of the objective column – to eliminate partial clipping of the beam as it enters the objective. Construct a rail tower straight up from the objective with two

variable shutters – one on top and one midway. Optionally, alignment plates can be taped to the bottom of the shutters to assist in visualizing the centering. Similar to centering the beams for coupling to the fiber, use the two mirrors to center the beam along the tower, using the variable apertures as markers as tests to see if the beam is clipped in any direction, as shown below. Note that only the mirrors should be adjusted at this point, NOT the X/Y adjusters of the collimator.

Top-left clipped   Unclipped circle   Bottom-right clipped
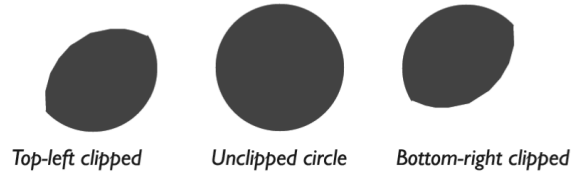
8. Next the 63x objective can be replaced and the rail tower constructed above the objective in the previous step removed.
9. Place a silver mirror on top of a coverslip on top of the 63x objective.
10. Place a reflected beam card (an index card wrapped in black tape with a punch hole works well) in front of the collimator while checking that the power after the punch card is maximal.
11. Adjust the focus of the objective so that the alignment mirror is exactly one focal length away. At this position, the excitation beam passing through the objective and the reflected beam are the same size. As shown in the following figures, it's important to check that the reflected beam follows the same pathway as the excitation beam, ensuring that the beam is passing through the center of and perpendicular to the objective.
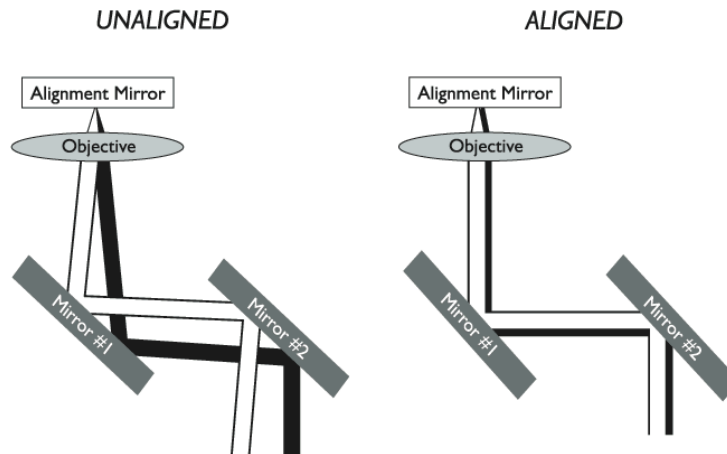
12. Adjust the first the two mirrors after the collimator by observing that the reflected beam is centered along the punch hole. Focus any adjustments to just one mirror, preferably mirror 1. Ideally, if the previous steps were performed correctly, minimal adjustment should be necessary. One can move the mirror in and out of focus so as to verify that the two reflected spots expand and contract symmetrically. If correction with the mirros is insufficient, it may be necessary to adjust the dichroic mirror. Ensure that the incoming and reflected beams completely overlap. Be careful to observe that the beam is not being clipped at any point of its transmission.
13. With an alignment mirror still on top of the objective, increase the power of both laser lines until the reflected beam can be seen transmitted into the emission pathway. Adjust

the position of the alignment mirror until it is one focal length away from the objective.

14. The reflected beam will be used to coarsely adjust the emission pathways for both channels. The procedure is identical for both the blue and red channels.

15. Follow the beam through the second dichroic and verify that the beam is not being clipped along the two-mirror pathway to the emission collimator. Position the mirrors such that the beam is centered on them and roughly entering the collimator.

16. Remove any lens from the emission collimator. It is absolutely critical that the beam is centered perfectly on the input of the fiber before the doublet lens is in place. Using two alignment plates, one before the collimator and one after, placed as close to the emission fiber, adjust the two mirrors until the reflected beam passes perpendicular to both alignment plates without being clipped. This ensures that the emission pathway is completely straight.

17. Once sufficient adjustment with the alignment plates is done, replace the focusing lens. Keeping the second alignment plate close to the fiber, verify that the focused beam is centered on the fiber input. Adjust the X/Y micrometers of the collimator until beam is centered.

18. Following adjustment, prepare a diluted sample of Alexa 488 / Atto 633. Generally, samples between 1-5nM work best.

19. Adjust the sample position until you are 50um within the sample. To do this, place the reflected beam card underneath the dichroic. As the sample is lowered onto the objective, two reflections points will be seen on the card, approximately 150-170um apart. This corresponds to the bottom and top of the coverslip. Once the first reflection point is reached using the coarse adjustment, use the fine micrometer to find the second reflection point.

20. Adjust the microscope objective collar as necessary from the thickness obtained from the fine micrometer between the two reflection points.

21. Turn on the APDs and measure the count rate utilizing the correlator software. Finely adjust the X/Y micrometers of the emission collimators until the count rate is maximized. The setup should now be fully aligned in the X and Y directions only.

22. After any alignment, it is important to perform a full sweep along the z-axis of the fiber coupler leading into the APD to determine the optimal position. Any adjustment of the fiber coupler along the z-axis requires fine-tuning in the X/Y directions again.

III.   Fluorophore Diffusion Coefficients

Fluorophore	MW g/mol	λ_{em} nm	QY	ε (M^{-1}cm^{-1})	Diffusion Coeff at 25C (298.15 K) / 10^{-6} cm^{2}s^{-1}	Methods / Ref
Alexa 488 SE	643	519	0.92	71,000	4.35 ± 0.05	Petrasek et. al[137]
Alexa 633 SE	~1200	647	-	100,000	3.4 ± 0.1	2fFCS[138]
Atto 488 Carboxylic acid	804	523	0.8	90,000	4.0 ± 0.1	2fFCS[90]
Atto 633 Carboxylic acid	652	657	0.64	130,000	4.16	Calculated using relation of $M^{\frac{1}{3}}$

IV. Temperature Dependence of Diffusion Coefficients

$$D = \frac{kT}{6\pi\eta(T)R_h} \qquad \eta(T) = Temp\ Dependent$$

$$D(T) = D(@25C) * \frac{T}{298.15K} * \frac{8.9 * 10^{-4}Pa * s}{\eta(T)}$$

$$= D(@25C) * \frac{t + 273.15}{\eta(T)} * 2.985 * 10^{-6}Pa * s * K^{-1}$$
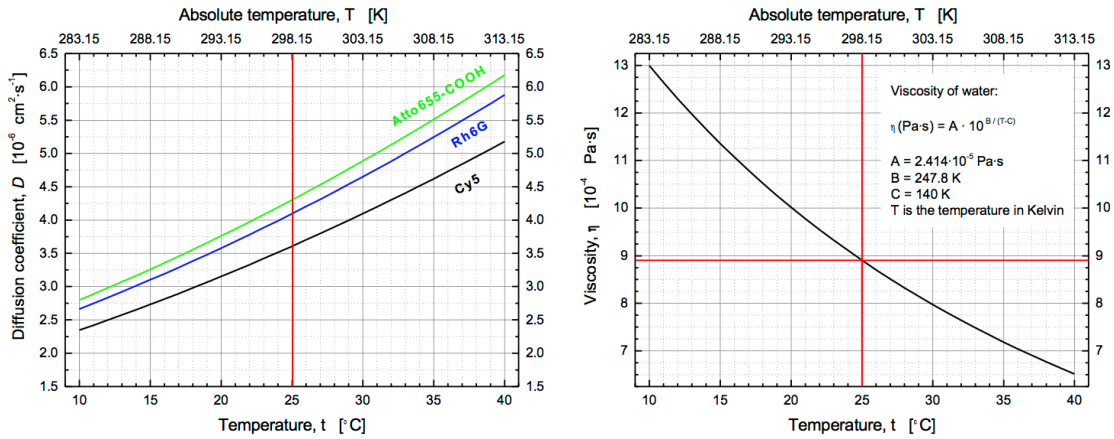
Figure adapted from Picoquant Application Note[90]

V. Errors in Pipetting

9.2.2 Eppendorf Research adjustable-volume

Volume	Systematic error (inaccuracy)	Random error (imprecision)
0.1 – 2.5 µl (dark gray)		
0.25 µl	±12.0 %	≤6.0 %
1.25 µl	±2.5 %	≤1.5 %
2.5 µl	±1.4 %	≤0.7 %
0.5 – 10 µl (light gray)		
1 µl	±2.5 %	≤1.8 %
5 µl	±1.5 %	≤ 0.8 %
10 µl	±1.0 %	≤0.4 %
2 – 20 µl (yellow)		
2 µl	±5.0 %	≤1.5 %
10 µl	±1.2 %	≤0.6 %
20 µl	±1.0 %	≤0.3 %
10 – 100 µl (yellow)		
10 µl	±3.0%	≤1.0 %
50 µl	±1.0 %	≤ 0.3 %
100 µl	±0.8 %	≤0.2 %
20 – 200 µl (yellow)		
20 µl	±2.5%	≤0.7 %
100 µl	±1.0 %	≤0.3 %
200 µl	±0.6 %	≤0.2 %
100 – 1,000 µl (blue)		
100 µl	±3.0 %	≤0.6 %
500 µl	±1.0 %	≤0.2 %
1,000 µl	±0.6 %	≤0.2 %

VI. Implementation of Gaussian and Numerical (Gaussian Beam) Fitting Models

Fitting follows the following procedure:
1) g_noexp is equivalent to the following component of $g(t,0)$ from above,

$$\sqrt{\pi}\int_0^\infty d\xi \int_0^\infty d\eta \left(\frac{\kappa\left(\eta-\sqrt{Dt}\xi\right)\kappa\left(\eta+\sqrt{Dt}\xi\right)}{8Dt+w^2\left(\eta-\sqrt{Dt}\xi\right)+w^2\left(\eta+\sqrt{Dt}\xi\right)}\right)$$

2) This is integrated twice, first in $gz1\_hermite$ and then in $g\_hermite$
3) In the fitting function itself, $g\_hermite$ is normalized by dividing by the concentration and $vol1^2$

Concentration is introduced into the fitting functions in nanoMolar concentration and multiplied by a factor as indicated below.

$$C = \frac{N}{VN_A} \quad V[um^3], N_A = 6.022*10^{23}\ [mol^{-1}]$$

$$10^{-15}[um^3]*6.022*10^{23}[\,mol^{-1}] = 6.022*10^8 \rightarrow C[nM]*6.022*10^8$$

lmfit Models for fitting FCS correlation function

modelFCS : 3-d Gaussian FCS model with parameters wx, wz, D diffusion coefficient, C concentration (all units are micrometer, seconds)

modelFCS_t: same as modelFCS with additional triplet contribution. Additional parameters F triplet fraction, tf relaxation time

modelFCS_n: FCS fit function for more a realistic confocal detection function (Gaussian in x,y but not in z). Has to be evaluated numerically.
Parameters: a pinhole radius, lambdaex, lambdaem, n index of refraction of immersion liquid, w0 width in x-y, D, C

modelFCS_nt: same as modelFCS but with triplet contribution

```
"""
import numpy as np
import math as m
from lmfit import Model
from scipy.integrate import quad

##############################################################################
# 3-d Gaussian models
##############################################################################

# 3-d Gaussian focus FCS model with triplet correction
def g_FCS(t,C,wxy,wz,D,F,tf):
    v=wxy*wxy*wz*m.pi**1.5
    N=C*6.022e-1*v
    triplet=(1-F+F*np.exp(-t/tf))/(1-F)
```

```python
    return 1.0+triplet/N/(1+4*D*t/wxy/wxy)/np.sqrt(1+4*D*t/wz/wz)

# 3-d Gaussian focus FCS model
def g(t,C,wxy,wz,D):
    v=wxy*wxy*wz*m.pi**1.5
    N=C*6.022e-1*v
    return 1.0+1.0/N/(1+4*D*t/wxy/wxy)/np.sqrt(1+4*D*t/wz/wz)

# 3-d Gaussian focus FCS model with triplet correction
def g_t(t,C,wxy,wz,D,F,tf):
    v=wxy*wxy*wz*m.pi**1.5
    N=C*6.022e-1*v
    triplet=(1-F+F*np.exp(-t/tf))/(1-F)
    return 1.0+triplet/N/(1+4*D*t/wxy/wxy)/np.sqrt(1+4*D*t/wz/wz)

modelFCS_t = Model(g_t,independent_vars=['t'])
modelFCS = Model(g,independent_vars=['t'])

# model for standard deviation
# empirically p=0.33
def noise(t,tc,a,b,p):
    x=t/tc
    return np.abs(a)/x+np.abs(b)/x**p

modelNoise=Model(noise,independent_vars=['t'])

###########################################################################
# Numerical models
###########################################################################
#constants
maxz=200 # z integration range in microns

# determine hermite-gaussian integration intervals
xh,yh=np.polynomial.hermite.hermgauss(50)

def w2(z,w0,lambdaex,n):
    return w0*w0+(lambdaex*z/m.pi/w0/n)**2

def k(z,a,r0,lambdaem,n):
    return 1-np.exp(-2*a*a/(r0*r0+(lambdaem*z/m.pi/r0/n)**2))

#def gi(eta,xi,t,D,w0,a,R0,lambdaex,lambdaem,n):
#    return np.exp(-xi**2)*k(eta-
np.sqrt(D*t)*xi,a,R0,lambdaem,n)*k(eta+np.sqrt(D*t)*xi,a,R0,lambdaem,n)/(8*D*t+w2(eta-
np.sqrt(D*t)*xi,w0,lambdaex,n)+w2(eta+np.sqrt(D*t)*xi,w0,lambdaex,n))
```

```python
def g_noexp(eta,xi,t,D,w0,a,R0,lambdaex,lambdaem,n):
    return m.sqrt(m.pi)*k(eta-
np.sqrt(D*t)*xi,a,R0,lambdaem,n)*k(eta+np.sqrt(D*t)*xi,a,R0,lambdaem,n)/(8*D*t+w2(eta-
np.sqrt(D*t)*xi,w0,lambdaex,n)+w2(eta+np.sqrt(D*t)*xi,w0,lambdaex,n))

def gz1_hermite(xi,t,D,w0,a,R0,lambdaex,lambdaem,n):
    return np.sum(g_noexp(xi,xh,t,D,w0,a,R0,lambdaex,lambdaem,n)*yh)

def g_hermite(t,D,w0,a,R0,lambdaex,lambdaem,n):
    return quad(gz1_hermite,0,maxz,args=(t,D,w0,a,R0,lambdaex,lambdaem,n))

#def gz1(xi,t,D,w0,a,R0,lambdaex,lambdaem,n):
#    return quad(gi,0,200+np.sqrt(D*t)*xi,args=(xi,t,D,w0,a,R0,lambdaex,lambdaem,n))[0]

#def g(t,D,w0,a,R0,lambdaex,lambdaem,n):
#    return quad(gz1,0,200,args=(t,D,w0,a,R0,lambdaex,lambdaem,n))

def g0(z,w0,a,R0,lambdaex,lambdaem,n):
    return k(z,a,R0,lambdaem,n)**2/w2(z,w0,lambdaex,n)

# vol1 is integral over k(z) and the square normalizes the function g_hermite
# g(t)=g_hermite/vol1**2
def vol1(a,r0,lambdaem,n,C=None,D=None,lambdaex=None,w0=None,F=None,tf=None):
    return quad(k,0,maxz,args=(a,r0,lambdaem,n))[0]*m.pi

def vol2(w0,a,r0,lambdaex,lambdaem,n,C=None,D=None,F=None,tf=None):
    return m.pi/2.0*quad(g0,0,maxz,args=(w0,a,r0,lambdaex,lambdaem,n))[0]

def vol1dict(b):
    n = b['n'].value
    a=b['a'].value
    r0=b['r0'].value
    lambdaem=b['lambdaem'].value

    return quad(k,0,maxz,args=(a,r0,lambdaem,n))[0]*m.pi

def vol2dict(b):
    w0=b['w0'].value
    n = b['n'].value
    a=b['a'].value
    r0=b['r0'].value
    lambdaem=b['lambdaem'].value
    lambdaex=b['lambdaex'].value
    return m.pi/2.0*quad(g0,0,maxz,args=(w0,a,r0,lambdaex,lambdaem,n))[0]

def g_n(t,D,C,w0,a,r0,lambdaex,lambdaem,n):
```

```python
    v1=vol1(a,r0,lambdaem,n)
    v2=vol2(w0,a,r0,lambdaex,lambdaem,n)

    print "w0 = ",w0,"R0 = ",r0,"c = ",C,"vol",v1*v1/v2

    return np.array([1+g_hermite(tt,D,w0,a,r0,lambdaex,lambdaem,n)[0]/C/6.022e-1/v1/v1 for tt
in t])

def g_nt(t,D,C,w0,a,r0,lambdaex,lambdaem,n,F,tf):
    v1=vol1(a,r0,lambdaem,n)
    v2=vol2(w0,a,r0,lambdaex,lambdaem,n)

    print "w0 = ",w0,"R0 = ",r0,"c = ",C,"vol",v1*v1/v2, "F",F,"tf",tf

    return np.array([1+(1-F+F*np.exp(-tt/tf))/(1-
F)*g_hermite(tt,D,w0,a,r0,lambdaex,lambdaem,n)[0]/C/6.022e-1/v1/v1 for tt in t])

modelFCS_n = Model(g_n,independent_vars=['t'])
modelFCS_nt = Model(g_nt,independent_vars=['t'])


############################################################################
# Combined fit dilutions residual functions
############################################################################

def g_all(b,t,c,data=None,sigma=None):
    #C=b['C'].value
    corr_g=None
    D=b['D'].value
    wxy=b['wxy'].value
    wz=b['wz'].value
    for i,conc in enumerate(c):
        C=b[conc].value
        v=wxy*wxy*wz*m.pi**1.5
        N=C*6.022e-1*v
        g=1+1/N/(1+4*D*t/wxy/wxy)/np.sqrt(1+4*D*t/wz/wz)
        if corr_g is None:
            corr_g=g
        else:
            corr_g=np.vstack((corr_g,g))

    print "wxy = ", wxy
    print "wz = ", wz
    print "SP = ", wz/wxy

    if data is None:
        return corr_g
```

```
    corr_res=(corr_g-data)/sigma
    return corr_res.flatten()


def g_all_t(b,t,c,data=None,sigma=None):
    #C=b['C'].value
    corr_g=None
    D=b['D'].value
    wxy=b['wxy'].value
    wz=b['wz'].value
    F=b['F'].value
    tf=b['tf'].value
    for i,conc in enumerate(c):
        C=b[conc].value
        v=wxy*wxy*wz*m.pi**1.5
        N=C*6.022e-1*v
        g=1+(1-F+F*np.exp(-t/tf))/(1-F)/N/(1+4*D*t/wxy/wxy)/np.sqrt(1+4*D*t/wz/wz)
        if corr_g is None:
            corr_g=g
        else:
            corr_g=np.vstack((corr_g,g))

    print "wxy = ", wxy
    print "wz = ", wz
    print "SP = ", wz/wxy

    if data is None:
        return corr_g
    corr_res=(corr_g-data)/sigma
    return corr_res.flatten()

def g_all_n(b,t,c,data=None,sigma=None):
    corr_g=None
    D=b['D'].value
    w0=b['w0'].value
    n = b['n'].value
    a=b['a'].value
    r0=b['r0'].value
    lambdaex=b['lambdaex'].value
    lambdaem=b['lambdaem'].value

    for i,conc in enumerate(c):
        C=6.022e-1*b[conc].value

        v1=vol1(a,r0,lambdaem,n)
        v2=vol2(w0,a,r0,lambdaex,lambdaem,n)
```

```python
        print "w0 = ",w0,"R0 = ",r0,"c = ",C,"vol",v1*v1/v2

        g=[1+g_hermite(tt,D,w0,a,r0,lambdaex,lambdaem,n)[0]/C/v1/v1 for tt in t]
        if corr_g is None:
            corr_g=g
        else:
            corr_g=np.vstack((corr_g,g))

    if data is None:
        return corr_g
    corr_res=(corr_g-data)/sigma
    return corr_res.flatten()


def g_all_nt(b,t,c,data=None,sigma=None):
    corr_g=None
    D=b['D'].value
    w0=b['w0'].value
    n = b['n'].value
    a=b['a'].value
    r0=b['r0'].value
    lambdaex=b['lambdaex'].value
    lambdaem=b['lambdaem'].value
    F=b['F'].value
    tf=b['tf'].value

    for i,conc in enumerate(c):
        C=6.022e-1*b[conc].value

        v1=vol1(a,r0,lambdaem,n)
        v2=vol2(w0,a,r0,lambdaex,lambdaem,n)

        print "w0 = ",w0,"R0 = ",r0,"c = ",C,"vol",v1*v1/v2

        g=[1+(1-F+F*np.exp(-tt/tf))/(1-
F)*g_hermite(tt,D,w0,a,r0,lambdaex,lambdaem,n)[0]/C/v1/v1 for tt in t]
        if corr_g is None:
            corr_g=g
        else:
            corr_g=np.vstack((corr_g,g))

    if data is None:
        return corr_g
    corr_res=(corr_g-data)/sigma
    return corr_res.flatten()


#############################################################################
```

```
# Combined fit oligo functions
##########################################################################

def g_oligo_all(b,t,data=None,sigma=None):
    D=b['D'].value
    wxy_b=b['wxy_b'].value
    wz_b=b['wz_b'].value
    wxy_r=b['wxy_r'].value
    wz_r=b['wz_r'].value
    delta_z=b['delta_z'].value
    C=b['C'].value
    F_b=b['F_b'].value
    F_r=b['F_r'].value
    tf_b=b['tf_b'].value
    tf_r=b['tf_r'].value

    vb=wxy_b*wxy_b*wz_b*m.pi**1.5
    N=6.022e-1*C*vb
    g=1.0+(1-F_b+F_b*np.exp(-t/tf_b))/(1-
F_b)/N/(1+4*D*t/wxy_b/wxy_b)/np.sqrt(1+4*D*t/wz_b/wz_b)
    corr_g=g[:]

    vr=wxy_r*wxy_r*wz_r*m.pi**1.5
    N=6.022e-1*C*vr
    g=1.0+(1-F_r+F_r*np.exp(-t/tf_r))/(1-
F_r)/N/(1+4*D*t/wxy_r/wxy_r)/np.sqrt(1+4*D*t/wz_r/wz_r)
    corr_g=np.vstack((corr_g,g[:]))

    wxysq=wxy_r*wxy_r+wxy_b*wxy_b
    wzsq=wz_r*wz_r+wz_b*wz_b

vcorr=2*wxy_b*wxy_b*wxy_r*wxy_r/wxysq*np.sqrt(2*wz_b*wz_b*wz_r*wz_r/wzsq)*m.pi*
*1.5
    N=6.022e-1*C*vcorr
    g=1+1/N/(1+8*D*t/wxysq)/np.sqrt(1+8*D*t/wzsq)*np.exp(-delta_z*delta_z/(8*D*t+wzsq))
    corr_g=np.vstack((corr_g,g))

    print "C=",C," D= ",D," dz= ",delta_z," V_blue= ",vb," V_red= ",vr, "V_cross=",vcorr

    if data is None:
        return corr_g
    corr_res=(corr_g-data)/sigma
    return corr_res.flatten()
```

functions describing crosscorrelation functions that are derived from U1(z1)*exp(-(z2-
z1)^2/s^2)*U2(z2)

```python
def
gc_noexp(eta,xi,t,D,w11,w22,a1,a2,R1,R2,lambdaex1,lambdaem1,lambdaex2,lambdaem2,n,dz):
    return m.sqrt(m.pi)*k(eta-
np.sqrt(D*t)*xi+dz,a1,R1,lambdaem1,n)*k(eta+np.sqrt(D*t)*xi,a2,R2,lambdaem2,n)/(8*D*t+w
2(eta-np.sqrt(D*t)*xi+dz,w11,lambdaex1,n)+w2(eta+np.sqrt(D*t)*xi,w22,lambdaex2,n))

def
gcz1_hermite(eta,t,D,w1,w2,a1,a2,R1,R2,lambdaex1,lambdaem1,lambdaex2,lambdaem2,n,dz):
    return
np.sum(gc_noexp(eta,xh,t,D,w1,w2,a1,a2,R1,R2,lambdaex1,lambdaem1,lambdaex2,lambdaem2,
n,dz)*yh)

def gc_hermite(t,D,w1,w2,a1,a2,R1,R2,lambdaex1,lambdaem1,lambdaex2,lambdaem2,n,dz):
    return quad(gcz1_hermite,-
maxz,maxz,args=(t,D,w1,w2,a1,a2,R1,R2,lambdaex1,lambdaem1,lambdaex2,lambdaem2,n,dz))

def g0c(z,w11,w22,a1,a2,R1,R2,lambdaex1,lambdaem1,lambdaex2,lambdaem2,n,dz):
    return
k(z+dz,a1,R1,lambdaem1,n)*k(z,a2,R2,lambdaem2,n)/np.sqrt(w2(z+dz,w11,lambdaex1,n))/np.s
qrt(w2(z,w22,lambdaex2,n))

def vol2c(w1,w2,a1,a2,R1,R2,lambdaex1,lambdaem1,lambdaex2,lambdaem2,n,dz):
    return np.pi/4.0*quad(g0c,-
maxz,maxz,args=(w1,w2,a1,a2,R1,R2,lambdaex1,lambdaem1,lambdaex2,lambdaem2,n,dz))[0]

#Numerical Model Fitting Blue / Red / Cross Together
def g_oligo_all_n(b,t,data=None,sigma=None):

    wxy_b = b['w0_b'].value
    wxy_r = b['w0_r'].value
    lambdaex_b=b['lambdaex_b'].value
    lambdaem_b=b['lambdaem_b'].value
    lambdaex_r=b['lambdaex_r'].value
    lambdaem_r=b['lambdaem_r'].value
    a_b=b['a_b'].value
    a_r=b['a_r'].value
    r0_b=b['r0_b'].value
    r0_r=b['r0_r'].value
    D = b['D'].value
    n = b['n'].value
    C = 6.022e-1*b['C'].value
    dz=b['delta_z'].value

    #blue correlation
    v1=vol1(a_b,r0_b,lambdaem_b,n)
```

```
    v2=vol2(wxy_b,a_b,r0_b,lambdaex_b,lambdaem_b,n)
    vb=v1*v1/v2

    g=[1+g_hermite(tt,D,wxy_b,a_b,r0_b,lambdaex_b,lambdaem_b,n)[0]/C/v1/v1 for tt in t]
#    gDb=np.array(gDb)
    corr_g=g[:]

    #red correlation
    v1=vol1(a_r,r0_r,lambdaem_r,n)
    v2=vol2(wxy_r,a_r,r0_r,lambdaex_r,lambdaem_r,n)
    vr=v1*v1/v2

    g=[1.0+g_hermite(tt,D,wxy_r,a_r,r0_r,lambdaex_r,lambdaem_r,n)[0]/C/v1/v1 for tt in t]
#    gDr =np.array(gDr)
    corr_g=np.vstack((corr_g,g[:]))

    #cross correlation
    v1=vol1(a_b,r0_b,lambdaem_b,n)
    v2=vol1(a_r,r0_r,lambdaem_r,n)
    g=[1.0+gc_hermite(tt, D, wxy_b, wxy_r, a_b, a_r, r0_b, r0_r,
lambdaex_b,lambdaem_b,lambdaex_r,lambdaem_r,n,dz)[0]/C/v1/v2/2.0 for tt in t]
#    gDc=np.array(gDc)
    corr_g=np.vstack((corr_g,g))

    print "C=",C/(6.022e-1)," D= ",D," dz= ",dz," V_blue= ",vb," V_red= ",vr,
'wxb=',wxy_b,'wxr=',wxy_r

    if data is None:
        return corr_g
    corr_res=(corr_g-data)/sigma
    return corr_res.flatten()

#Numerical Model Fitting Blue / Red / Cross Together
def g_oligo_all_nc(b,t,data=None,sigma=None):

    wxy_b = b['w0_b'].value
    wxy_r = b['w0_r'].value
    lambdaex_b=b['lambdaex_b'].value
    lambdaem_b=b['lambdaem_b'].value
    lambdaex_r=b['lambdaex_r'].value
    lambdaem_r=b['lambdaem_r'].value
    a_b=b['a_b'].value
    a_r=b['a_r'].value
    r0_b=b['r0_b'].value
    r0_r=b['r0_r'].value
    D = b['D'].value
```

```python
    n = b['n'].value
    Cb = 6.022e-1*b['Cb'].value
    Cr = 6.022e-1*b['Cr'].value
    Cc = 6.022e-1*b['Cc'].value
    dz=b['delta_z'].value

    #blue correlation
    v1=vol1(a_b,r0_b,lambdaem_b,n)
    v2=vol2(wxy_b,a_b,r0_b,lambdaex_b,lambdaem_b,n)
    vb=v1*v1/v2

    g=[1+g_hermite(tt,D,wxy_b,a_b,r0_b,lambdaex_b,lambdaem_b,n)[0]/Cb/v1/v1 for tt in t]
#    gDb=np.array(gDb)
    corr_g=g[:]

    #red correlation
    v1=vol1(a_r,r0_r,lambdaem_r,n)
    v2=vol2(wxy_r,a_r,r0_r,lambdaex_r,lambdaem_r,n)
    vr=v1*v1/v2

    g=[1.0+g_hermite(tt,D,wxy_r,a_r,r0_r,lambdaex_r,lambdaem_r,n)[0]/Cr/v1/v1 for tt in t]
#    gDr =np.array(gDr)
    corr_g=np.vstack((corr_g,g[:]))

    #cross correlation
    v1=vol1(a_b,r0_b,lambdaem_b,n)
    v2=vol1(a_r,r0_r,lambdaem_r,n)
    g=[1.0+gc_hermite(tt, D, wxy_b, wxy_r, a_b, a_r, r0_b, r0_r,
lambdaex_b,lambdaem_b,lambdaex_r,lambdaem_r,n,dz)[0]/Cc/v1/v2/2.0 for tt in t]
#    gDc=np.array(gDc)
    corr_g=np.vstack((corr_g,g))

    print "Cb=",Cb/(6.022e-1),"Cr=",Cr/(6.022e-1),"Cc=",Cc/(6.022e-1)," D= ",D," dz= ",dz,"
V_blue= ",vb," V_red= ",vr, 'wxb=',wxy_b,'wxr=',wxy_r

    if data is None:
        return corr_g
    corr_res=(corr_g-data)/sigma
    return corr_res.flatten()

#function describing polymer dynamics with one color attached
def kp(v,t,Rg,t1):
    modes = np.array([(Rg**2/p**(2*v+1)/np.pi**2/6.0)*(1-np.exp(-t*p**(3*v)/t1)) for p in
range(1,10)])
    return modes.sum()
```

```python
def MSD(D,t,Rg,v,t1):
    return np.sqrt(D*t+(4*kp(v,t,Rg,t1)))

def gPT_noexp(eta,xi,t,D,w0,a,R0,lambdaex,lambdaem,n,Rg,v,t1):
    return                                                    m.sqrt(m.pi)*k(eta-
MSD(D,t,Rg,v,t1)*xi,a,R0,lambdaem,n)*k(eta+MSD(D,t,Rg,v,t1)*xi,a,R0,lambdaem,n)/(8*MS
D(D,t,Rg,v,t1)**2+w2(eta-
MSD(D,t,Rg,v,t1)*xi,w0,lambdaex,n)+w2(eta+MSD(D,t,Rg,v,t1)*xi,w0,lambdaex,n))

def gPTz1_hermite(xi,t,D,w0,a,R0,lambdaex,lambdaem,n,Rg,v,t1):
    return np.sum(gPT_noexp(xi,xh,t,D,w0,a,R0,lambdaex,lambdaem,n,Rg,v,t1)*yh)

def gPT_hermite(t,D,w0,a,R0,lambdaex,lambdaem,n,Rg,v,t1):
    return quad(gPTz1_hermite,0,200,args=(t,D,w0,a,R0,lambdaex,lambdaem,n,Rg,v,t1))

def gPT_n(t,D,C,w0,a,r0,lambdaex,lambdaem,n,v,t1):
    v1=vol1(a,r0,lambdaem,n)
    v2=vol2(w0,a,r0,lambdaex,lambdaem,n)
    Rg=0.33/D
    print "c = ",C,"vol =",v1*v1/v2,"D= ",D,"Rg = ",Rg, "t1 = ",t1

    return      np.array([1+gPT_hermite(tt,D,w0,a,r0,lambdaex,lambdaem,n,Rg,v,t1)[0]/C/6.022e-
1/v1/v1 for tt in t])

modelFCS_PTn = Model(gPT_n,independent_vars=['t'])

# functions describing crosscorrelation functions that are derived from U1(z1)*exp(-(z2-
z1)^2/s^2)*U2(z2)

def kpc(v,t,Rg,t1):
    modes=np.array([((Rg**2/p**(2*v+1)/np.pi/6.0**2)*(1-(-1)**p*np.exp(-t*p**(3*v)/t1)))  for
p in range(1,15)])
    return modes.sum()

def MSDCC(D,t,Rg,v,t1):
    return np.sqrt(D*t+(4*kpc(v,t,Rg,t1)))

def
gcPTC_noexp(eta,xi,t,D,w11,w22,a1,a2,R1,R2,lambdaex1,lambdaem1,lambdaex2,lambdaem2,n
,dz,Rg,v,t1):
    return                                                    m.sqrt(m.pi)*k(eta-
MSDCC(D,t,Rg,v,t1)*xi+dz,a1,R1,lambdaem1,n)*k(eta+MSDCC(D,t,Rg,v,t1)*xi,a2,R2,lambda
em2,n)/(8*MSDCC(D,t,Rg,v,t1)**2+w2(eta-
MSDCC(D,t,Rg,v,t1)*xi+dz,w11,lambdaex1,n)+w2(eta+MSDCC(D,t,Rg,v,t1)*xi,w22,lambdaex
2,n))
```

```python
def
gcPTCz1_hermite(eta,t,D,w1,w2,a1,a2,R1,R2,lambdaex1,lambdaem1,lambdaex2,lambdaem2,n,
dz,Rg,v,t1):
    return
np.sum(gcPTC_noexp(eta,xh,t,D,w1,w2,a1,a2,R1,R2,lambdaex1,lambdaem1,lambdaex2,lambda
em2,n,dz,Rg,v,t1)*yh)

def
gcPTC_hermite(t,D,w1,w2,a1,a2,R1,R2,lambdaex1,lambdaem1,lambdaex2,lambdaem2,n,dz,Rg,
v,t1):
    return                                              quad(gcPTCz1_hermite,-
200,200,args=(t,D,w1,w2,a1,a2,R1,R2,lambdaex1,lambdaem1,lambdaex2,lambdaem2,n,dz,Rg,v,
t1))
#
def
gcPTC_n(t,D,C,w1,w2,a1,a2,R1,R2,lambdaex1,lambdaem1,lambdaex2,lambdaem2,n,dz,Rg,v,t1
):
    v1=vol1(a1,R1,lambdaem1,n)
    v2=vol1(a2,R2,lambdaem2,n)
    print "c = ",C,"D= ",D,"Rg = ",Rg, "t1 = ",t1

    return
np.array([1+gcPTC_hermite(tt,D,w1,w2,a1,a2,R1,R2,lambdaex1,lambdaem1,lambdaex2,lambda
em2,n,dz,Rg,v,t1)[0]/C/6.022e-1/v1/v2/2.0 for tt in t])

modelFCS_PTCn = Model(gPTC_n,independent_vars=['t'])
```

VII.   MSD Fitting

```python
import numpy as np
from pandas import DataFrame, Series
from lmfit import minimize, Parameter
import pandas as pd
import math as m
import matplotlib.pyplot as plt
from scipy.integrate import quad
from scipy.optimize import fsolve
from scipy.interpolate import interp1d
import sys
import os
import pickle
import collections
from GaussianModels import vol1, vol2, vol2c, g_n, gPT_n, modelFCS_n, modelFCS_PTn

#defines the location of the parameters
paradir='../062415/50um/dilutions/SOME/'
```

```
datadir='../061515/PCR/'
dzdir='../061515/OL_N'

parameters=collections.defaultdict(list)
with open(paradir+'corr_average_B3R6.pkl','r') as paraPickleFile:
    parameters['B'].append(pickle.load(paraPickleFile))
    parameters['B'].append(pickle.load(paraPickleFile))
    parameters['B'].append(pickle.load(paraPickleFile))
    parameters['B'].append(pickle.load(paraPickleFile))
    parameters['R'].append(pickle.load(paraPickleFile))
    parameters['R'].append(pickle.load(paraPickleFile))
    parameters['R'].append(pickle.load(paraPickleFile))
    parameters['R'].append(pickle.load(paraPickleFile))

bBlue=parameters['B'][2]
bRed=parameters['R'][2]

w1=bBlue['w0'].value
w2=bRed['w0'].value
r1=bBlue['r0'].value
r2=bRed['r0'].value
a1=value=bBlue['a'].value
a2=value=bRed['a'].value
lambdaex1=0.488
lambdaem1=0.519
lambdaex2=0.633
lambdaem2=0.657
n=1.33
dz=1.16885461

print "w1 = ",w1
print "w2 = ",w2
print "r1 = ",r1
print "r2 = ",r2
print "a1 = ",a1
print "a2 = ",a2

v1b=vol1(a1,r1,lambdaem1,n)
v2b=vol2(w1,a1,r1,lambdaex1,lambdaem1,n)
print "Volume Blue = ",v1b*v1b/v2b

v1r=vol1(a2,r2,lambdaem2,n)
v2r=vol2(w2,a2,r2,lambdaex2,lambdaem2,n)
print "Volume red = ",v1r*v1r/v2r

filename='PCR_4000b'
```

```python
corrSet=pd.read_csv(datadir+filename+'.csv')

#data set for fitting mean square displacements
corrData=corrSet[corrSet['delta_t']>=1e-7]
corrData=corrData[corrData['delta_t']<=10]

# plot the data and have the user decide about the cutoff time after which only diffusion is
dominating
plt.figure()
plt.errorbar(corrData['delta_t'],corrData['meanR'],yerr=corrData['stdR'])
plt.xscale('log')
plt.show()

# calculate fit to data and fit to noise
logstdB=np.log10(corrData['stdR'])
logt=np.log10(corrData['delta_t'])
pf=np.polyfit(logt,logstdB,4)
p=np.poly1d(pf)
print pf
fitNoiseB=10**p(logt)


#data set for finding normalization constant
corrNorm=corrSet[corrSet['delta_t']>=1e-7]
corrNorm=corrNorm[corrNorm['delta_t']<=1e-6]

# fit a horizontal line to correlation functions for times between 1e-7 and 1e-6
normb=np.polyfit(corrNorm['delta_t'],corrNorm['meanB'],0,w=corrNorm['stdB'],cov=True)[0][0
]
normr=np.polyfit(corrNorm['delta_t'],corrNorm['meanR'],0,w=corrNorm['stdR'],cov=True)[0][0]
print "normalizations R,B: ",normb,normr

stdeBlue=np.array(corrData['stdB']/(normb-1.0)/np.sqrt(20))
stdeRed=np.array(corrData['stdR']/(normr-1.0)/np.sqrt(20))

# create autocorrelation function for the particular optical parameters as function of msd
msd=np.logspace(-4,2,2000)
logmsd=np.linspace(-4,2,2000)
logtime=np.log10(corrData['delta_t'])

ginterB=(g_n(msd,0.5,1.0,w1,a1,r1,lambdaex1,lambdaem1,n)-1.0)*6.022e-1*v1b*v1b/v2b
ginterR=(g_n(msd,0.5,1.0,w2,a2,r2,lambdaex2,lambdaem2,n)-1.0)*6.022e-1*v1r*v1r/v2r
#ginterR=np.array([gr(d2,b) for d2 in msd])

plt.figure()
plt.plot(msd,ginterB,"b")
```

```
plt.plot(msd,ginterR,"r")
plt.xscale('log')
plt.ylabel('theoretical g-1.0')
plt.xlabel('mean square displacement micrometer^2')

# do the logarithmic interpolation
msdBinter=interp1d(ginterB,logmsd,bounds_error=False)
msdRinter=interp1d(ginterR,logmsd,bounds_error=False)

plt.figure()
plt.xscale('log')
plt.yscale('log')
plt.ylabel('mean square displacement in micrometer^2')
plt.xlabel('delta t in sec')

slope_array=[]
bias_range=np.linspace(-.15,.15,31)
for bias in bias_range:
    gblue=np.array((corrData['meanB']-1.0)/(normb-1.0))*(1-bias)
    msdlogB=np.array(msdBinter(gblue))
    msdBlue=10**msdlogB

    # lets select the long times and determine its slope
    time_window=np.array(corrData['delta_t']>1e-3) & np.array(corrData['delta_t']<1e-2)
    msdlogB_longtime=msdlogB[time_window]
    longtime=logtime[time_window]
    slope_array.append(np.polyfit(longtime,msdlogB_longtime,1)[1])

    plt.plot(corrData['delta_t'],msdBlue)

slope_array=np.array(slope_array)
slope_inter=interp1d(slope_array,bias_range)
print slope_inter(1.0)
plt.show()
```

VIII.   Nanofabrication Protocol

Nanofabrication
Nanofabrication for this project is performed at the Center for Functional Nanomaterials at Brookhaven National Laboratories, Upton NY.

Materials:
Pyrex 7740 (borosilicate glass) or similar glass (i.e. Fused Silica)

1) Piranha Cleaning

a. Before attempting to pattern a surface with nano features one must first clean the surface of interest
b. Place the 500um glass wafers in a non-corrosive wafer boat / Teflon carrier and immerse wafers in a vat of piranha cleaning solution
    i. 3 parts H_2SO_4 : 1 part H_2O_2
    ii. Each should be done in a new fresh batch of solution
c. Lightly shake wafer boat to induce convection then allow to rest in water while filling up new container with more water
d. Dry with ultrapure argon or nitrogen
    i. Alternative is spin dry
e. Alternative cleaning can be performed with Acetone / IPA / DI rinses

2) Metal Mask Deposition
a. Typically for Nano-slits 50nm Cr offers best protection for all other forms of subsequent etching, but up to 20nm is sufficient.
b. Thermal / E-beam evaporator

3) HMDS coating
a. Naturally dehumidifies surface creating highly water repellant layer
b. Spin at same speed as resist in next step

4) Resist coating
a. Spin coat
    i. Note: Filter all resists with syringe and 0.2um filter for optimal deposition
    ii. Optical
        1. S1811
            I.   4000rpm for 45sec
    iii. EBL
        1. ZEP520A 100% pure
            I.   4000rpm for 45sec
b. Pre-bake wafers on hotplate
    i. 110 C for optical resists / 2 minutes
    ii. 180 C for EBL resists / 5 minutes

5) Exposure
a. Optical Lithography
    i. Exposure time
        1. 8 seconds for S1800 series – important not to overexpose
    ii. Type
        1. Hard contact / 30um gap – critical for their to be maximum contact to prevent light leakage – can result in larger structures than anticipated
b. EBL
    i. Small features
        1. 2nA_ap5
    ii. Large features (more than 1mm square area)
        1. 20nA_ap7

6) Development
a. Develop using appropriate developer
    i. Optical (S1800 series)

1. MF-312
                        I.   2 parts DI : 1 part MF312
                                i. Must dilute - Otherwise the developer will eat away
                                    at the resist entirely
                        II.   45 sec to 1m15sec
            ii. EBL
                1. Xylene
                        I.   2 minutes
                2. IPA
  7) Metal Etching
        a. Cr Etching Wet Etch
            i. 3 minutes with Transene Cr Etchant
            ii. 3 min DI Rinse
            iii. Note: Cr Wet etch may result in some undercutting or overcutting
                depending on if the etch is isotropic or anisotropic – if channel geometry
                at walls is critical, important to use Dry Etch
        b. Cr Dry Etch
            i. Oxford C
                1. Special Cr Etch recipe available – can modify the time as
                    appropriate to etch corresponding thicknesses (e.g. ~1m30s to etch
                    25nm Cr)
  8) Glass etching
        a. Wet Etch BOE
            i. Place wafers in wafer / Teflon boat and immerse them in BOE (10:1) for
                varying amounts of time
                1. 5min45sec ~ 100nm as tested with AFM
                2. etch rate is linear
            ii. Rinse wafer with DI water at least 3x
        b. Dry Etch (Bosch Process)
            i. SiO2 recipe – 25nm/min

Note: If at this point you would like to design a chip with two sets of channels at different
heights and have incorporated the required alignment marks in your design, you can proceed to
the following alternative steps before going to step 9 below. Alignment marks must be large
enough to be able to locate easily as well as including multiple – at a minimum four should
included – one at each corner of sample area.

Different heights can be performed using a combination of EBL and Optical lithography or only
EBL. It is recommended to etch the previous photoresist prior to applying another resist. It is
also generally easier to etch the smaller nano-channels first, as application of resist over larger
structures can prove problematic.
  • Cleaning
        o Resist removal
            ▪ Acetone
            ▪ 1165 remover

- Repeat procedure starting at step 3 ABOVE

---

9) **Mask Removal**
   a. Resist removal
      i. Acetone
      ii. 1165 Remover
   b. Metal Removal
      i. Cr Etchant (as above)

Note: At this point steps apply to both nano-fabricated AND blank pieces

---

10) **Surface Cleaning**
   a. Piranha bath (3:1 Sulfuric Acid to 30% Hydrogen Peroxide – 1:1 ratio also reported)
   b. Rinse DI Water (at least 3x)
      i. Renberg et. al 2009 highlights importance of multiple rinses to eliminate trapped Piranha solution, which can result in delamination of samples when heated
      ii. Sonication for 20 min works as well – change DI water every 5 min
   c. Mechanical Polishing
      i. Scrub substrate with a wet melamine foam sponge while flushing with DI water
      ii. Dry with inert gas (Nitrogen, Argon, etc)

Optional Step: Most critical for Thermal Bonding

11) **Surface Activation**
   a. Ammonium Hydroxide
      i. Activate the surface so that the glass wafers will adhere to one another. Aqueous solution composed of 29% NH4OH (ammonium hydroxide) Heat this solution on a hot plate until temperature rises to approximately 40 C.
      ii. Heat Wafers for 30 min in solution
      iii. Rinse with DI water (Doyle group rinses 12x with fresh DI baths)
      iv. Spin Dry
   b. O2 Plasma
      i. Trion Etcher
      ii. 5 min O2 plasma

---

12) **Spontaneous Bonding**
   a. Spontaneous Bonding

       i.   Use new gloves which are a size too small (avoiding any wrinkles)

      ii.   Align the thin wafer on top of the thicker patterned wafer to enclose the etched channels.

            1.   Approach the patterned substrate surface slowly and when within a mm press together from the center with thumb and index finger

     iii.   At this point, if there is excess air trapped in between the two wafers, follow the following procedure:

            1.   To remove these pockets of air, place on a clean, flat surface. Press against the top of the wafer with cloth, rubbing air bubbles to the sides of the wafer.

            2.   If you see interference rings that means your spontaneous bonding was not good. Occasionally there will be a few fringes or rings surrounding dusts or particles; if the majority of the surface area is clear, this suggests a good bond

            3.   Test of successful bonding is by placing sample on hotplate set at 200C for 2 min; if they remain attached, spontaneous bonding was successful

            4.   If unsuccessful, go back to mechanical polishing step for both substrates

---

Permanent Substrate Bonding Options

13) Thermal Bonding

    a. Sources

        i.   Mao 2005 / Doyle Lab [125]

    b. Temperature Profile

        i.   T1 550C / tm1 8 hours

       ii.   T2 550C / tm2 12-16 hours

      iii.   T3 25C / tm3 5 hours
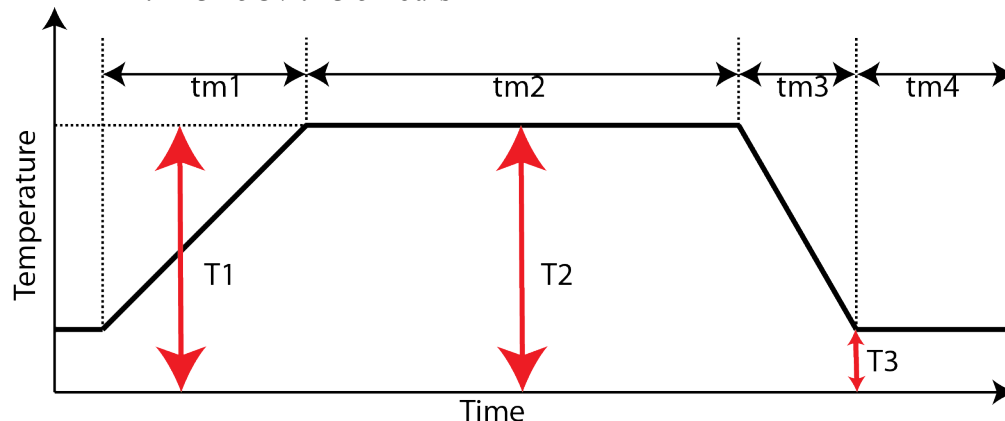
14) PSQ Bonding

    a. Sources

        i.   Gu et al. [131]

       ii.   Sriram et al. [130]

      iii.   Leichle et al. [135]

    b. NOTE: Processing is to be done on non-fabricated, clean glass

  i. Permanent Bonding forming within 10 min of initial contact

  ii. High Power / Low Pressure increasing bonding time significantly by roughening the PSQ surface

  iii. Focus should be on Medium Power / High Pressure if possible

  iv. Maximum aspect ratio obtained is less than 4×10^{-5} (500um width / 18nm depth)

  v. Samples can be cleaned / separated by using commercially available removers.

   1. Soak in Dynasolve 210 (Dynaloy, Inc.) with ultra-sonication for 2–3 h or overnight without sonication

   2. Rinsing with IPA

c. Bake at 180C for 2 min to make sure glass is completely dry

d. Mix 2:1 Xylene:Hardsil AP (Gelest) - FRESH

  i. Filter with 0.45um PTFE membrane or better

  ii. Gu et. al Utilized various dilutions and undiluted

  iii. Leichle et. al utilized 1:1.5 PSQ:Xylene

e. Spin coat solution

  i. 3000rpm for 30s

f. Bake at 240C for 30min

g. O2 Plasma

  i. Trion Etcher

  ii. Settings From Sriram et al. / Leichle / Gu

   1. 25 sccm O2 / 17 sccm O2

   2. 50W RF (Range of 20-150W tested) / 50W

   3. 1.5 min / 1 min / 30sec

   4. 150mTorr (High Pressure) - 15mTorr (Low) / 150mTorr

h. After contact can be assisted by heating at 60C for 1 hour

15) Indium Bonding

a. Sputter evaporation of 100 – 200 Angstroms of Indium (10-20nm)

b. Combine two samples with uniform loading

  i. Standard Pressure or under vacuum / compression

  ii. Room temperature or 150 C

c. Cr normally used as adhesion layer prior to indium-indium bonding, but that would not work in terms of fluorescence measurement